

Universidade de São Paulo
Instituto de Física

Testando Modelos de Matéria Escura Auto-Interagente em Telescópios de Neutrinos

Denis Stefan Robertson Sotelo

Orientador: Profa. Dra. Ivone Freire da Mota e Albuquerque

Tese de doutorado apresentada ao Instituto de Física da
Universidade de São Paulo, como requisito parcial para
a obtenção do título de Doutor em Ciências.

Banca Examinadora:

Profa. Dra. Ivone Freire da Mota e Albuquerque (IF-USP)

Prof. Dr. Laerte Sodre Junior (IAG-USP)

Prof. Dr. Rogério Rosenfeld (IFT-UNESP)

Prof. Dr. Enrico Bertuzzo (IF-USP)

Prof. Dr. Rodrigo Nemmen da Silva (IAG-USP)

São Paulo
2017

FICHA CATALOGRÁFICA
Preparada pelo Serviço de Biblioteca e Informação
do Instituto de Física da Universidade de São Paulo

Sotelo, Denis Stefan Robertson

Testando Modelos de Matéria Escura Auto-interagente em Telescópios de Neutrinos. São Paulo, 2017.

Tese (Doutorado) – Universidade de São Paulo. Instituto de Física. Depto. de Física Experimental.

Orientador: Prof^a Dr^a Ivone Freire da Mota e Albuquerque

Área de Concentração: Astrofísica de Partículas

Unitermos: 1. Matéria Escura; 2. Física de partículas; 3. Neutrinos.

USP/IF/SBI-117/2017

University of São Paulo
Physics Institute

Probing Self-Interacting Dark Matter Models with Neutrino Telescopes

Denis Stefan Robertson Sotelo

Supervisor: Prof. Dr. Ivone Freire M. Albuquerque

Thesis submitted to the Physics Institute of the University of Sao Paulo in partial fulfillment of the requirements for the degree of Doctor of Science.

Examining Committee:

Prof. Dr. Ivone Freire da Mota e Albuquerque (IF-USP)

Prof. Dr. Laerte Sodre Junior (IAG-USP)

Prof. Dr. Rogério Rosenfeld (IFT-UNESP)

Prof. Dr. Enrico Bertuzzo (IF-USP)

Prof. Dr. Rodrigo Nemmen da Silva (IAG-USP)

São Paulo
2017

A mi papá, que Dios lo tenga en Su gloria.

Agradecimentos

Este trabalho não teria sido possível sem a valiosa ajuda de tantas pessoas que me apoiaram ao longo destes anos de pesquisa. Gostaria poder agradecer a todas elas como deveria. Só posso dizer que as guardarei sempre na alma e peço a Deus as guarde sempre.

Em primeiro lugar, quero agradecer muito a Deus Nosso Senhor, sem Ele literalmente nada seria possível. Também estou muito agradecido à Santíssima Virgem Maria, Sua Mãe Imaculada, pelos tantos cuidados e favores, de maneira especial pela fortaleza para levar a bom término esta tese.

Também quero agradecer muito à Ivone pela sua guia, a confiança e todo o apoio e conselho ao longo destes anos. Nela achei não apenas a melhor orientadora que podia ter encontrado, mas também uma grande amiga. Sempre lhe estarei agradecido. Agradeço também aos meus pais e à minha irmã pelo grande apoio apesar da distância e também à toda minha família. À todos os meus amigos, de maneira muito especial à Diana, por toda sua ajuda, tempo, apoio e também paciência. Simplesmente fico sem palavras para lhe agradecer, um abraço de gratidão é para ela. Agradeço também ao Nícolas pelos inúmeros cafés, discussões e também ajudas com o português. Quero agradecer também aos padres Juan Manuel e Adílson, aos professores e colegas do IF, em especial aos do grupo de pesquisa e aos membros da banca examinadora.

Agradeço também a todo o pessoal do IF, da secretaria, da CPG e ao Sergio que várias vezes me ajudaram seja com documentos e resolvendo consultas ou problemas com o computador.

Quero agradecer também às boas pessoas que me hospedaram nesta cidade, em especial à dona Lu e ao senhor Djalma por me fazer sentir parte da sua família.

Finalmente, agradeço também à Fundação de Amparo à Pesquisa do Estado de São Paulo (FAPESP) pelo apoio financeiro e pela oportunidade de desenvolver este trabalho.

Abstract

In this thesis we studied dark matter models with strong self-interactions, typically known as self-interacting dark matter (SIDM). This kind of models constitute a promising solution to the tension between small scale structure observations and predictions assuming the standard case of collisionless cold dark matter (CDM) while keeping the success of the standard cosmological model, Λ CDM, at large scales. The presence of strong self-interactions can increase the dark matter capture and annihilation in astrophysical objects like our sun, enhancing the potential of indirect detection signals. We used the high energy neutrinos produced by such annihilations to probe SIDM models.

We established strong constraints on SIDM with velocity independent cross section by comparing the expected neutrino signal with the results of the IceCube-79 dark matter search. Also, we determined the sensitivity for the IceCube-DeepCore and PINGU detectors for SIDM with a velocity dependent self-interacting cross section (vdSIDM). Most of its relevant parameter space can be tested with the three years of data already collected by IceCube-DeepCore, complementing results from direct detection experiments and other indirect detection studies.

Keywords: dark matter, indirect detection, neutrino telescopes, particle physics

Resumo

Nesta tese investigamos modelos de matéria escura com auto-interações fortes, conhecidos tipicamente como matéria escura auto-interagente (SIDM). Este tipo de modelos constituem uma solução promissora à tensão entre as observações de estrutura a pequena escala e as previsões assumindo o caso padrão de matéria escura fria não colisional (CDM), enquanto se mantêm o sucesso do modelo cosmológico padrão, Λ CDM, a grandes escalas. A presença de auto-interações fortes podem aumentar a captura e a aniquilação da matéria escura em objetos astrofísicos como o nosso sol, aumentando o potencial de sinais de detecção indireta. Usamos o sinal de neutrinos de alta energia produzidos por essas aniquilações para explorar modelos de SIDM.

Estabelecemos fortes vínculos em modelos de SIDM com seção de auto-interação independente da velocidade comparando o sinal de neutrinos esperado com os resultados de busca de matéria escura do IceCube-79. Também, determinamos a sensibilidade dos detectores IceCube-DeepCore e PINGU para modelos de SIDM com uma seção de auto-interação dependente da velocidade (vdSIDM). A maior parte do espaço de parâmetros de interesse pode ser testado com os três anos de dados já coletados pelo IceCube-DeepCore, complementando os resultados de experimentos de detecção direta e outras análises de detecção indireta.

Palavras chave: matéria escura, detecção indireta, telescópios de neutrinos, física de partículas

Contents

Contents	1
1 Small Scale Problems and SIDM	6
1.1 CDM Small Scale Controversies	7
1.1.1 Core-Cusp Problem	7
1.1.2 The Missing Satellites Problem	9
1.1.3 Too Big to Fail Problem	11
1.2 Possible explanations for CDM Small Scale Controversies	12
1.2.1 Baryonic Effects	12
1.2.2 Warm Dark Matter	14
1.3 Self-Interacting Dark Matter	15
1.4 Constraints on SIDM	17
2 SIDM Capture and Annihilation in the Sun	21
2.1 Dark matter capture rate due to interactions with the Sun’s nuclei	21
2.2 Dark matter capture rate due to self-interactions	26
2.3 Dark matter annihilation rate	29
3 Neutrino Flux from Dark Matter Annihilation	34
3.1 Neutrino Propagation from the Sun to the Earth with WimpSim	34
3.1.1 Dark Matter Annihilation in the Sun	35
3.1.2 Neutrino Interactions and Oscillations	36
3.1.3 Neutrino Propagation	37
4 Probing SIDM with IceCube Results	41
4.1 Muon Neutrino Events at IceCube for SIDM Models	41
4.2 IceCube-79 Dark Matter Search Results	44
4.3 Probing velocity-independent SIDM	46
5 Velocity Dependent SIDM	53
5.1 A velocity dependent SIDM Model	54
5.2 Couplings with the Standard Model	62
6 Capture and Annihilation of vdSIDM	66
7 Neutrino Flux from vdSIDM Annihilation	72
8 IceCube-DeepCore and PINGU Sentitivities to vdSDIM	78
Bibliography	84

Introduction

Cosmological observations have led to the Λ CDM model as the standard model of cosmology. In this picture the universe composition is dominated by dark energy (consistent with a cosmological constant Λ) and collisionless cold dark matter (CDM). Despite its great success at large scales ($\mathcal{O}(\gtrsim \text{Mpc})$), the CDM hypothesis encounters some potential difficulties describing the structure at smaller scales [1, 2]. These come from the disagreement between observations and predictions from structure formation simulations. One of these unsolved difficulties is the core-cusp [3] discrepancy between the profiles of dark matter halos observed in dwarf and low surface brightness galaxies, which present a flat density core [4, 5] and the density profiles found in high resolution N-body CDM simulations, which steeply grow toward the center [6, 7, 8]. More recently the so called too big to fail (TBTf) problem [9, 10] came into evidence, and refers to fact that the most massive subhalos in Λ CDM simulations for Milky Way - like galaxies are too dense to be consistent with our galaxy's bright dwarf satellites, so despite being more massive they have no visible counterparts.

Several attempts have been proposed to solve these problems, involving the interplay between baryons and dark matter during the structure formation [11, 12] or assuming different dark matter properties like warm dark matter (WDM) [13, 14]. We briefly review these scenarios in chapter 1. Among the latter type of efforts, a promising possibility is self-interacting dark matter (SIDM) [15], on which our work is focused.

In SIDM models the dark matter particles interact with each other and their elastic collisions over cosmic time scales allow the mass transfer outwards from the dense central regions of dark matter halos. As a consequence of this process, the halo central region becomes more spherical and its density decreases forming a cored profile. Several SIDM simulations support this hypothesis, leading to a better agreement with observations than CDM simulations while keeping its success at large scales [16, 17, 18].

One important consequence of dark matter self-interactions is their effect on the dark matter capture and annihilation in astrophysical objects like our sun. For example, the dark matter scattering off the dark matter particles that have already been captured by the Sun's gravitational potential will enhance its capture rate, and consequently also its annihilation rate [19]. Therefore, SIDM can significantly increase the associated indirect detection signal. In our work, we took into account these effects and determined the

high energy neutrino flux produced in such annihilations to independently probe SIDM models.

We considered two different scenarios. In the first one, we explored SIDM models with a constant dark matter self-interacting cross section. We determined the corresponding dark matter capture and annihilation rates in the Sun. We computed the flux of produced neutrinos through Monte Carlo simulations and estimated the expected signal at the IceCube detector. We then compared our estimated event rates with those of the IceCube-79 dark matter search [20]. We ended up establishing strong constraints on the self-interacting cross section [21].

Additionally, we studied SIDM models in which the self-scattering cross section depends on the relative velocity of the dark matter particles. These scenarios (vdSIDM) were proposed in order to evade strong constraints from analysis of the dark matter distribution in astrophysical systems whose relative velocities are characteristically large ($\sim 200 - 4000$ km/s) such as galaxies, clusters [22, 23] and from the Bullet cluster [24], while, at the same time, to alleviate the TBTF problem of dwarf satellites [25, 26], whose relative velocities are much lower (~ 10 km/s). This kind of models occur naturally in SIDM models containing a dark force described by a Yukawa potential [27, 28, 29].

In spite of their simplicity, vdSIDM models have a rich phenomenology. For example, besides their non trivial self-scattering cross section [29], their annihilation is enhanced by the Sommerfeld effect [30, 31], and there is an additional neutrino signal enhancement due to the dark force mediators' late decays [32]. We consistently accounted for all the relevant processes and determined the vdSIDM annihilation signal at neutrino telescopes. By comparing our predictions to the atmospheric neutrino background we determined the IceCube-DeepCore's and PINGU's neutrino telescopes' sensitivity to vdSIDM. We therefore provided grounds for an independent and complementary probe. Additionally we compared our results with those from direct detection analysis.

This thesis details our research on SIDM and presents our results, also it gives a short overview on the several studies done on these type of dark matter models. The document has two main parts, corresponding to each of our analysis mentioned above and so include the contents of our published work on SIDM [21] and our work submitted to JCAP on vdSIDM [33]. The document is structured as follows: in chapter 1 we describe the CDM small scale problems and some potential solutions focusing on SIDM scenarios. In chapter 2 we detail the calculation of SIDM dark matter capture and annihilation in the Sun. In chapter 3 we describe the propagation of the neutrinos produced from the Sun to the detector and in chapter 4 we compare our estimation with the limits from IceCube and present our results. Chapter 5 opens the second part of this work introducing vdSIDM, it also describes the specific particle model we investigated. Chapters 6 and 7 describe the changes for vdSIDM capture and annihilation in the Sun, and the propagation of neutrinos. In chapter 8 we present our results for the sensitivity to vdSIDM of IceCube-

DeepCore and PINGU detectors. Finally we present our conclusions.

I should note that my PhD studies also included analysis of bino dark matter signatures in direct detection experiments [34], which for being unrelated to our main work we did not include it in this document.

Chapter 1

Small Scale Cold Dark Matter Controversies and Self-Interacting Dark Matter

Cold dark matter (CDM) is an essential ingredient of the standard model of cosmology Λ CDM. It is referred to as cold because the dark matter particles were non-relativistic when structure formation started at the early Universe. It is commonly assumed that CDM interact weakly with ordinary matter, as it is the case of the widely studied WIMPs (Weakly Interacting Massive Particles). Thus, at the early universe, CDM particles were in equilibrium with the primordial plasma until the universe's expansion froze them out, and exist in abundance today as thermal relics.

In the CDM scenario, structure formation occurs hierarchically from the initial smooth Universe until it forms the complex matter distribution observed today. First, small objects are formed from the initial matter distribution inhomogeneities due to their self-gravitational collapse. Then, these objects merge together to form larger and more massive objects, forming galaxies, galaxy clusters and superclusters. At large scales, Λ CDM predictions for the universe structure are remarkably successful, being consistent with several observations as, for example, CMB anisotropies [35], galaxy clustering [36], the Lyman- α forest [37] and baryon acoustic oscillations [38].

Nevertheless, at small scales there seems to be inconsistencies between CDM predictions and observational data [1, 2]. For example, observations from the inner regions of galaxies and Milky Way's dwarf spheroidals show that they are less dense than results from CDM cosmological simulations. The differences between CDM predictions and observations have led to the proposal of many hypothesis in order to solve these discrepancies or at least alleviate them. For example, since baryonic matter is abundant at small scales, these inconsistencies might indicate the importance of the effects from baryonic physics. Another possibility is that the nature of dark matter is more complex and interesting than

the standard collisionless CDM. Along this line, a very attractive scenario is that dark matter particles could have strong self-interactions [15] that would modify the density profiles of dark matter halos achieving a better agreement with observations.

In this chapter we discuss the CDM small scale potential controversies and some proposed solutions, focusing on dark matter self-interactions.

1.1 CDM Small Scale Controversies

Λ CDM structure formation results from simulations are incompatible, at small scales, with current observations. Simulations show that CDM gravitational collapse leads to cuspy dark matter halos while observations favor halos with constant density cores. Also simulated halos retain a large number of substructures, contrasting with the ~ 10 “classical” Milky Way’s satellites. These conflicts are called as the “cusp-core problem” and the “missing satellites problem”. More recently, it has been discovered that in Milky Way like simulated halos, assuming CDM, there are several satellites whose densities are also inconsistent with observations. This is known as the “Too Big to Fail problem”. These controversies are described in detail below.

1.1.1 Core-Cusp Problem

The core-cusp problem refers to the discrepancy between the observations of dark matter halos’ density profiles and those in cosmological simulations. The observed data is well described by profiles that have a constant density core, such as a non-singular isothermal sphere or a pseudo-isothermal (PI) sphere, given by:

$$\rho_{\text{PI}} = \frac{\rho_0}{1 + (r/R_C)^2}, \quad (1.1)$$

where ρ_0 is the central density and R_C is the halo core radius [3]. On the other hand, simulations of dark matter halos, assuming the standard collisionless CDM, are better described by steep density profiles in the inner regions, called cuspy profiles, $\rho \sim r^\alpha$ with $\alpha \approx -1$. It is important to note that, while the simulations are based on the Λ CDM cosmological model, the dark matter density profiles are not predicted directly from first principles, but are derived from analytical fits made to numerical simulations results.

The presence of a cuspy central region characterized by a power-law slope with $\alpha = -1$ has been obtained since early analysis of numerical simulations [39]. Later investigations added support to these findings. For example, a systematic study of many simulated halos, which considered different values for the cosmological parameters, found that the halos’ inner region are well described by a characteristic $\alpha = -1$ slope, independently of the halo’s mass, size or assumed cosmology [6]. This profile is called the “NFW profile”

and is given by:

$$\rho_{\text{NFW}} = \frac{\rho_i}{(r/R_s)(1+r/R_s)^2}, \quad (1.2)$$

where ρ_i is related to the density of the universe at the time of halo collapse and R_s is the scale radius of the halo. Other simulations indicate even steeper inner slopes with $\alpha = -1.5$ [40]. However, more recent results, with very high resolution, obtain a slope with $\alpha = -1$ that becomes shallower ($\alpha = -0.8$) with decreasing radius, down to the innermost resolved point [7, 8].

From the observational side, early works such as [41], find that atomic hydrogen (H I)¹ rotation curves of dwarf galaxies are better described by PI profiles, indicating that these galaxies favor distributions with an approximately constant density core. Later analysis with improved resolution of Low Surface Brightness (LSB) galaxies², using the H α line³, also favored a core dominated structure rather than a cuspy profile [42]. These results still leave some room for observational or physical systematic effects, such as pointing errors on the true dynamical center of the galaxy or non-circular orbits of the gas, that could artificially distort cuspy distributions to cored ones. Nonetheless, the use of high resolution two-dimensional velocity fields significantly reduces the potential impact of those effects. Recent analysis that make use of this tool also find that the PI distribution describes the data better than the NFW profile [5, 43].

Figure 1.1 shows fits to the rotation curves for two LSB galaxies [5]. The data was obtained with high resolution optical velocity fields. The red solid line corresponds to the best fit for an isothermal halo, the green short-dashed line to an NFW halo unconstrained by cosmology, and the black long-dashed line to a NFW halo consistent with Λ CDM. These results clearly show that the core distribution describes better the observations.

Other recent results come from high resolution surveys as The H I Near Galaxy Survey (THINGS). This survey presented the rotation curves and the dark matter density profiles of seven dwarf galaxies, finding flat inner density slopes with a mean value $\alpha = -0.29 \pm 0.07$ [4]. A similar analysis by LITTLE THINGS for 26 dwarfs found $\alpha = -0.32 \pm 0.24$ [44], also in disagreement with the expected slope from Λ CDM simulations $\alpha \approx -1$.

However, this observed disparity might indicate the deficiency of the dark matter-only simulations of structure formation to account for the properties of real galaxies which contain both dark matter and baryons. From this perspective it was proposed that intense baryonic processes like supernovas can impact the evolution of dark matter halos

¹The atomic hydrogen line or H I line, refers to the spectral line produced by the atomic transition of the electron between the two hyperfine levels of the hydrogen 1s ground state. The emitted radiation has a wavelength of 21.106 cm.

²LSB galaxies are late-type, gas-rich, highly dark matter dominated disk galaxies. These are expected to have had a passive evolution, with little evidence of baryonic processes that might have provoked strong perturbations on their matter distribution evolution.

³The H α line refers to the first in the Balmer series, corresponding to the transition of the hydrogen electron from its third to second lowest energy level. It has a wavelength of 656.28 nm, corresponding to the visible part of the electromagnetic spectrum.

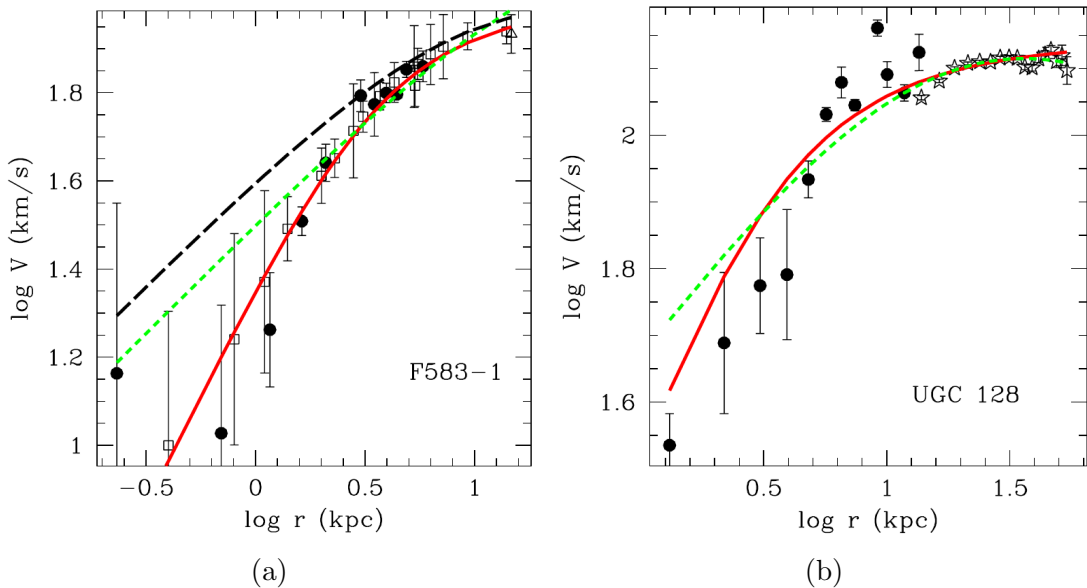


Figure 1.1: Halo fits to rotation curves. The red solid line corresponds to the best fit for an isothermal halo, the green short-dashed line to an unconstrained NFW halo, and the black long-dashed line to a NFW halo consistent with Λ CDM. Figure extracted from [5].

of dwarf galaxies producing low density cored profiles [45, 46, 47]. We describe further these possibilities below in Sec. 1.2.1. On the other hand, the effect of baryon feedback on LSB galaxies, which have larger circular velocities and therefore deeper gravitational potential wells, is expected to be less pronounced [48].

1.1.2 The Missing Satellites Problem

The missing satellites problem refers to the discrepancy between the number of Milky Way’s dwarfs satellite galaxies and the large number of subhalos that are predicted by CDM cosmological simulations [49]. This is illustrated in figure 1.2. When this problem was noticed in the 1990’s, only eleven Milky Way’s satellite galaxies were known within the galaxy ~ 250 kpc virial radius. This number is predicted to be much larger by numerical simulations assuming the standard cosmology (being a factor of $\sim 5 - 40$ more abundant) [50, 51].

The most conservative explanations come from baryonic physics. The idea within this context is that gas accretion in low mass subhalos would be suppressed after the reionization epoch due to the presence of a strong photoionizing UV radiation [52]. So, the observed satellites would correspond to the fraction of subhalos that gathered enough gas before reionization. The smaller subhalos would remain dark and therefore would be much harder to detect. This proposal was tested by simulations and it was found viable [53]. Other proposed solutions involve either modifying the assumed inflation model, or

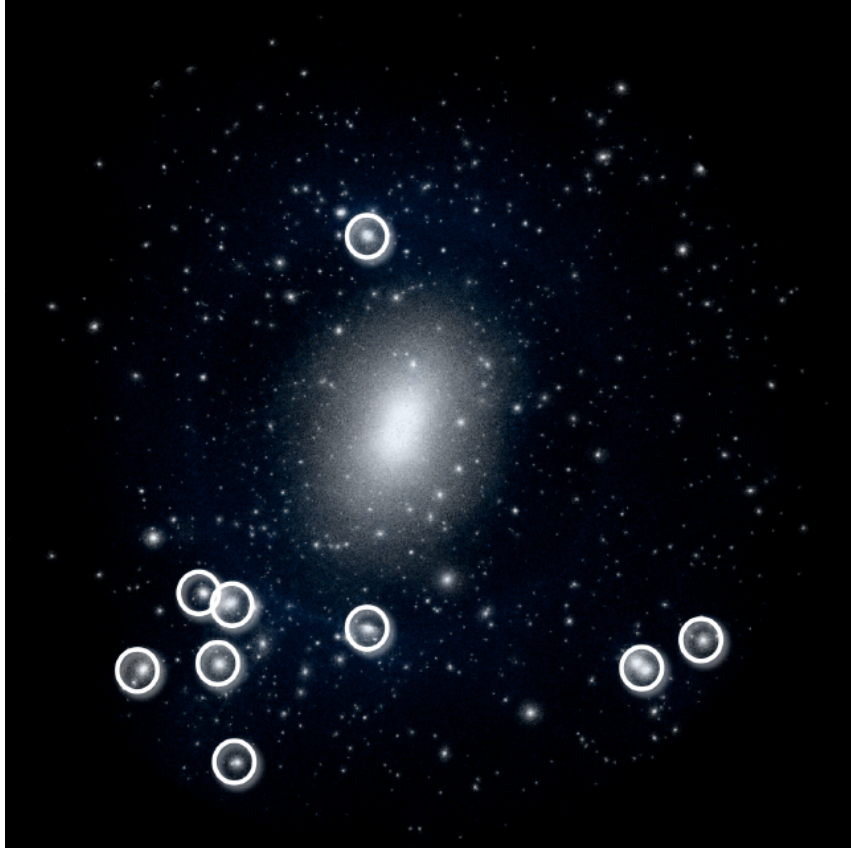


Figure 1.2: Dark matter distribution of a simulated $10^{12}M_{\odot}$ CDM halo. The number of subhalos present in the simulation exceed the number of the known satellites of the Milky Way. The white circles mark the nine most massive subhalos which are expected to host the well known Milky Way's dwarfs satellites. Figure extracted from [1].

considering warm dark matter (WDM) instead of the standard CDM, or yet allowing dark matter strong self-interactions.

Quite recently the Sloan Digital Sky Survey (SDSS) has discovered ~ 20 new ultra-faint satellites with very low luminosities [54, 55, 56]. Taking into account the limited SDSS sky coverage and the dwarf's luminosity attenuation as a function of their distance to the Sun, it was estimated that a large number (between ~ 300 and ~ 600) of satellites should exist within 400 kpc of the Sun that are brighter than the faintest known dwarf galaxies [57]. Even more recently, the Dark Energy Survey have discovered 17 new candidate ultra-faint galaxies in its first two years of observation [58, 59]. A combined analysis using the SDSS and DES findings estimates at least 142^{+53}_{-34} satellites within 300 kpc of the Sun [60]. These results alleviate the CDM's missing satellites problem and it is expected that future surveys like the Large Synoptic Survey Telescope [61] will continue to find many ultra-faint satellites.

1.1.3 Too Big to Fail Problem

The too big to fail problem is also related to the Milky Way dwarf satellites. Specifically, it refers to the fact that Λ CDM simulations predict many large subhalos that are too dense to host any of the brightest satellites of the Milky Way [9, 10]. The mass of the simulated halos exceed by a factor of ~ 5 the ones of the dwarf spheroidals of our galaxy inferred from stellar dynamics.

This problem is illustrated in figure 1.3 [10]. The rotation curves for the largest simulated subhalos are shown for two Aquarius simulations [62]⁴ with halo masses $2.19 \times 10^{12} M_{\odot}$ and $1.39 \times 10^{12} M_{\odot}$. The solid curves correspond to subhalos that are at least 2σ denser than the brightest Milky Way dwarf spheroidals. The data points correspond to the measured V_{circ} for these observed satellites at their half-light radius. It is clear that each simulated halo have several (~ 10) subhalos that are more massive than those observed in our galaxy. These are so massive that should have formed stars but, for some unknown reason, do not have any visible counterpart observed in the Milky Way. While it is possible in principle that these large subhalos exist and somehow have remained dark despite their large mass, it seems physically unlikely. On the other hand, their observation would be a strong confirmation of the Λ CDM at small scales.

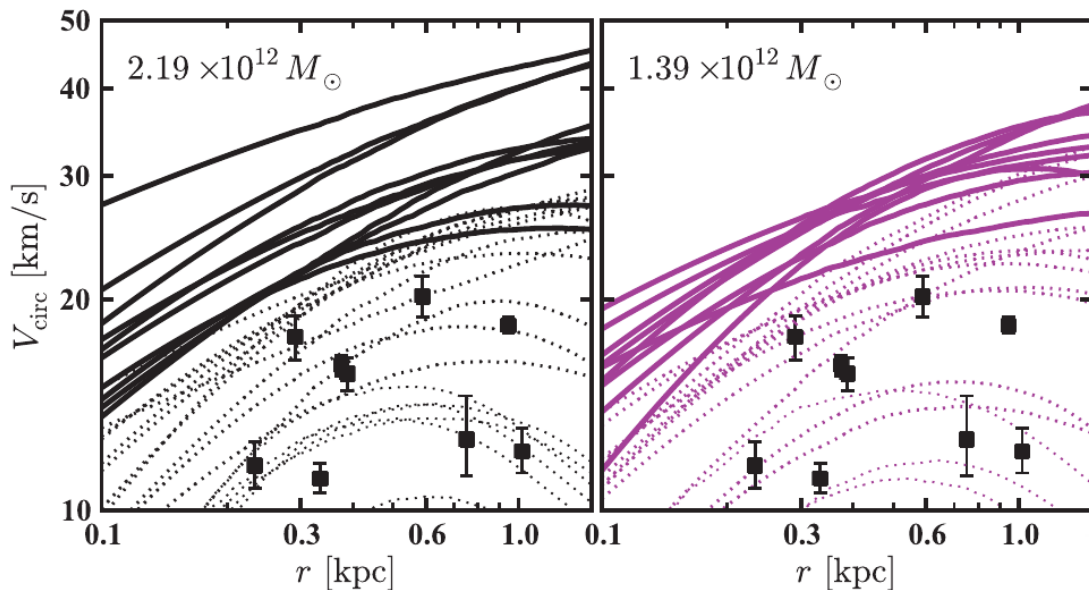


Figure 1.3: Rotation curves for the largest subhalos for two Aquarius simulations. The solid curves represent the rotation curves of those subhalos that are at least 2σ denser than every bright Milky Way dwarf spheroidal. The data points with error bars show measured V_{circ} values for the observed bright satellites. Figure extracted from [10].

One quite simple solution comes from the observation that the number of massive

⁴The Aquarius simulations contain 6 examples of an isolated Milky Way - like halo simulated at ultra-high resolutions in a Λ CDM cosmology. These simulations are used to study the fine-scale structure of our galaxy [62].

subhalos depends on the mass of the host galaxy, so the too big to fail problem would be alleviated if the Milky Way is less massive than is commonly thought $\lesssim 10^{12} M_{\odot}$ [63]. However, several measurements indicate that this is quite unlikely (see for example the summary for the Milky Way mass measurements in [10]).

Another possibility is that the Milky Way halo is not representative of a typical Λ CDM galactic halo. From this perspective, the too big to fail problem would be just a statistical fluctuation. This hypothesis is supported by a statistical analysis of simulated halos [64]. It shows that the variation of subhalos properties is quite large indeed, where at least $\sim 10\%$ of all halos have subhalo populations consistent with the observed kinematics of the Milky Way dwarfs. On the other hand, very recent analysis investigated the too big to fail problem for Andromeda and the Local Group dwarf galaxies and found the same inconsistencies as for the Milky Way [65, 66], disfavoring this explanation.

1.2 Possible explanations for CDM Small Scale Controversies

All the above apparent inconsistencies between CDM predictions and observations are very interesting and call for an explanation. This could come from a better understanding of the galaxy formation evolution, the interplay between baryons and dark matter, the nature of dark matter or a combination of all this. Here we discuss some of the proposed explanations.

1.2.1 Baryonic Effects

Most cosmological simulations neglect the presence of baryons, since they only constitute a small fraction of the total halo mass and also due to their high complexity. However, since they concentrate in the inner regions of halos, their effects are expected to be important at small radii. Recently, there have been several analysis that implemented baryonic processes into halo evolution simulations and they do seem to alleviate CDM's small scale problems.

For example, an analysis concerning the core-cusp problem [11], has shown that cuspy distributions can in fact become shallower when baryonic processes are taken into account. Their result is represented in figure 1.4, which shows the evolution of the density profile of a dwarf galaxy. This analysis used high resolution hydrodynamic cosmological simulations that included explicitly H_2 and metal cooling, star formation and supernova driven gas outflows. It also shows (black dotted curve), the cuspy profile obtained for a dark matter only simulations, without the inclusion of baryonic effects, and with the same initial conditions. A similar analysis also found that the inclusion of baryonic feedback processes in the dark matter halo evolution lead to the formation of cored profiles [67], both of these

results are in good agreement with the observed dwarf rotation curves by THINGS [4]. The same flattening of dark matter cusps is also found in simulations using an adaptive mesh technique and including the stellar feedback effect on the gas dynamics [68].

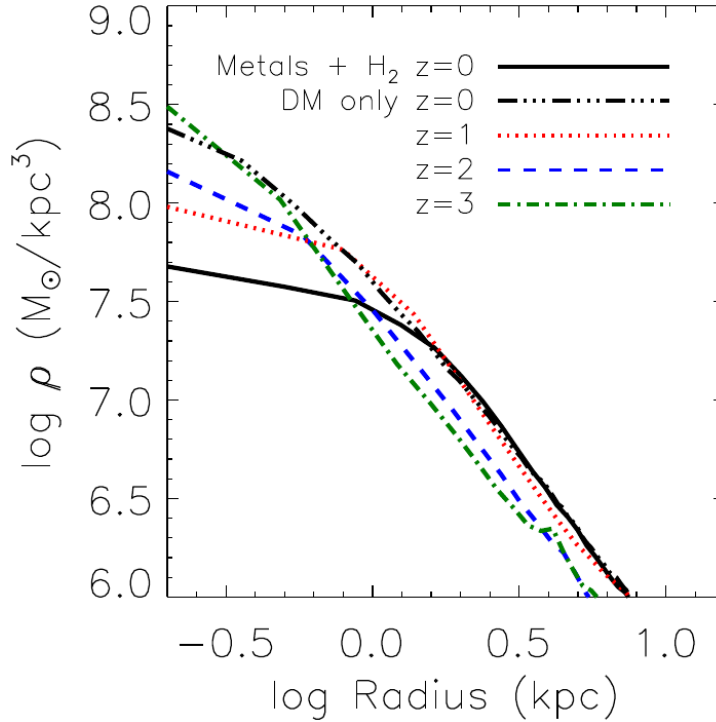


Figure 1.4: Density profile of a dwarf galaxy at several redshifts. The upper dot dashed curve is the cuspy dark matter density profile resulting from a collisionless N-body simulation. The other curves show the evolution of the profile in a cosmological simulation with the same initial conditions including the effects of gas dynamics, star formation and supernova feedback. At $z=0$ (black solid curve) the profile acquires a core with nearly constant density. Figure extracted from [11].

Other analysis using high resolution simulations including a baryonic matter disk further support these findings [12, 69]. They simulated Milky Way mass galaxies including the effects of supernova feedback and tidal stripping⁵. They found that the satellites end up with reduced dark matter densities and also shallower inner density profiles in good agreement with observations. These same simulations also show that including the effect of baryons reduces the overall number of massive subhalos, potentially solving the missing satellites problem.

Additional studies investigated the effect of baryonic feedback on the density profiles of dark matter halos as a function of the halo mass [70, 71]. The authors analyzed 31 galaxies from the MaGICC project, a cosmological hydrodynamical simulation [72], with masses ranging from $\sim 10^{10} - 10^{12} M_{\odot}$. They found that baryonic feedback flattens maximally the halo density profiles in halos with stellar-to-halo mass ratio $M_{*}/M_{\text{halo}} \sim 0.5\%$ or halo

⁵Refers to a subhalo loss of mass due to encounters with the galactic baryonic disk.

masses $\sim 6.3 \times 10^{10} M_{\odot}$. For larger halos, despite the more abundant star formation, the feedback is less effective due to the deeper gravitational potential well, while for smaller ones there is too little star formation to affect the dark matter density profile. In both latter cases the halos are cuspy.

A more recent and similar study [73] analyzed a broader halo mass range $M_{\text{halo}} \sim 10^9 - 10^{12} M_{\odot}$ of simulated halos from the Feedback In Realistic Environments (FIRE) project [74]. They found that dark matter profiles are shallow for $M_{\text{halo}} \sim 10^{10} - 10^{11} M_{\odot}$ due to the strong baryonic feedback and are cuspy for higher or lower halo masses. Their result is consistent with [11, 70, 71].

Regarding the too big to fail problem of Milky Way dwarf satellites, high resolution numerical simulations that included the dynamical effects of supernova feedback [75] found that too much energy (the equivalent of more than 40000 supernovae) must be delivered directly to the dark matter with full efficiency in order to solve the problem. On the other hand, an analysis using FIRE simulations showed that simulated dwarf galaxies agrees with those of the Milky Way and Andromeda [76] and do not suffer the too big to fail problem.

1.2.2 Warm Dark Matter

A different take on CDM small scale controversies is to assume different dark matter properties. One of the proposed solutions is that dark matter is not cold but warm, where their velocity dispersion is intermediate to those of hot (relativistic) and cold dark matter (non-relativistic). The idea is that particles with higher thermal energies would have large enough velocities at the early Universe to smear out fluctuations at sub-galactic scales, preventing gravitational collapse at these scales while not changing structure at larger ones.

Numerical simulations of WDM effects on structure evolution find a better agreement with observations for dark matter masses $m_{\text{WDM}} \sim 1 \text{ keV}$ [13, 77] than CDM. The dark matter halo profiles are still cuspy but with lower densities than those of CDM simulations, so they are more consistent with galaxy rotation curves and dwarfs satellites dynamics. They also show a fewer amount of substructures, alleviating the missing satellites problem. More recent simulations with higher resolution point to the same results. While WDM does not seem to solve the core-cusp problem it has halos with lower densities and fewer substructures in better agreement with observations for $m_{\text{WDM}} \sim 2 \text{ keV}$ [78, 14]. An example is shown in figure 1.5, where the rotation curves of the massive simulated subhalos are compared to the measured values for the Milky Way bright dwarf satellites.

On the other hand, several observations have been used to test the WDM hypothesis, and thus, have imposed constraints in the WDM mass. The most stringent ones come from the Lyman- α forest [79] and from the number of ultra-faint dwarfs galaxies in the

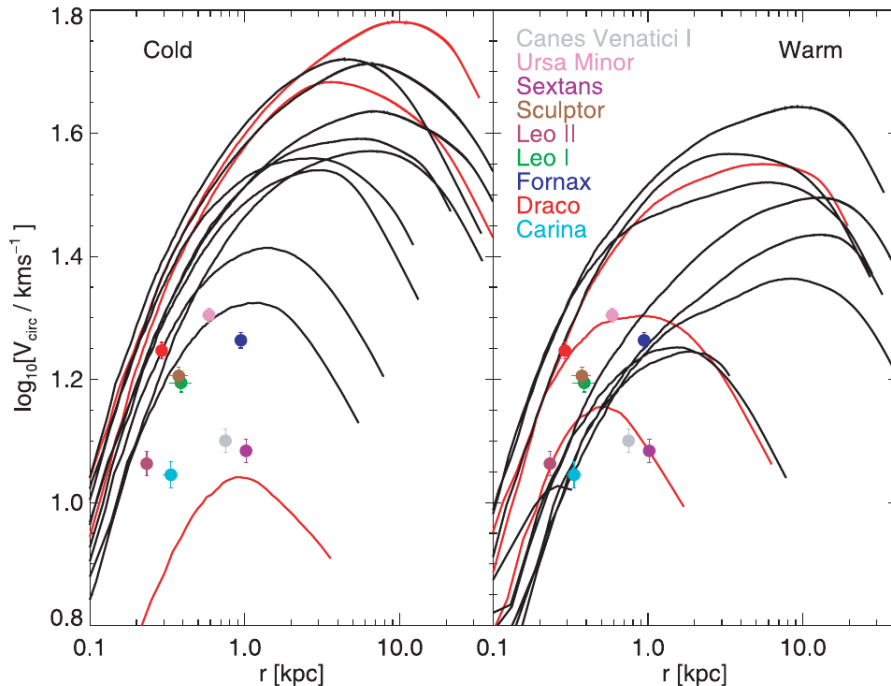


Figure 1.5: Rotation curves for the 12 most massive subhalos in CDM (left) and WDM (right) simulations. The data points correspond to the values measured for the 9 dwarf spheroidals of the Milky Way. Figure extracted from [14].

SDSS data [80]. The former requires that the WDM mass $m_{\text{WDM}} > 3.3$ keV at 2σ level. This result is based on the comparison of high redshift quasar spectra combined with an extended series of hydrodynamical simulations. While the other analysis bounds the WDM particle mass to $m_{\text{WDM}} > 2.3$ keV for thermal WDM also at 2σ level with a maximum likelihood for $m_{\text{WDM}} = 4$ keV. Therefore, a realistic WDM scenario must have a mass of about $m_{\text{WDM}} \sim 4$ keV to be in agreement with both Lyman- α forest and SDSS data. However, it was found that a WDM with this mass value cannot resolve the CDM small scale inconsistencies [81]. A very recent analysis of the Lyman- α forest established a very strong lower limit on the WDM mass, requiring $m_{\text{WDM}} > 5.3$ keV at 2σ C.L. [82], further weakening WDM as an alternative to CDM small scale problems.

1.3 Self-Interacting Dark Matter

Another promising possibility to solve the small scale problems is self-interacting dark matter (SIDM). In these scenarios dark matter particles can scatter elastically with each other. Their self-scattering rate increases at the inner dense regions of halos, so they would naturally affect the structure evolution at small scales. It is important to note that in SIDM models, dark matter strong self-scattering is added to the standard CDM assumption, such that dark matter particles still have weak interactions with baryons as

usual WIMPs.

SIDM were originally proposed to solve the core-cusp and missing satellites problems [15]. The main idea is that the dark matter particles will behave collisionally at the high density regions of halos, modifying the dark matter distribution over the time scale of structure formation. The relevant strength of the self-interactions can be estimated by requiring that the probability of interaction over a time t_{age} comparable to the age of the halo (~ 10 Gyr) be relatively high: $\Gamma_{\text{scatt}} \times t_{\text{age}} \sim 1$. The dark matter self-scattering rate Γ_{scatt} can be written as

$$\Gamma_{\text{scatt}} = \sigma v (\rho_{\chi}/m_{\chi}) \approx 0.1 \text{ Gyr}^{-1} \times \left(\frac{\rho_{\chi}}{0.1 M_{\odot}/\text{pc}^3} \right) \left(\frac{v}{50 \text{ km/s}} \right) \left(\frac{\sigma/m_{\chi}}{1 \text{ cm}^2/\text{g}} \right), \quad (1.3)$$

where m_{χ} is the dark matter particle mass, σ the dark matter self-interacting cross section and v the relative velocity. The central region of a typical dwarf galaxy is characterized by $\rho_{\chi} \sim 0.1 M_{\odot}/\text{pc}^3$ and $v \sim 50$ km/s [4]. Therefore, for a dark matter cross section per unit mass $\sigma/m_{\chi} \sim 1 \text{ cm}^2/\text{g}$ ⁶ or higher one can expect a sufficient number of dark matter particle collisions to effectively modify the halo density distribution. So, within this scenario the kinetic energy can be transferred through the dark matter particle collisions from the hot outer regions of the halo to its colder inner part. This effectively redistributes the particles to higher orbits creating a density profile with a central low density core, alleviating the core-cusp and too big to fail problem. Also, due to the collisional character of SIDM, a more isotropic velocity distribution is expected, making halos more spherical than CDM in their central regions. Additionally, self-interactions could in principle reduce the amount of substructure in the inner parts of dark matter halos through slowly scattering off the dark matter in low density dwarfs [15], mitigating the missing satellites problem. At the same time SIDM keeps large scale structure unchanged, being as consistent with observations as collisionless CDM. These features can be seen in figure 1.6, where large and small scale structure in CDM and SIDM models, obtained by cosmological numerical simulations [22], are shown.

Early analysis using numerical simulations verified the expected phenomenology. Self-interactions in fact allow the energy transfer from the particles in the halo hot external regions to the particles in the cold inner regions. This leads to the formation of isothermal, constant density cores, in better agreement with observations than standard collisionless CDM [16, 17] (see figure 1.7). Other cosmological simulations show that the most consistent results with observations are obtained for a constrained interval of the self-interaction cross section $\sigma_{\chi\chi}/m_{\chi} \approx 10^{-23} - 10^{-24} \text{ cm}^2/\text{GeV}$ (or 0.5 - 5 cm^2/g). Lower or higher values led to almost identical results to CDM or a too effective destruction of many substructures [18, 83].

⁶ $1 \text{ cm}^2/\text{g} \approx 1.8 \times 10^{-24} \text{ cm}^2/\text{GeV}$

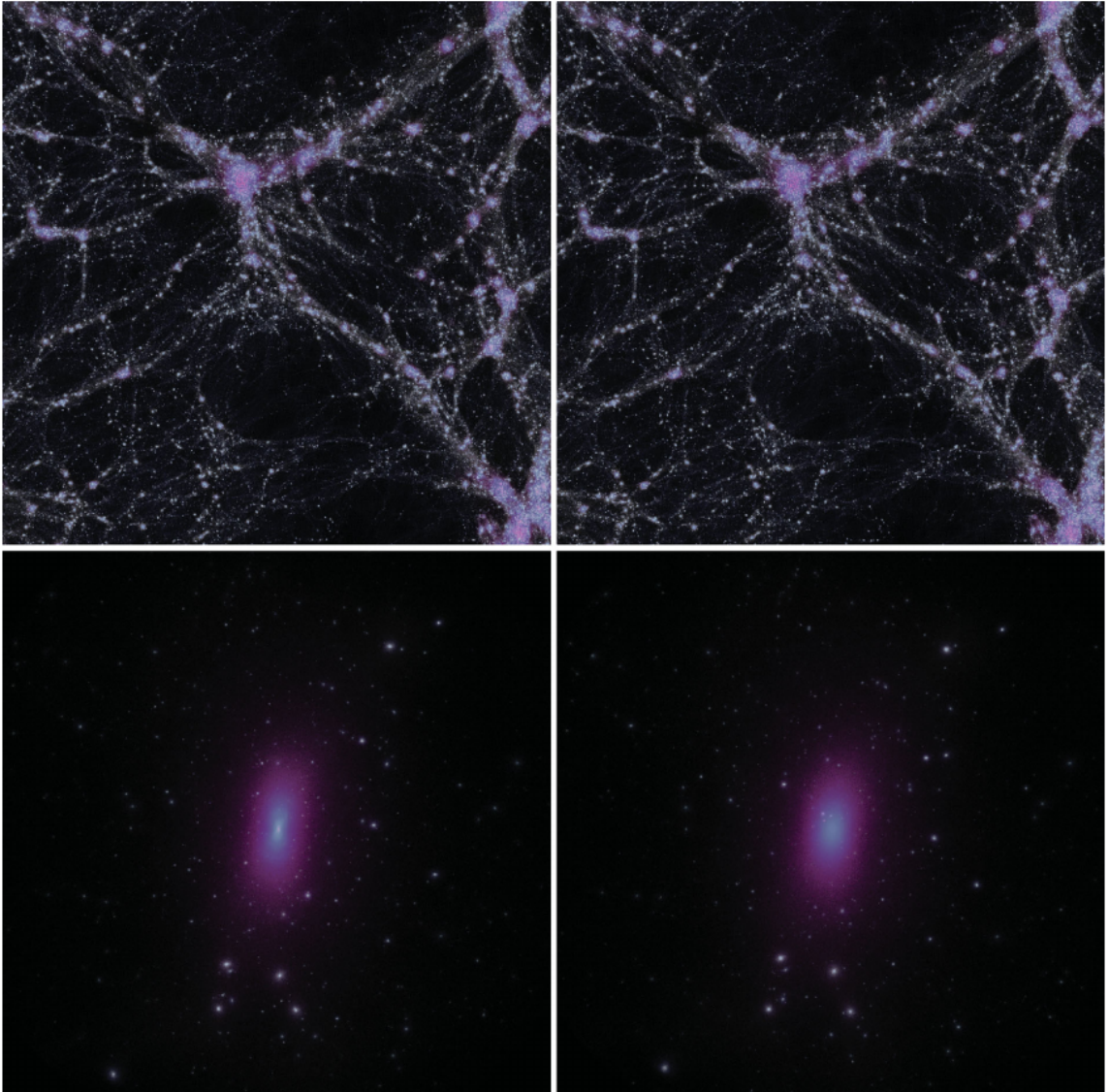


Figure 1.6: Structure formation simulations which compare collisionless CDM with SIDM. At the top, large scale structure is shown for CDM (left) and SIDM with $\sigma_{\chi\chi}/m_\chi = 1 \text{ cm}^2/\text{g}$ (right). The local phase space density is color coded with white being denser than purple. There are no differences between the two cases, showing that SIDM does not affect large scale structure formation. At the bottom, small scale structure in a Milky Way mass halo is shown. The SIDM halo (right) has lower densities (physical density is lower and its velocity dispersion larger) and a more spherical core than the one in CDM. Also, SIDM substructure content is quite similar to CDM's except in the inner region. Figure extracted from [22].

1.4 Constraints on SIDM

Currently, comparisons of SIDM simulations with several observational data have constrained the SIDM parameter space. An analysis investigating the consistency between observed density profiles and substructure abundance of galaxies and clusters, and the results for SIDM structure formation using high resolution cosmological simulations [22],

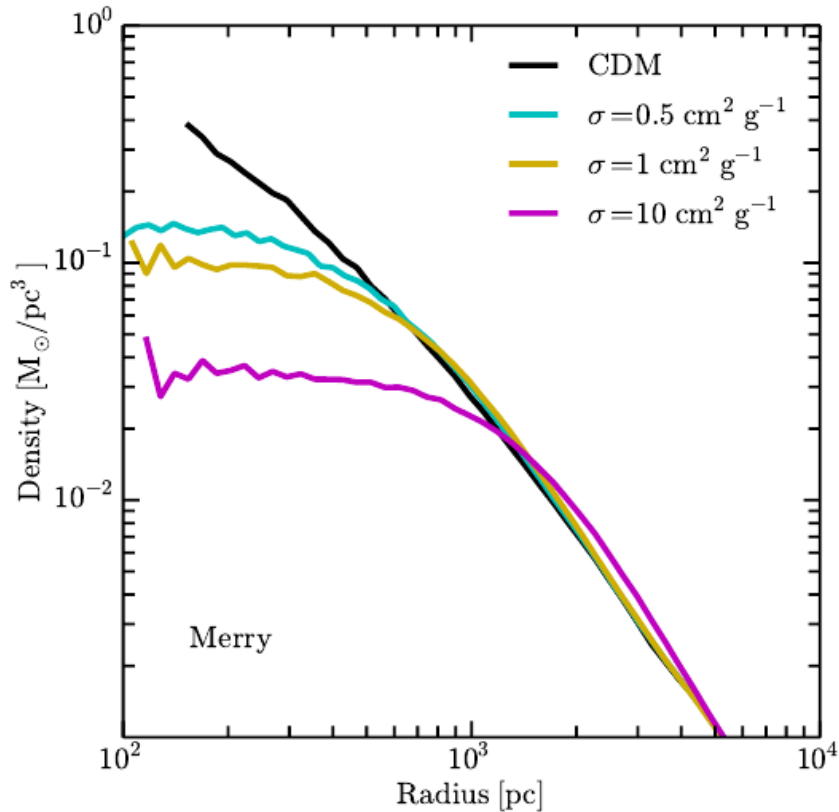


Figure 1.7: Density profiles in collisionless CDM (black) and SIDM (colored) simulations. Results for SIDM show the presence of well resolved and low density cores. Figure extracted from [84].

find that in SIDM models with $\sigma_{\chi\chi}/m_\chi = 1 \text{ cm}^2/\text{g}$, the halo core densities are too low to match the observations of galaxy clusters, LSB spiral and dwarf spheroidal galaxies. On the other hand, SIDM models with $\sigma_{\chi\chi}/m_\chi = 0.1 \text{ cm}^2/\text{g}$ are capable of reproducing the observed core sizes and central densities of those systems. Thus, SIDM with $\sigma_{\chi\chi}/m_\chi \gtrsim 1 \text{ cm}^2/\text{g}$, seem to be too effective at forming dark matter halos with flat low density cores, in disagreement with observations, while SIDM models with $\sigma_{\chi\chi}/m_\chi \approx 0.1 \text{ cm}^2/\text{g}$ are more consistent with observations than collisionless CDM, alleviating the core-cusp problem.

A very similar result was obtained from an analysis of halo shapes using ellipticity measurements from gravitational lensing and x-rays for galaxies and clusters [23]. Numerical simulations considering SIDM with $\sigma_{\chi\chi}/m_\chi = 1 \text{ cm}^2/\text{g}$ present halos that are likely too spherical to be consistent with observations. However, these are in good agreement with halo's ellipticity for SIDM models with $\sigma_{\chi\chi}/m_\chi = 0.1 \text{ cm}^2/\text{g}$.

Another constraint comes from an analysis of several data of the merging galaxy cluster 1E 0657-56, the Bullet Cluster [24]. Measurements with X-rays, strong and weak lensing, and optical observations were compared with numerical simulations that include the effect of dark matter self-interactions. If dark matter were collisionless, the dark matter concentration peaks should coincide with the galaxies distribution center, since

these are also non collisional (see figure 1.8). But, if dark matter have self-interactions, the dark matter subclusters would have experienced a drag force to the system's center when they were traversing each other, just as the gas in the merger but with a much lower strength. This force would cause a shift between dark matter and galaxies position. From the non-observation of such displacement an upper bound on SIDM was obtained: $\sigma_{\chi\chi}/m_{\chi} \leq 1.25 \text{ cm}^2/\text{g}$ at 68% confidence level.

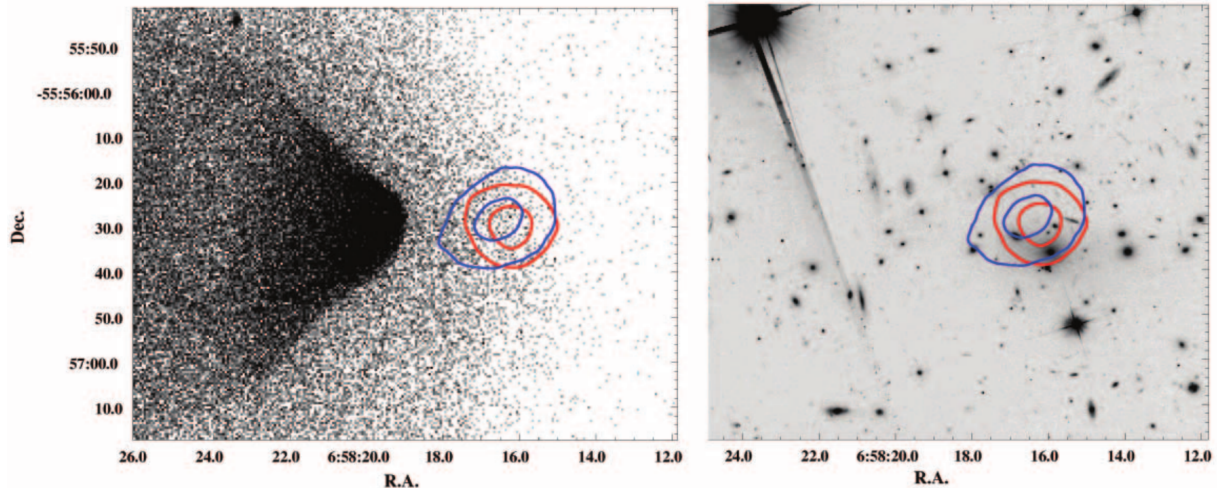


Figure 1.8: Close-up of the subcluster bullet region. The dark matter and galaxy centroid contours at 1σ and 3σ are shown in blue and red, respectively. The figure at the left corresponds to the X-ray Chandra image, while the right is the optical Hubble Space telescope image. Figure extracted from [24].

Other constraint came from an analysis of the too big to fail problem for SIDM models [26]. In this analysis, high resolution simulations of a Milky Way size halo were investigated for several SIDM scenarios. From the comparison between simulated subhalos and the kinematics of the Milky Way's satellites, a constant self-interaction cross section $\sigma_{\chi\chi}/m_{\chi} = 0.1 \text{ cm}^2/\text{g}$ is found to be too weak to solve the too big to fail problem. Simulated halos were too similar to those in CDM simulations, presenting too many large substructures inconsistent with the observed Milky Way dwarf spheroidals. In order to alleviate this problem, self-interactions should be $1 \lesssim \sigma_{\chi\chi}/m_{\chi} \lesssim 10 \text{ cm}^2/\text{g}$. These results are shown in figure 1.9. This constraint is in tension with those mentioned above, therefore there is only a small window open, at about $\sigma_{\chi\chi}/m_{\chi} \sim 0.5 - 1 \text{ cm}^2/\text{g}$, for velocity independent SIDM models to work as a solution to CDM small scale controversies.

Independently of these constraints, SIDM models can be probed by high energy neutrinos produced in dark matter annihilation in the Sun [19]. Interestingly, due to the self-interactions, the dark matter that is already capture in the Sun gravitation potential well would act as additional targets, effectively increasing the dark matter capture. This effect enhances the dark matter annihilation rate, potentially increasing the expected detectable signals in neutrino telescopes in the Earth.

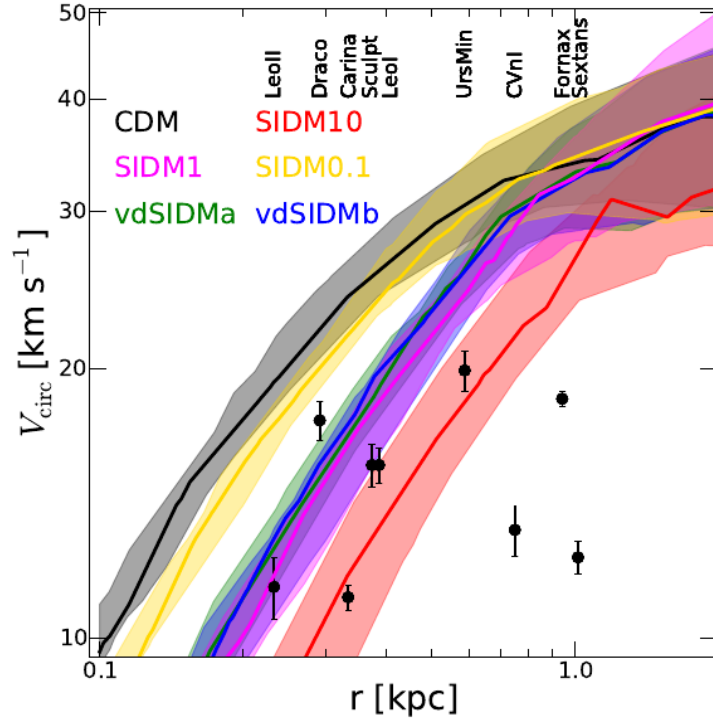


Figure 1.9: Circular velocity profiles of the 15 largest subhalos for several SIDM models and CDM. It can be seen that for a constant SIDM with $\sigma_{\chi\chi}/m_\chi = 0.1 \text{ cm}^2/\text{g}$ (yellow curve) the result is too similar to CDM (black curve), both being inconsistent with measurements for the dwarf spheroidals (black dots). The other SIDM models tested (both velocity independent and velocity dependent) show a better agreement with data, alleviating the too big to fail problem. Figure extracted from [26].

Our goal is to probe the SIDM models, by comparing our prediction for the neutrino flux, produced from dark matter annihilations in the Sun, to the available neutrino telescope observations.

Chapter 2

SIDM Capture and Annihilation in the Sun

In this chapter we first describe the capture of dark matter particles by astrophysical objects such as the Sun due to their scattering with nucleons as well as with already captured dark matter particles. Then, we proceed describing the enhancement on the capture and annihilation rates due to dark matter self-interactions.

2.1 Dark matter capture rate due to interactions with the Sun's nuclei

The Sun, in its journey around the Milky Way's center, is immersed in the galactic halo, and dark matter particles might interact with the Sun's nuclei. If the dark matter particles lose enough energy in these interactions they can not escape from the Sun's gravitational potential and are captured by the Sun. In this section we estimate the dark matter capture rate following the procedure described in [85, 86].

As the dark matter - nucleus interaction cross section, $\sigma_{\chi n}$, is very small, its interaction probability is also very low: $n\sigma_{\chi n}R_{\odot} \ll 1$ (n being the Sun's numerical density and R_{\odot} its radius). This implies that dark matter particles would at maximum interact once while passing through the Sun. In order to be captured, they should lose enough energy in this interaction, and have their speed reduced to less than the escape velocity at the point of interaction $v(r)$. Thus, it is useful to define $\Omega_v^-(w)$ as the probability per unit time that an incoming dark matter particle with velocity w will scatter to a velocity less than v while traveling through a solar spherical shell. In order to obtain the rate of dark matter particles passing through the Sun scaled by the capture probability, we consider a thin spherical shell of the Sun, with radius r and thickness dr . We also assume that the gravitational field at an imaginary spherical surface with large radius R , is negligible. At this distance away from the Sun, the dark matter velocity distribution is given by

$f(\vec{u}) d^3\vec{u}$.

At the imaginary surface $f(u) = 4\pi u^2 f(\vec{u})$ and the number of dark matter particles entering an area element $d\hat{S}$ per unit time, with velocity between u and $u + du$, is

$$f(\vec{u}) d^3\vec{u} \vec{u} \cdot \hat{n} dS = \frac{1}{4} f(u) u du d\cos^2\theta, \quad 0 \leq \theta \leq \frac{\pi}{2} \quad (2.1)$$

where θ is the angle between the element area $d\hat{S}$ and the incoming dark matter particle. It is convenient to change variables to the angular momentum per unit mass: $J = Ru \sin(\theta)$,

$$d\cos^2\theta du = \left| \frac{\partial(\cos^2\theta, u)}{\partial(u, J)} \right| du dJ = \frac{du dJ^2}{u^2 R^2}. \quad (2.2)$$

Summing over all surface area elements, we obtain the total number of incoming dark matter particles per unit time,

$$\pi f(u) \frac{du}{u} dJ^2. \quad (2.3)$$

The dark matter velocity at the spherical shell in the Sun is $w = (u^2 + v^2)^{1/2}$, where u is its velocity at infinity. For this particle to be captured, it must end up with a velocity less than v after the interaction with a Sun's nucleus. The probability for this is given by

$$\Omega_v^-(w) \times \frac{dl}{w}, \quad (2.4)$$

where $dl = dr / \cos\theta = dr [1 - (J/rw)^2]^{-1/2}$ is the distance traveled by the particle across the shell and then dl/w is the total time it spends in the solar shell:

$$\frac{dl}{w} = \frac{1}{w} \frac{dr}{\sqrt{1 - (J/rw)^2}} \times 2\Theta(rw - J), \quad (2.5)$$

where Θ is the Heaviside step function. The factor $2\Theta(rw - J)$ comes in because the particles will intersect the solar shell twice or not at all, depending on their angular momentum being $J < rw$ or $J > rw$ respectively.

The number of dark matter particles captured per unit time with velocities between u and $u + du$ has therefore to be scaled by the probability represented in equation (2.4):

$$2\pi \frac{f(u)}{u} du dr \Omega_v^-(w) \frac{1}{w} \int dJ^2 \frac{\Theta(rw - J)}{\sqrt{1 - (J/rw)^2}}, \quad (2.6)$$

which integrated in J gives:

$$4\pi r^2 dr \frac{f(u) du}{u} w \Omega_v^-(w). \quad (2.7)$$

Thus the total dark matter capture rate per unit shell volume is given by:

$$\frac{dC}{dV} = \int_0^\infty du \frac{f(u)}{u} w \Omega_v^-(w). \quad (2.8)$$

In order to obtain the capture probability rate $\Omega_v^-(w)$, we consider that the solar shell is made out of nuclei with mass m_N . The transferred energy in a dark matter - nucleus interaction is $\Delta E = \frac{m_\chi^2 m_N}{(m_\chi + m_N)^2} w^2 (1 - \cos \theta')$, where θ' is the scattering angle in the center of momentum frame and m_χ is the dark matter mass. By taking the extreme values of $\cos \theta'$, the fractional dark matter energy loss in a collision, $\Delta E/E$, falls in the interval

$$0 \leq \frac{\Delta E}{E} \leq 4 \frac{\mu}{(\mu + 1)^2}, \quad (2.9)$$

where $\mu = m_\chi/m_N$. Since the dark matter - nucleus scattering is isotropic, the distribution of energy loss is uniform over all the interval. This loss has to be such that the dark matter particle velocity is less than v after the collision:

$$\frac{w^2 - v^2}{w^2} = \frac{u^2}{w^2} \leq \frac{\Delta E}{E} \leq 4 \frac{\mu}{(\mu + 1)^2}. \quad (2.10)$$

Therefore, the probability for a dark matter particle transfer sufficient energy in an interaction, so that it ends up captured, is given by the ratio of these two intervals' sizes:

$$\frac{(\mu + 1)^2}{4\mu} \left(\frac{4\mu}{(\mu + 1)^2} - \frac{u^2}{w^2} \right) \Theta \left(\frac{4\mu}{(\mu + 1)^2} - \frac{u^2}{w^2} \right), \quad (2.11)$$

where the Heaviside function just ensures the right order of the extreme values of the interval. Then, to finally obtain the capture probability rate $\Omega_v^-(w)$, we simply multiply the total scattering rate, $\sigma n w$, by the conditional probability of capture given by equation (2.11):

$$\Omega_v^-(w) = \frac{\sigma n}{w} \left(v^2 - \frac{(\mu - 1)^2}{4\mu} u^2 \right) \Theta \left(v^2 - \frac{(\mu - 1)^2}{4\mu} u^2 \right). \quad (2.12)$$

Now, the only missing term in the equation (2.8) is the dark matter velocity distribution, which we assume is given by a Maxwell-Boltzmann distribution:

$$f(u) du = n_\chi \frac{4}{\sqrt{\pi}} x^2 \exp(-x^2) dx, \quad (2.13)$$

where n_χ is the dark matter numerical density and x is the dimensionless velocity

$$x^2 \equiv \frac{m_\chi}{2kT_\chi} u^2, \quad (2.14)$$

with T_χ being the dark matter temperature. In this distribution the mean square velocity is $\bar{v}^2 = 3kT_\chi/m_\chi$. In order to take into account the velocity of the Sun \tilde{v} , this distribution

becomes:

$$f_\eta(u) = f(u) \exp(-\eta^2) \frac{\sinh(2x\eta)}{2x\eta}, \quad (2.15)$$

where η is the dimensionless velocity of the Sun ($v_\odot = 220$ km/s)

$$\eta^2 \equiv \frac{m_\chi}{2kT_\chi} v_\odot^2. \quad (2.16)$$

Conveniently defining

$$A^2 \equiv \frac{3v^2}{2\bar{v}^2} \frac{4\mu}{(\mu-1)^2}, \quad (2.17)$$

the capture probability rate (equation (2.12)) is given by

$$\Omega_v^-(w) = \frac{1}{w} \frac{\sigma n v^2}{A^2} (A^2 - x^2) \Theta(A - x). \quad (2.18)$$

Using equations (2.8) and (2.18) and integrating over x , one obtains:

$$\frac{dC}{dV} = \left(\frac{6}{\pi}\right)^{\frac{1}{2}} \sigma n n_\chi \bar{v} \frac{v^2}{\bar{v}^2} \left[1 - \frac{1 - \exp(-A^2)}{A^2}\right], \quad (2.19)$$

under the assumption that the dark matter velocity distribution given by equation (2.13), which is valid only for capture by astrophysical objects at rest in relation to the dark matter distribution. For the Sun we consider the distribution given by equation (2.15), and we obtain:

$$\begin{aligned} \frac{dC}{dV} = & \left(\frac{6}{\pi}\right)^{\frac{1}{2}} \sigma n n_\chi \bar{v} \frac{v^2}{\bar{v}^2} \frac{1}{2\eta A^2} \left[\left(A_+ A_- - \frac{1}{2} \right) [\chi(-\eta, \eta) - \chi(A_-, A_+)] \right. \\ & \left. + \frac{1}{2} A_+ e^{-A_-^2} - \frac{1}{2} A_- e^{-A_+^2} - \eta e^{-\eta^2} \right], \end{aligned} \quad (2.20)$$

where

$$\chi(a, b) \equiv \int_a^b \exp(-y^2) dy = \frac{\pi^{1/2}}{2} [\text{erf}(b) - \text{erf}(a)] \quad (2.21)$$

and $A_\pm \equiv A \pm \eta$.

Finally, the total dark matter capture rate is determined by integrating over all the Sun's volume:

$$C = \int_0^{R_\odot} 4\pi r^2 dr \frac{dC(r)}{dV}, \quad (2.22)$$

where R_\odot is the Sun's radius. It is worth noting that dC/dV depends on the distance from the Sun's center r through the escape velocity $v(r)$ and the Sun's nucleus numerical density $n(r)$.

It is also important to note that in this calculation only one nuclear specie was considered. For a precise estimative of the dark matter capture in the Sun, the composition and

distribution of its several elements must be taken into account. With these considerations, the total dark matter capture rate is given by [86]:

$$C = 4.8 \times 10^{24} \text{ s}^{-1} \frac{\rho_\chi}{0.3 \text{ GeV/cm}^3} \left(\frac{270 \text{ km/s}}{\bar{v}_\chi} \right) \left(\frac{\text{GeV}}{m_\chi} \right) \sum_i \left[F_i(m_\chi) \left(\frac{\sigma_{\chi N_i}}{10^{-40} \text{ cm}^2} \right) f_i \phi_i S(m_\chi/m_{N_i}) \left(\frac{\text{GeV}}{m_{N_i}} \right) \right], \quad (2.23)$$

where ρ_χ is the local dark matter density, \bar{v}_χ is the velocity distribution dispersion and m_χ is the dark matter mass. The sum is over all the nuclear species N_i that compose the Sun, m_{N_i} is their corresponding mass, f_i is the mass fraction of the element i and $\sigma_{\chi N_i}$ is the scalar interaction cross section between a dark matter particle χ and a nucleus N_i . The quantities ϕ_i describe the distribution of the element i in the Sun. The values used for ϕ_i and f_i for the ten most abundant elements are listed in the table 2.1 and were extracted from [86] and [87] respectively. $S(m_\chi/m_{N_i})$ is the kinematic suppression factor for dark matter capture from a nucleus N_i :

$$S(x) = \left[\frac{A^b}{1 + A^b} \right]^{1/b}, \quad (2.24)$$

where

$$A = \frac{3}{2} \frac{x}{(x-1)^2} \left(\frac{\langle v_{\text{esc}} \rangle^2}{\bar{v}^2} \right) \quad (2.25)$$

and $b = 1.5$. The quantity $\langle v_{\text{esc}} \rangle$ is the mean escape velocity, which for the Sun is $\langle v_{\text{esc}} \rangle = 1156 \text{ km/s}$. Note that for $x = m_\chi/m_{N_i} \rightarrow 1 : S(x) \rightarrow 1$, but for $x \rightarrow \infty$ and $x \rightarrow 0 : S(x) \rightarrow 0$. In other words, capture is kinematically suppressed if the dark matter mass differs considerably from the nuclear mass, and there is no suppression when the two masses are similar. $F_i(m_\chi)$ is the form-factor suppression of dark matter capture from a nucleus with mass m_{N_i} . For hydrogen, the form factor suppression is $F_H(m_\chi) = 1$. For the other elements we used the following expression [86]:

$$F_i(m_\chi) = F_i^{\text{inf}} + (1 - F_i^{\text{inf}}) \exp \left[- \left(\frac{\ln m_\chi}{\ln m_c^i} \right)^{\alpha_i} \right], \quad (2.26)$$

where F_i^{inf} , m_c^i and α_i are listed in the table 2.2. Finally, in the equation (2.23), $\sigma_{\chi N_i}$ is the scattering cross section between a dark matter particle and the nucleus N_i . We use the relation:

$$\sigma_{\chi N_i} = A_i^2 \left(\frac{m_{\chi N_i}}{m_{\chi n}} \right)^2 \sigma_{\chi n}, \quad (2.27)$$

where we are assuming that the dark matter interacts equally with protons and neutrons. In this last relation $m_{\chi N_i}$ and $m_{\chi n}$ are the dark matter - nucleus and dark matter - nucleon reduced masses, and A_i is the atomic mass number of the i element.

Table 2.1: Solar composition

Element	A_i	f_i [87]	ϕ_i [86]
H	1	0.7352	3.16
He	4	0.2485	3.4
C	12	2.36×10^{-3}	3.23
N	14	6.91×10^{-4}	3.23
O	16	5.72×10^{-3}	3.23
Ne	20	1.25×10^{-3}	3.23
Mg	24	7.06×10^{-4}	3.23
Si	28	6.63×10^{-4}	3.23
S	32	3.08×10^{-4}	3.23
Fe	56	1.29×10^{-3}	3.23

Table 2.2: Parameters for form-factor suppression in the Sun [86]

Element	m_c^i (GeV)	F_i^{inf}	α_i
He	18.2	0.986	1.58
C	61.6	0.788	2.69
N, O, Ne	75.2	0.613	2.69
Mg, Si	71.7	0.281	2.97
S	57.0	0.101	3.1
Fe	29.3	0.00677	3.36

We used the equation (2.23) with $\bar{v} = 270$ km/s and $\rho_\chi = 0.4$ GeV [88, 89] in the case of spin-independent dark matter - nucleon interactions. In figure 2.1 we show the total dark matter capture rate for $\sigma_{\chi n} = 10^{-44}$ cm² as well as the contributions from some elements.

In the case of spin-dependent interactions, the capture will be mainly due to interactions with hydrogen. In this case there is no significant form factor suppression and the capture rate will be given by [86]:

$$C^{\text{sd}} = 1.3 \times 10^{25} \text{ s}^{-1} \frac{\rho_\chi}{0.3 \text{ GeV/cm}^3} \left(\frac{270 \text{ km/s}}{\bar{v}_\chi} \right) \left(\frac{\text{GeV}}{m_\chi} \right) \left(\frac{\sigma_{\chi\text{H}}}{10^{-40} \text{ cm}^2} \right) S(m_\chi/m_{\text{H}}). \quad (2.28)$$

In figure 2.2 we show comparatively both the spin-independent and spin-dependent capture rates independently of the dark matter - nucleon cross section. In this case we also used $\bar{v} = 270$ km/s and $\rho_\chi = 0.4$ GeV.

2.2 Dark matter capture rate due to self-interactions

Once dark matter particles are captured by the Sun's gravitational potential, as described in the section before, they start to accumulate in the Sun's core due to the successive

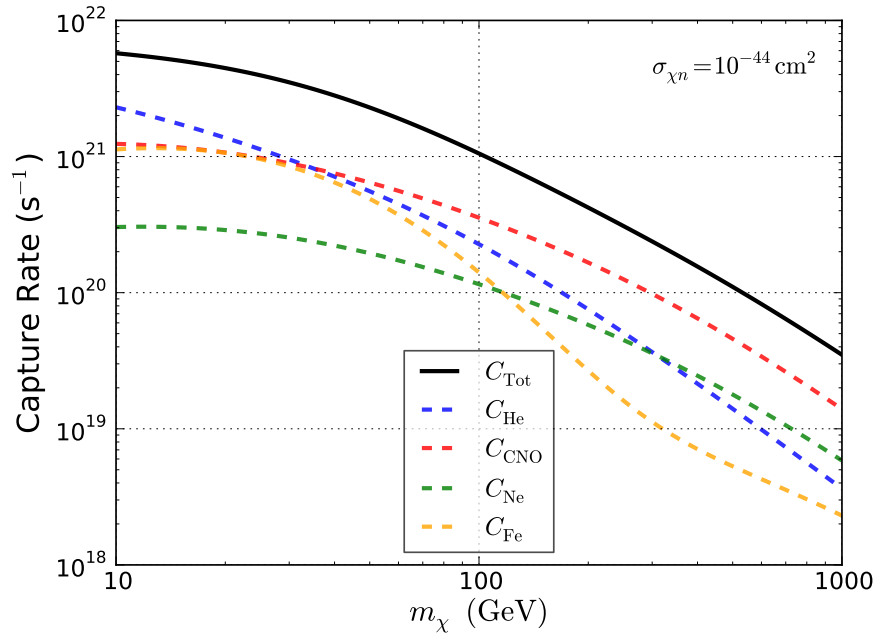


Figure 2.1: Dark matter capture rate in the Sun. It is shown the total dark matter capture rate for $\sigma_{\chi n} = 10^{-44} \text{ cm}^2$ as well as the contribution to the capture rate for some elements.

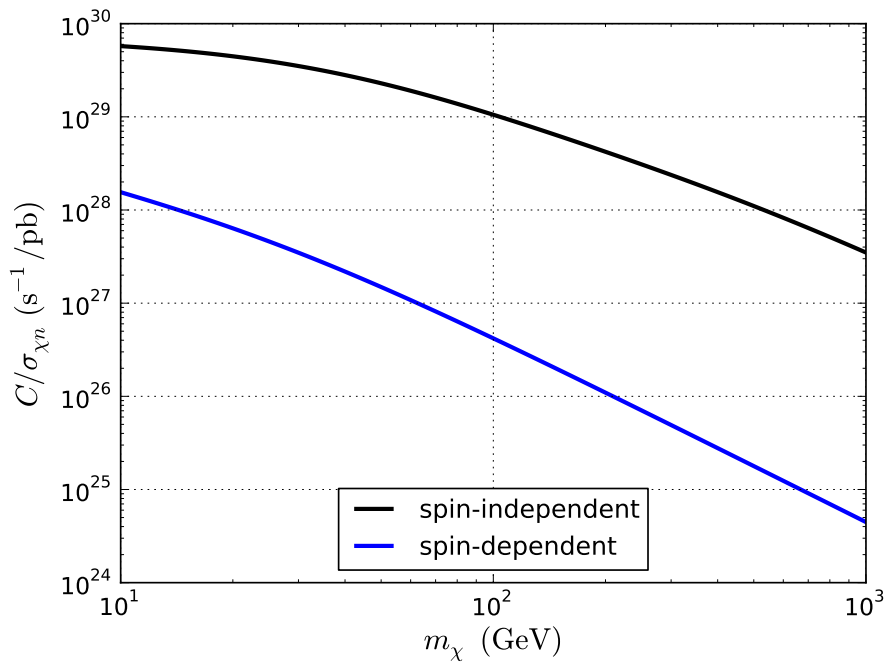


Figure 2.2: Dark matter capture rate in the Sun for spin-independent and spin-dependent interactions. In the case of spin-dependent interactions, only interactions with hydrogen were considered.

energy loss that result from additional interactions with the Sun's nuclei. In the scenario that we are considering, where dark matter particles have self-interactions in addition to their weak couplings to the SM, the dark matter particles traversing the Sun could interact with those dark matter particles already captured. In the same way as before, if the incoming particles lose sufficient energy in these scatterings, they would not be able to escape from the Sun's gravitational potential and become captured. In this section, we will obtain this additional capture rate following the same procedure as the section above.

The steps of the calculation are exactly the same but with a different probability rate $\Omega_v^-(w)$. So we arrive at the same expression for the differential capture rate per volume as equation (2.8),

$$\frac{dC}{dV} = \int_0^\infty du \frac{f(u)}{u} w \Omega_v^-(w). \quad (2.29)$$

but in this case $\Omega_v^-(w)$ have a simpler form since now it accounts for dark matter - dark matter scattering.

The fractional energy loss in a scattering between dark matter particles falls in the interval

$$0 \leq \frac{\Delta E}{E} \leq 1. \quad (2.30)$$

On the other hand, a particle, in order to be captured, should scatter off from velocity w to a velocity less than the escape velocity v . Thus, it is required an energy loss of at least:

$$\frac{w^2 - v^2}{w^2} = \frac{u^2}{w^2} \leq \frac{\Delta E}{E}. \quad (2.31)$$

Then again, considering a uniform distribution of the energy loss, the probability for a dark matter particle to lose enough energy is given by the ratio of these intervals

$$1 - \frac{u^2}{w^2} = \frac{v^2}{w^2}. \quad (2.32)$$

Finally, the probability rate $\Omega_v^-(w)$ is the product of the total rate of scattering $\sigma_{\chi\chi}nw$ (note that in this case $\sigma_{\chi\chi}$ is the elastic dark matter self-interacting cross section and n the numerical dark matter density in the Sun) by the above conditional probability (equation (2.32)):

$$\Omega_v^-(w) = \sigma_{\chi\chi}n \frac{v^2}{w}. \quad (2.33)$$

Then, with this result and using the same dark matter velocity distribution as in the section before (equation (2.15)):

$$f(x) = \frac{2n_\chi}{\sqrt{\pi}} x^2 e^{-x^2} e^{-\eta^2} \frac{\sinh(2x\eta)}{x\eta}, \quad (2.34)$$

where $x^2 = \frac{3}{2}(u/\bar{v})^2$ and $\eta^2 = \frac{3}{2}(v_\odot/\bar{v})^2$, and after integrating over the speed distribution

we get:

$$\frac{dC}{dV} = \sqrt{\frac{3}{2}} n_\chi n \sigma_{\chi\chi} \frac{v^2(r)}{\bar{v}} \frac{\text{erf}(\eta)}{\eta}. \quad (2.35)$$

In this equation we explicitly wrote the velocity escape dependence on the distance from the Sun's center $v = v(r)$.

To obtain the total dark matter self-capture rate we need to integrate over the Sun's volume.

$$C = \sqrt{\frac{3}{2}} n_\chi \sigma_{\chi\chi} \frac{v^2(R_\odot)}{\bar{v}} \frac{\text{erf}(\eta)}{\eta} \int_0^{R_\odot} 4\pi r^2 n \frac{v^2(r)}{v^2(R_\odot)} dr. \quad (2.36)$$

This last integral can be rewritten conveniently defining the dimensionless gravitational potential $\hat{\phi} = v^2(r)/v^2(R_\odot)$. We then obtain:

$$C = \sqrt{\frac{3}{2}} n_\chi \sigma_{\chi\chi} \frac{v^2(R_\odot)}{\bar{v}} N_\chi \langle \hat{\phi} \rangle \frac{\text{erf}(\eta)}{\eta} \quad (2.37)$$

where N_χ is the number of dark matter particles already captured and $\langle \hat{\phi} \rangle$ is the average gravitational potential for dark matter in the Sun. Since dark matter occupy the most inner part of the Sun, we have $\langle \hat{\phi} \rangle \simeq 5.1$ [85].

There is one additional complication in the calculation of the dark matter self-capture rate. It could happen that in the scattering between the dark matter particles, the particle that was already captured gain enough energy to escape from the Sun. This would result in no net gain in the amount of captured dark matter particles. To take this into account, we must require that in order to a particle be counted as captured it must lose energy not only higher than $u^2/w^2 \leq \Delta E/E$, as in equation (2.31), but also lower than $\Delta E/E \leq v^2/w^2$. With this consideration we recalculate the probability rate of capture $\Omega_v^-(w)$ obtaining:

$$\Omega_v^-(w) = \sigma_{\chi\chi} n \frac{v^2 - u^2}{w}. \quad (2.38)$$

So, this modification would be unimportant when $v(r) \gg u$ which is just the case for dark matter self-capture in the Sun. Considering the dark matter speed distribution, most of the particles have velocities $u < v(R_\odot) = 617.5$ km/s. However this is not the case for smaller astrophysical objects such as the Earth which has a escape velocity $v(R_\oplus) = 11.2$ km/s. Therefore, in the Earth most of the dark matter self-scatterings that would lead to the capture of the infalling particle, would eject the target.

2.3 Dark matter annihilation rate

As already mentioned, once the dark matter particles are captured, due to dark matter - nucleon or dark matter self-interactions, they concentrate in the Sun's core. There they can annihilate producing standard model particles, which reduces the amount of

dark matter present in the Sun. Thus, the time evolution of the number of dark matter particles in the Sun, N_χ , is determined by capture and annihilation Γ_a rates competition, given by

$$\frac{dN_\chi}{dt} = C_c + C_s N_\chi - 2\Gamma_a, \quad (2.39)$$

where C_c is the dark matter capture rate due to interactions with nuclei, given by equation (2.23) if interactions are spin-independent or equation (2.28) if they are spin-dependent, $C_s N_\chi$ is the dark matter self-capture rate (equation (2.37)). The factor 2 accompanying Γ_a appears because dark matter annihilates in pairs. In this equation we are not considering the effect of dark matter evaporation, since it is only important for low masses $m_\chi \lesssim 4$ GeV [90], and we are focusing on dark matter masses above 20 GeV.

The annihilation rate can be written as

$$\Gamma_a = \frac{1}{2} C_a N_\chi^2, \quad (2.40)$$

where $C_a = \langle \sigma_a v \rangle V_2 / V_1^2$. $\langle \sigma_a v \rangle$ is the thermal average annihilation cross section times relative velocity and, for dark matter produced as a thermal relic, is determined by the dark matter cosmological abundance, which gives $\langle \sigma_a v \rangle \sim 3 \times 10^{-26}$ cm³/s. V_j are effective volumes of the Sun as obtained in [91]: $V_j = 2.44 \times 10^{27} (\frac{100 \text{ GeV}}{j m_\chi})^{3/2}$ cm³, considering a thermal distribution at an effective solar core temperature $T = 1.57 \times 10^7$ K [92]. This assumption is reasonable for dark matter masses $m_\chi \gtrsim 10$ GeV [93].

In the standard collisionless CDM case, where self-interactions are non-existent ($C_s = 0$), the solution to equation (2.39) is

$$N_\chi^{\text{CDM}} = \sqrt{\frac{C_c}{C_a}} \tanh(\sqrt{C_c C_a} t). \quad (2.41)$$

Hence, there is a time scale for the equilibrium between dark matter capture and annihilation, $\tau_{\text{eq}} = 1/\sqrt{C_c C_a}$. For most cases of interest, the time scale for equilibrium is much less than the age of the Sun: $\tau_{\text{eq}} \ll \tau_\odot$. In this case, the solution has approached a steady state

$$N_{\chi, \text{eq}}^{\text{CDM}} = \sqrt{\frac{C_c}{C_a}}. \quad (2.42)$$

Therefore, the annihilation rate would also be time independent

$$\Gamma_{a, \text{eq}}^{\text{CDM}} = \frac{1}{2} C_a (N_{\chi, \text{eq}}^{\text{CDM}})^2 = \frac{1}{2} C_c, \quad (2.43)$$

and does not depend in the annihilation rate coefficient C_a . Thus, the dark matter annihilation rate depends only on the capture rate and is independent of its annihilation cross section, provided the latter is large enough to reach the equilibrium.

The solution when dark matter self-interactions are taken into account is

$$N_{\chi}^{\text{SIDM}} = \frac{C_c \tanh(t/\zeta)}{\zeta^{-1} - \frac{C_s}{2} \tanh(t/\zeta)}, \quad (2.44)$$

where

$$\zeta = \frac{1}{\sqrt{C_c C_a + C_s^2/4}}. \quad (2.45)$$

This result was first presented in [19]. The steady state solution is reached for $t \gg \zeta$, in this case

$$N_{\chi,\text{eq}}^{\text{SIDM}} = \frac{C_s}{2C_a} + \sqrt{\frac{C_s^2}{4C_a^2} + \frac{C_c}{C_a}}. \quad (2.46)$$

Clearly, equation (2.46) reduces to equation (2.42) when $C_s = 0$ as it should. When self-interactions are dominant, $C_s \gg C_s C_a$, we have that

$$N_{\chi,\text{eq}}^{\text{SIDM}} \approx \frac{C_s}{C_a} \quad (2.47)$$

and the annihilation rate is

$$\Gamma_{a,\text{eq}}^{\text{SIDM}} = \frac{1}{2} C_a (N_{\chi,\text{eq}}^{\text{SIDM}})^2 \approx \frac{C_s^2}{2C_a} \quad (2.48)$$

Therefore, in this case, both N_{χ} and Γ_a are independent of the capture rate due to interactions with Sun's nuclei. Also, both quantities are inverse proportional to C_a . Thus, SIDM models with a low annihilation cross section will have a larger annihilation rate.

In figure 2.3 we present the number of dark matter particles in the Sun as a function of time (in units of the Sun's age, t_{\odot}) for two dark matter self-interaction cross sections $\sigma_{\chi\chi} = 3 \times 10^{-22} \text{ cm}^2$ (left) and $\sigma_{\chi\chi} = 10^{-23} \text{ cm}^2$ (right). The solid curves correspond to collisionless CDM while the dashed curves to SIDM models. The different colors correspond to different values of $\sigma_{\chi n}$, as indicated in the figure legend. For CDM, the steady state has been reached for all cases except for the weakest $\sigma_{\chi n} = 10^{-47} \text{ cm}^2$ (red curve). The most important result is that self-interactions significantly increase the amount of dark matter captured and accelerates the equilibrium between the capture and annihilation processes. Self-interactions can even bring to equilibrium solutions that otherwise would not (red dashed curve in left plot). The fact that when $\sigma_{\chi\chi}$ is strong enough N_{χ} becomes independent of $\sigma_{\chi n}$ can be seen through the convergence of the red and green dashed curves in the left plot.

The increment in the amount of dark matter particles captured present in SIDM models consequently leads to an enhancement in the annihilation rate (equation (2.40)). Therefore, we expect a larger flux of dark matter annihilation products for SIDM than for CDM. For each particular SIDM model considered in this work, we will use equations

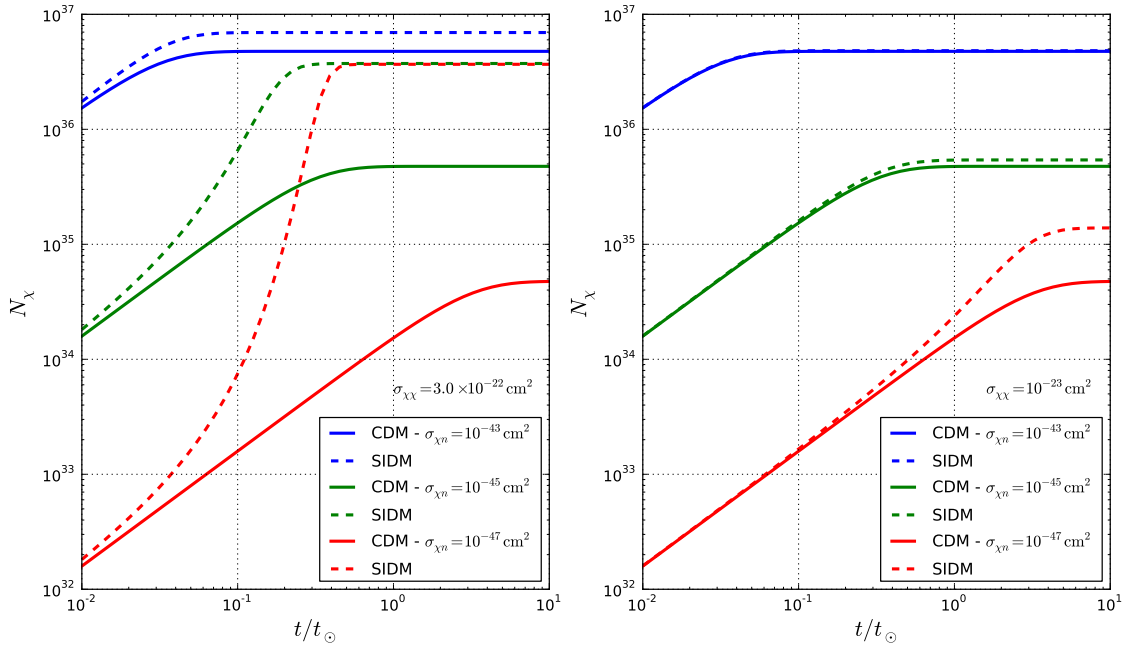


Figure 2.3: Time evolution of dark matter particles in the Sun. Solid curves are for collisionless CDM and dashed curves for SIDM models. The left plot correspond to $\sigma_{\chi\chi} = 3 \times 10^{-22} \text{ cm}^2$ while the right plot to $\sigma_{\chi\chi} = 3 \times 10^{-23} \text{ cm}^2$. The colors indicate the dark matter - nucleon cross section $\sigma_{\chi n}$ value as labeled in the legend.

(2.40) and (2.44) to determine the number of annihilations occurring in the Sun's core. This will be used later to obtain the expected neutrino signal for these models.

Chapter 3

Neutrino Flux from SIDM Annihilation

Dark matter particles in the Sun's core can annihilate in pairs into Standard Model particles like quarks, leptons and gauge bosons. The produced particles will generate another ones through hadronization, interactions in the Sun and decays. Among the products, the neutrinos will be of most importance. This is because their low interaction cross section allows them to escape the Sun and reach the Earth, where they can be detected by underground experiments serving as dark matter probes as noted in early works such as [94, 95].

To obtain the dark matter induced neutrino flux at neutrino detectors we will need to keep track of the neutrino propagation from the Sun's core to the Earth, 1.50×10^8 km away. In their travel, neutrino - nucleon interactions and oscillations will affect the energy spectrum. We will consider these effects using the WimpSim simulation package described below.

3.1 Neutrino Propagation from the Sun to the Earth with WimpSim

The WimpSim code simulates the dark matter annihilation in the center of the Sun and the propagation of the neutrinos produced in such annihilations in an event based framework [96]. This means that it follows each neutrino from their creation, at the Sun's core, to their arrival at detectors in the Earth. For this process, it includes the effects of neutrino oscillations in matter and vacuum, the neutrino interactions with nucleons via charge current and neutral current interactions, and also it takes into account neutrino regeneration from τ decay.

The WimpSim code is written in the programming language Fortran and is publicly available at [97]. The program is divided into two parts, WimpAnn and WimpEvent. The

first, WimpAnn, simulates the dark matter annihilation in the Sun and propagates the neutrinos produced until 1 AU¹ from the Sun. The main output of WimpAnn is a list specifying all neutrino states, described by their state vector

$$\nu = \begin{pmatrix} a_e \\ a_\mu e^{i\phi_\mu} \\ a_\tau e^{i\phi_\tau} \end{pmatrix}, \quad (3.1)$$

the neutrino energy and if its a particle or anti-particle. The second program, Wimp-Event, uses this list to continue the neutrinos propagation to the actual detector location in the Earth. To do this, the detector position and time of the events have to be known. The main output is an event list with the energy and angles of the incoming neutrinos and the outgoing leptons and hadronic showers produced in the neutrino interactions.

3.1.1 Dark Matter Annihilation in the Sun

Dark matter particles captured in the Sun can annihilate producing Standard Model particles. The annihilation channels that can be simulated in Wimpsim include quarks ($d\bar{d}, u\bar{u}, s\bar{s}, c\bar{c}, b\bar{b}, t\bar{t}$), gauge bosons (gg, W^+W^-, Z^0Z^0) and leptons ($\mu^-\mu^+, \tau^-\tau^+, \nu_e\bar{\nu}_e, \nu_\mu\bar{\nu}_\mu, \nu_\tau\bar{\nu}_\tau$). To simulate the hadronization and decay of the annihilation products and collect the neutrinos and antineutrinos produced, WimpSim uses the event generator Pythia 6.4 [98].

In this work we will consider two annihilation channels, dark matter annihilating into W^+W^- (or $\tau^+\tau^-$ if $m_\chi < m_W$) and into $b\bar{b}$. These channels were chosen since their decay chain produces neutrinos in a wide energy range. They are also the channels analyzed by the IceCube collaboration, so this will allow us to make a direct comparison of our results with theirs.

The process for the $b\bar{b}$ channel is a bit different because these quarks hadronize forming B mesons that, for the case of the Sun, interact before they decay. Wimpsim takes this process into account in an approximate way. First, it performs the simulation in Pythia as in free space, and then rescale the energy of the produced neutrinos estimating the B mesons energy loss due to their interactions in the Sun [93, 99].

In figure 3.1 we show the obtained neutrino spectra at creation in the Sun for both annihilation channels, $b\bar{b}$ (left) and W^+W^- (right). As expected, the W^+W^- channel produces a higher flux of high energy neutrinos than the $b\bar{b}$ channel.

¹1 astronomical unit $\approx 1.50 \times 10^8$ km, Earth's mean distance to the Sun.

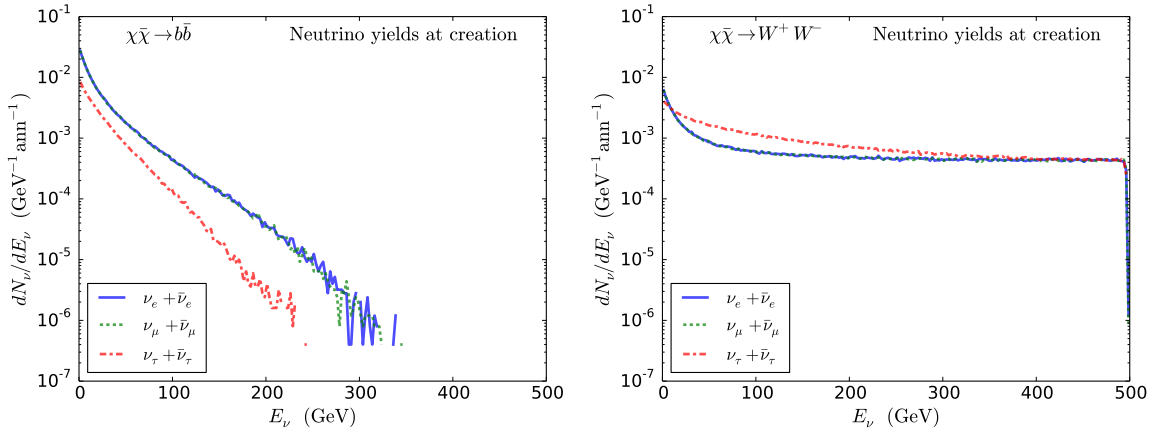


Figure 3.1: Neutrino yields at creation in the Sun’s core. The three flavor neutrino spectra is shown for dark matter with $m_\chi = 500$ GeV annihilating into $b\bar{b}$ (left) and W^+W^- (right).

3.1.2 Neutrino Interactions and Oscillations

Once the high energy neutrinos are produced, they will propagate out from the Sun’s center. In this travel the neutrinos could experience interactions with nucleons and neutrino oscillations.

Neutrinos can interact with nucleons via charge current (CC) and neutral current (NC) interactions. In a CC interaction, a charge lepton is produced while in a NC interaction, a neutrino with degraded energy is obtained. The cross sections of these processes are calculated since they are needed to determine the interaction probabilities and the leptons’ energy loss. The former will be used in WimpSim to determine if an interaction occurs when the neutrino is traversing the Sun and/or the Earth in its way to the detector, while the latter are needed to account for the neutrino energy losses, their regeneration from τ decay and also, for calculating the scattering processes near or in the neutrino detector.

To calculate the neutrino - nucleon cross sections we use the CTEQ6-DIS parton distribution function [100, 101], which is the default in WimpSim. This calculations are done through the Nusigma package [102]. First, it is obtained a table of the cross sections for specific energy values, and from this the actual cross section, at the desired energy, is interpolated. This approach serves to gain computational speed. Nusigma also simulates the interaction, returning the energy and angles of the final state lepton and the hadronic shower.

To accurately obtain the neutrino yields at the Earth, WimpSim needs to also keep track of neutrino oscillations. These occur because the neutrino flavor eigenstates are different from the neutrino mass eigenstates. This is written as

$$|\nu_\alpha\rangle = \sum_a U_{\alpha a}^* |\nu_a\rangle, \quad (3.2)$$

where U is the leptonic mixing matrix, $|\nu_\alpha\rangle$ is a neutrino flavor eigenstate (ν_e, ν_μ or ν_τ), and $|\nu_a\rangle$ ($a = 1, 2$ or 3) are the neutrino mass eigenstates with definite mass m_a . The evolution of the neutrino state $\nu(t)$ is given by

$$\nu(t) = S(t)\nu(0), \quad (3.3)$$

where the evolution operator $S(t)$ is given by $S(t) = \exp(-iHt)$. H is the total hamiltonian, which includes both vacuum and the Mikheyev-Smirnov-Wolfenstein (MSW) potential terms

$$H = \frac{1}{2E}U \text{diag}(0, \Delta m_{21}^2, \Delta m_{31}^2) U^\dagger + \text{diag}(\sqrt{2}G_F N_e, 0, 0). \quad (3.4)$$

E is the neutrino energy, $\Delta m_{ij}^2 = m_i^2 - m_j^2$ are the neutrino mass squared differences, G_F is the Fermi coupling constant, and N_e is the electron number density in the medium.

To calculate the effect of neutrino oscillations during their propagation in the Sun and the Earth, WimpSim propagates the neutrinos by layers of constant electron number density. For oscillations in vacuum, only one layer with null electron number density is needed.

For our simulations we used the leptonic mixing matrix in its standard parametrization

$$U = \begin{pmatrix} c_{13}c_{12} & c_{13}s_{12} & s_{13}e^{-i\delta} \\ -s_{12}c_{23} - c_{12}s_{23}s_{13}e^{i\delta} & c_{12}c_{23} - s_{12}s_{23}s_{13}e^{i\delta} & s_{23}c_{13} \\ s_{12}s_{23} - c_{12}c_{23}s_{13}e^{i\delta} & -c_{12}s_{23} - s_{12}c_{23}s_{13}e^{i\delta} & c_{23}c_{13} \end{pmatrix}, \quad (3.5)$$

where $c_{ij} = \cos \theta_{ij}$, $s_{ij} = \sin \theta_{ij}$, and δ is the CP-violating phase. We used the WimpSim 3.05 standard values for the mixing parameters, which are based on PDG 2012 [103]:

$$\begin{aligned} \theta_{12} &= 33.58^\circ \\ \theta_{13} &= 9.12^\circ \\ \theta_{23} &= 40.40^\circ \\ \delta &= 0.0^\circ \\ \Delta m_{21}^2 &= 7.58 \times 10^{-5} \text{eV}^2 \\ \Delta m_{31}^2 &= 2.35 \times 10^{-3} \text{eV}^2. \end{aligned}$$

3.1.3 Neutrino Propagation

To propagate the neutrinos produced in dark matter annihilations it is necessary to know the solar composition and density. For this, WimpSim uses the Standard Solar Model [104], which gives the density of the most abundant elements and electrons as a function of the distance from the Sun's center. The element densities are needed to calculate the

neutrino interaction probabilities, and the electron densities to obtain the matter effect on neutrino oscillations.

The first step in the simulation is to attribute a creation point to each neutrino produced. This is done assuming a thermal distribution for the dark matter particles captured in the Sun. For masses of interest in this work, dark matter particles are concentrated to within 1% of the solar radius. Therefore the initial neutrino trajectories could be approximated as radial. After this step, the amount of matter that each neutrino should traverse to reach the Sun's surface is known. Then, the interaction cross sections are calculated and used to randomize where the neutrino interacts (if it interacts at all) and with what type of interaction.

In the case of CC interactions, first the flavor probabilities at the interaction point have to be determined (following the neutrino evolution operator method, briefly described above). According these probabilities, the actual interacting neutrino flavor is randomized. If the neutrino is a ν_τ , the interaction is simulated and a τ lepton is produced. Then, its decay is simulated with Pythia and the produced neutrinos are collected. These neutrinos proceed their propagation until reach the Sun's surface. On the other hand, if the interacting neutrino is a ν_e or ν_μ , then the CC interaction will produce an electron, which is stable, or a muon, which will be stopped before it has time to decay. As neither of these processes produce high energy neutrinos, so the interacting neutrino is considered absorbed.

For NC interactions, the relative phases among neutrino flavor eigenstates are preserved because the interaction is flavor blind. Then, the only effect of this type of interactions will be a neutrino energy change.

To take into account the effect of neutrino oscillations between the creation and interaction points, the Sun is divided in layers of constant density. WimpSim considers layers with a width of 0.3% of the solar radius, keeping the total error on the neutrino state at the end of propagation to less than 1%.

In figure 3.2 we show our results of neutrino propagation to the solar surface for both annihilation channels investigated $b\bar{b}$ (left) and W^+W^- (right). There are two significant things to note. First, there has been occurred a mixture between muon and tau neutrinos, while the electron neutrinos have remained basically unmixed. Second, there are more neutrinos at lower energies than in the original spectrum at creation (figure 3.1). This is because CC interactions create secondary neutrinos from τ decay and because of the neutrino energy loss in NC interactions. Additionally, the CC interactions create a loss of high energy neutrinos due to absorption of ν_e and ν_μ .

Once the neutrinos reach the Sun's surface they are propagated to a distance of 1 AU away from the Sun, taking into account neutrino oscillations in vacuum. At the end of this propagation, WimpSim saves the energy and their relative phase flavor for each neutrino. In figure 3.3 we show the neutrino spectra at this distance for both chosen annihilation

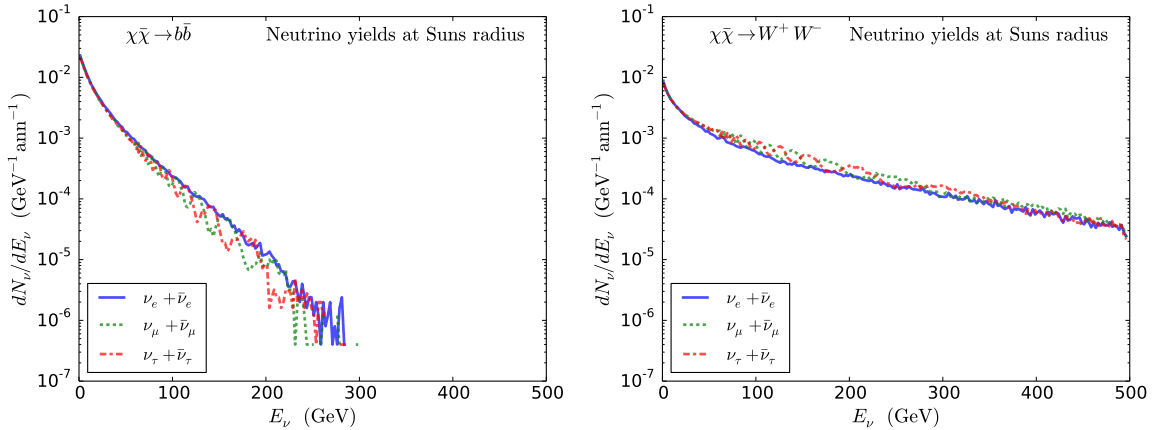


Figure 3.2: Neutrino yields at the solar surface. The three flavor neutrino spectra is shown for dark matter with $m_{\chi} = 500$ GeV annihilating into $b\bar{b}$ (left) and W^+W^- (right).

channels. We note that the ν_e are now mixed with the ν_{μ} and ν_{τ} . It is interestingly to note that despite some neutrino flavors were dominant at creation, at this propagation stage we essentially have equal amounts for each neutrino flavor.

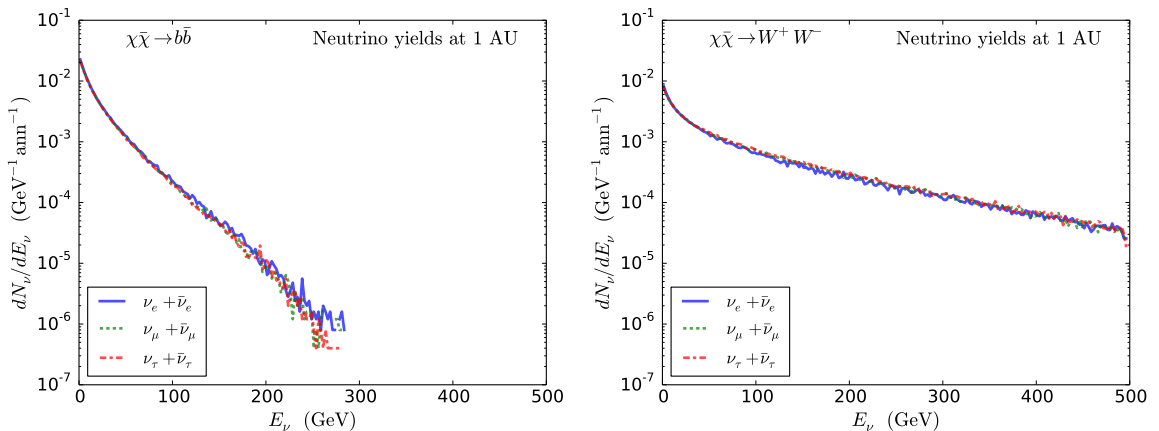


Figure 3.3: Neutrino yields at 1 AU from the Sun. The three flavor neutrino spectra is shown for dark matter with $m_{\chi} = 500$ GeV annihilating into $b\bar{b}$ (left) and W^+W^- (right).

The last propagation step is from 1 AU to the actual position of the detector in the Earth. To do this, it is necessary to know the detector location and the time that the events occur. This is required to determine the exact distance between the Sun and the Earth and also, the amount of matter that the neutrino will traverse across the Earth until it reaches the detector.

The propagation across the Earth is done in the same way as for the Sun. In this case WimpSim uses the Earth density profile from [105] to calculate the neutrino interactions

and matter oscillation effect. The neutrinos are propagated through layers with a width of 0.3% of the Earth radius.

Once the neutrinos reach the detector they are projected to their flavor eigenstates, according to their flavor phases. Then their interactions are simulated with Nusigma, producing charged leptons and hadronic showers. The neutrino yields at the detector are saved as well as the hadronic showers and leptons produced, including their angular and energy information.

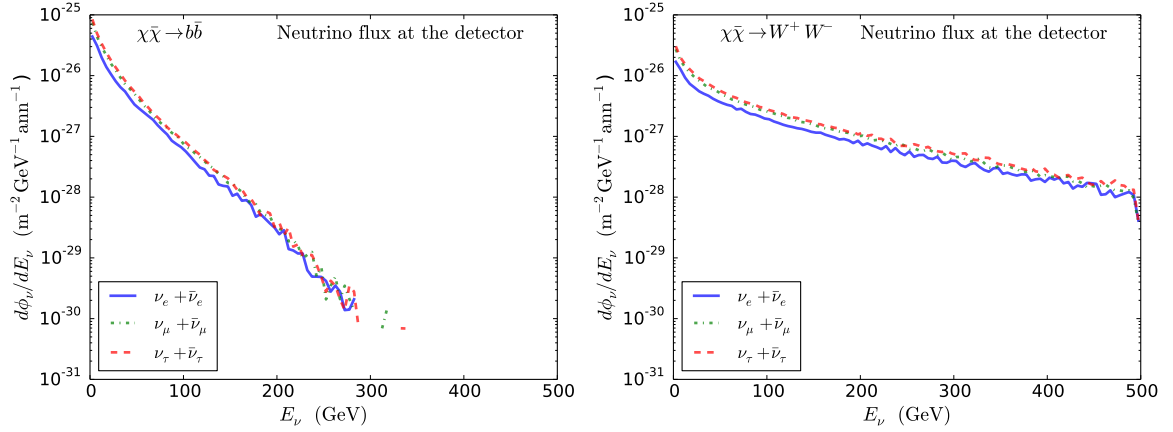


Figure 3.4: Neutrino yields at the detector. The three flavor neutrino spectra is shown for dark matter with $m_\chi = 500$ GeV annihilating into $b\bar{b}$ (left) and W^+W^- (right).

In figure 3.4 we show the neutrino flux at the IceCube detector. We have considered the time period between the Autumn and Spring equinoxes in the south hemisphere.

Chapter 4

Probing SIDM with IceCube Results

In this section we obtain the expected number of muon neutrino events at the IceCube detector originated from SIDM annihilation in the Sun. We will compare this to the last IceCube collaboration dark matter search result. From this comparison we will probe the parameter space of velocity-independent SIDM models.

4.1 Muon Neutrino Events at IceCube for SIDM Models

At the end of the last chapter we obtained the neutrino flux that reaches the IceCube detector, for all three neutrino flavors. For our analysis, we will only use the final muon neutrinos and antineutrinos. These are the same used by the IceCube collaboration when looking for dark matter annihilation in the Sun, due to their good angular direction reconstruction and background rejection.

For our investigation, we simulated dark matter annihilations with masses between $m_\chi = 20 \text{ GeV} - 5 \text{ TeV}$ for the $b\bar{b}$ and $W^+W^-/\tau^+\tau^-$ annihilation channels and two time periods, winter and summer. For each dark matter mass, annihilation channel and time period, we simulated 10^6 dark matter annihilation events, obtaining the averaged neutrino flux at the IceCube detector.

The expected number of muon neutrinos observed at IceCube N_{ν_μ} is given by

$$N_{\nu_\mu} = \Gamma_a t_{\text{exp}} \int_{E_{\text{thr}}} \frac{d\phi_{\nu_\mu}}{dE} A_{\text{eff}}(E) dE, \quad (4.1)$$

where t_{exp} is the exposure time and depends on which data set is analyzed. For the winter period t_{exp} is 150 days, and for summer 167 days. A_{eff} is the IceCube's effective area. This accounts for the neutrino - nucleon interaction probability, the produced muon energy loss and also for the experimental cuts and analysis efficiencies. We take $A_{\text{eff}}(E)$ as a function of the neutrino energy for each data set as given in [106] (see figure 4.1).

$\frac{d\phi_{\nu\mu}}{dE}$ is the muon neutrino energy spectrum, obtained at the end of our simulations with WimpSim. Γ_a is the dark matter annihilation rate, given by equation (2.40), where N_χ is given by equation (2.41) for CDM, and by equation (2.44) for SIDM. It is important to note that it is in this factor that the effects of dark matter self-interactions enter for the muon neutrino events predicted at the IceCube detector.

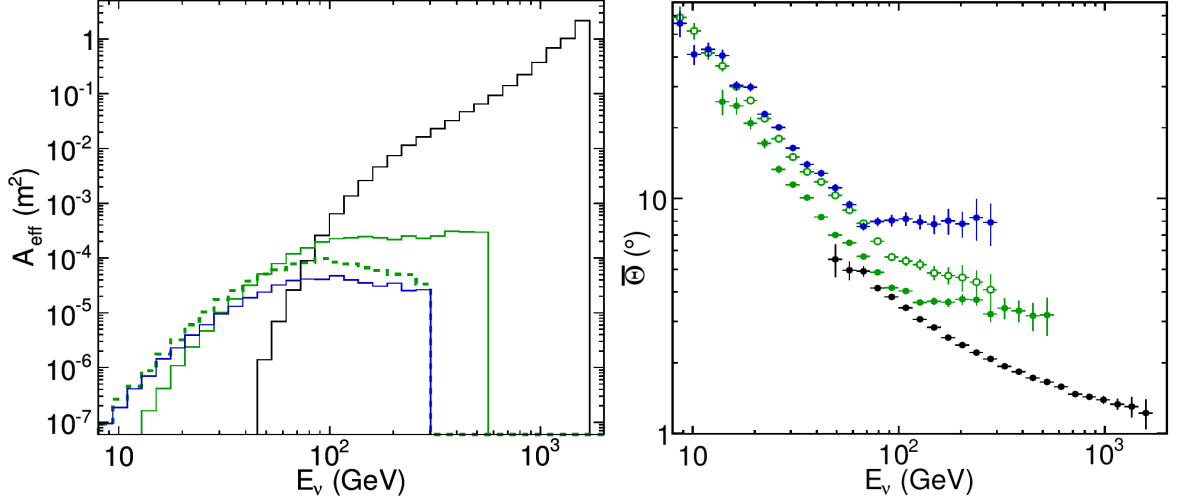


Figure 4.1: IceCube’s total neutrino effective area (left) and median angular error (right) as a function of the muon neutrino energy. The different curves correspond to the different data sets as defined in the IceCube analysis [20], being black for the winter high energy set (WH), blue for the summer set (SL) and green for the winter low energy (WL). Figure extracted from [106].

In order to compare our results to the IceCube observations we need to account for the detector’s finite angular resolution. This is shown in figure 4.1 as a function of the neutrino energy for the winter and summer data sets. The detector angular error decreases with increasing energy, going from $\sim 10^\circ$ at 40 GeV to $\sim 1^\circ$ at 1 TeV. We include this reconstruction effect by smearing the arrival direction of each simulated muon neutrino by a gaussian distribution with its σ equal to the experimental angular error at the corresponding neutrino energy. In figure 4.2 we show the neutrino arrival angular distributions about the of Sun-IceCube axis, for different dark matter mass values. We then remove all events with arriving angles $\theta > 3^\circ$, which is the IceCube’s accepted angular direction for events coming from the Sun [20]. In figure 4.3 we show the event reduction due to the angular cut for the $W^+W^-/\tau^+\tau^-$ annihilation channel, for a low (50 GeV) and a large (1 TeV) dark matter mass. As expected, the angular smearing causes a very significant loss in the neutrino flux for low energy neutrinos, while at high energies the flux after the angular cut remains almost unchanged.

After all this considerations we obtain our prediction for the integrated number of events in IceCube. In figures 4.4 we show the predicted muon neutrino events spectrum at IceCube for both annihilation channels. The spectra include the total number of

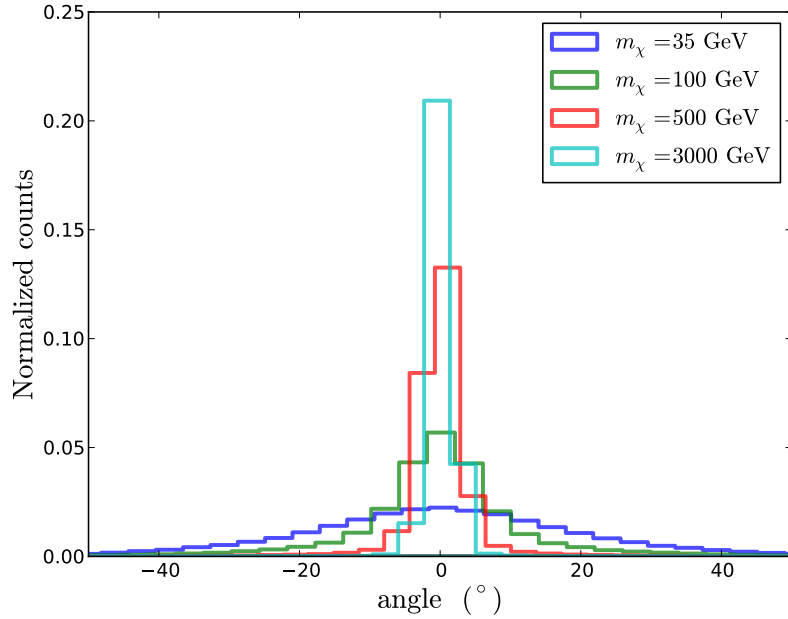


Figure 4.2: Angular smearing about the Sun-IceCube axis due to the angular direction reconstruction error of IceCube. Each histogram corresponds to a different dark matter mass value as labeled.

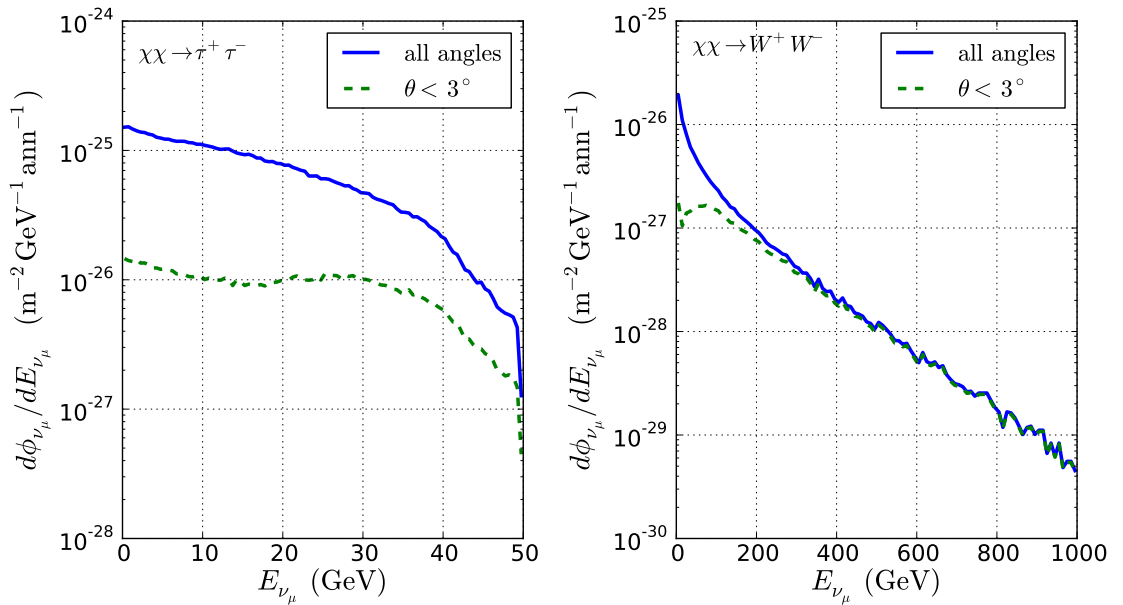


Figure 4.3: Neutrino flux as a function of the neutrino energy for $m_\chi = 50$ GeV and 1000 GeV annihilating into $W^+W^-/\tau^+\tau^-$. The blue solid line includes all simulated events and the green dashed line to events with smeared angular direction $\theta \lesssim 3^\circ$.

events (low energy and high energy) during winter for a dark matter mass of 800 GeV. The several curves correspond to different values of $\sigma_{\chi\chi}/m_\chi$ as labeled and it was taken $\sigma_{\chi n} = 10^{-44} \text{ cm}^2$. The enhancement on the expected number of events due to dark matter self-interactions is clear in these figures.

4.2 IceCube-79 Dark Matter Search Results

We compare our predictions to the results of the IceCube dark matter search [20]. The IceCube collaboration used the neutrino telescope with its 79-strings configuration to look for the muon neutrino signal originated from dark matter annihilation in the Sun. This analysis used for the first time the DeepCore subarray¹, lowering the energy threshold down to 10 GeV and extending the time of data acquisition into the summer.

In the IceCube analysis the data was divided into three sets, according the time period and energy of the events. The data during the winter season, when the Sun is below the horizon, was divided into a low energy sample (WL) and a high energy one (WH). For the summer period, when the Sun is above the horizon, only low energy events were considered (SL). The main background is constituted by down-going muons originated by cosmic rays interactions in the atmosphere. The majority of these muons are easily rejected during the winter season by looking only for up-going muon tracks in the detector. For the SL set, the IceCube digital optical modules that surround the DeepCore subarray are used as a background veto and only events with a reconstructed neutrino interaction vertex inside DeepCore were selected.

In figure 4.5 are compared the final data sets distribution of the IceCube-79 analysis (gray squares) with the expected background from atmospheric muons and neutrinos (dotted lines). The colored lines correspond to the expected signal from CDM annihilation in the Sun's center. From these results, the IceCube collaboration concludes that the observed number of events from the direction of the Sun is consistent with the background-only hypothesis. Thus, upper limits on the number of expected muons from dark matter annihilations were imposed at 90% C.L., as shown in table 4.1. These limits are for the three data sets combined.

The IceCube collaboration used these results to constraint the dark matter - nucleon interaction cross section, assuming the standard scenario for dark matter capture. It excludes values for the spin-independent $\sigma_{\chi n}$ down to $\sim 10^{-43} \text{ cm}^2$ (for $m_\chi = 500 \text{ GeV}$ and W^+W^- channel). For spin-dependent interaction obtained the most stringent results

¹The DeepCore subarray is constituted by 15 strings, each with 50 improved PMTs with 7 m vertical spacing, located in the deepest and clearest ice instrumented by IceCube, between 2100 and 2450 m below the surface [107]. It was specifically designed to lower the IceCube neutrino energy threshold by an order of magnitude, to energies $\sim 10 \text{ GeV}$. Its location at the central base of the IceCube detector, allows it to use the surrounding IceCube detector as a highly efficient active veto against the main background of downward going muons produced in cosmic-ray atmospheric showers.

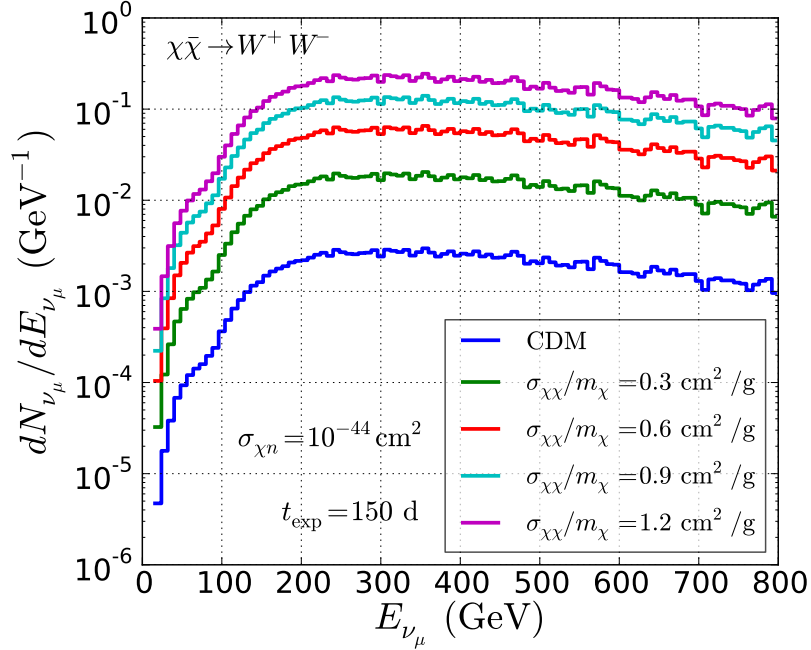
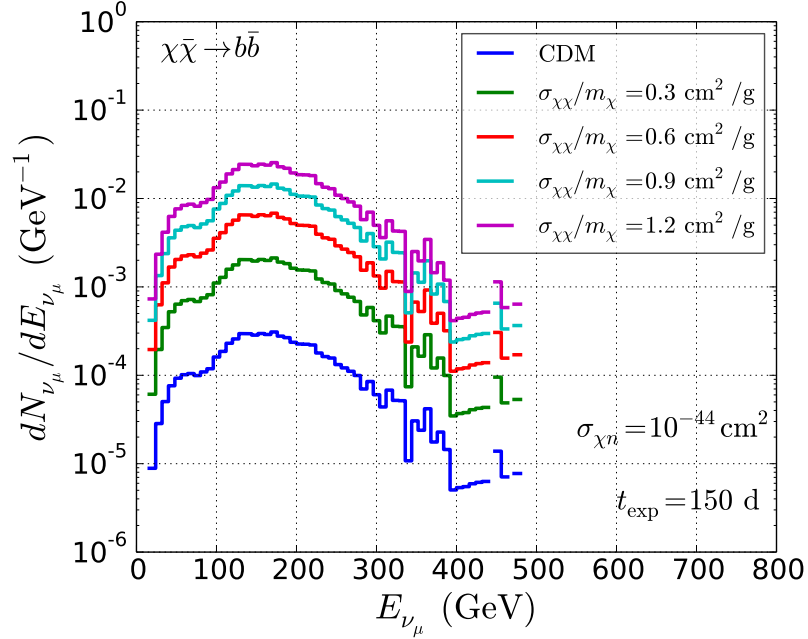


Figure 4.4: Muon neutrino events spectrum at the IceCube detector for $b\bar{b}$ (top) and W^+W^- (bottom) annihilation channels. The blue line correspond to CDM model and the others to SIDM models with different self-interaction cross sections values as labeled. For the $b\bar{b}$ annihilation channel, the integrated number of events are 0.05 for CDM and 0.36 (1.1, 2.4, 4.3) for $\sigma_{\chi\chi}/m_\chi = 0.3$ (0.6, 0.9, 1.2) cm^2/g . For the W^+W^- channel, these are 1.4 for CDM and 9.6 (30.8, 66.0, 115.2) for the SIDM models respectively. These results are for $m_\chi = 800$ GeV considering only the winter time period.

to date, excluding values of $\sigma_{\chi H}$ down to $\sim 10^{-40}$ cm² (for $m_\chi = 500$ GeV and W^+W^- channel).

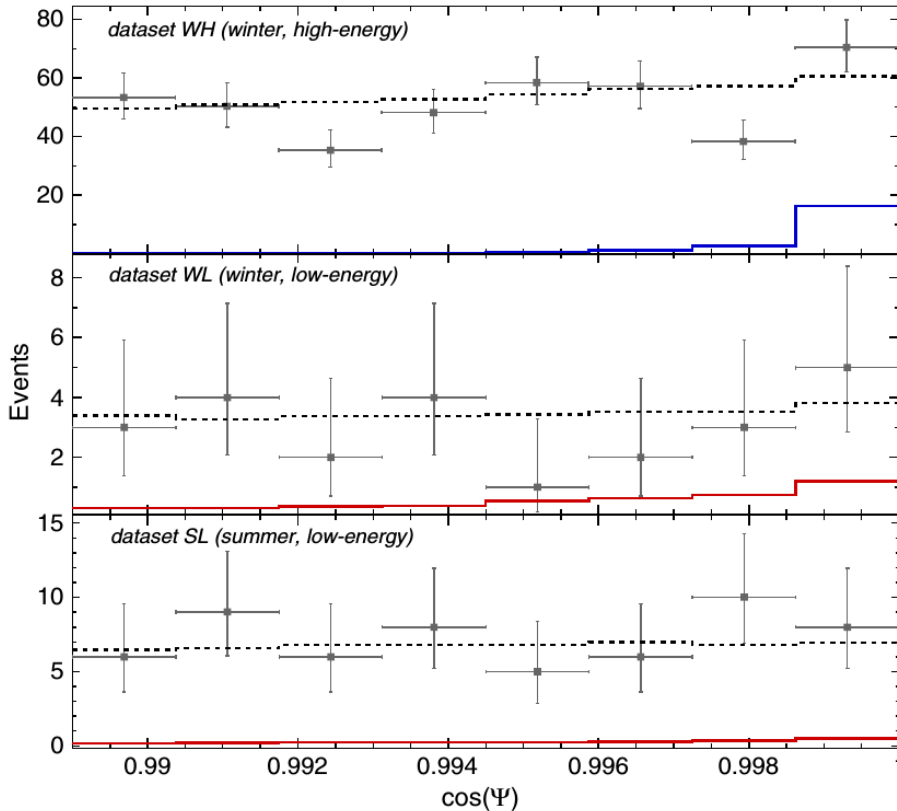


Figure 4.5: Angular distribution relative to the Sun of observed events at IceCube-79. The events are shown in gray squares for the three data sets (WL, WH and SL). The dotted curves indicate the expected background from atmospheric muons and neutrinos. Also are shown in colored lines simulated signals from dark matter annihilations in the Sun. Figure extracted from [20].

4.3 Probing velocity-independent SIDM

We use the IceCube limits on the number of expected muons to constraint SIDM models. For this, we compare our predicted number of events for the total time of IceCube data acquisition, with the IceCube-79 limits. Any model that predicts a larger number of events is ruled out at 90% C.L. We scanned the SIDM $(\sigma_{\chi\chi}, m_\chi)$ parameter space for the $W^+W^-/\tau^+\tau^-$ and $b\bar{b}$ annihilation channels assuming several fixed values for the dark matter - nucleon scattering cross section $\sigma_{\chi n}$.

We present our results for the $W^+W^-/\tau^+\tau^-$ channel in figure 4.6. The solid (dashed) blue curve are the upper limits at 90% C.L. for the $\sigma_{\chi\chi}$ as a function of m_χ , assuming a thermal annihilation cross section $\langle\sigma_{av}\rangle = 3 \times 10^{-26}$ cm³/s (10^{-27} cm³/s). Models with $\sigma_{\chi\chi}$ above these curves are excluded by our analysis. Each plot correspond to a different

Table 4.1: IceCube-79 upper limits on the number of muon events from dark matter annihilation in the Sun. Values extracted from [20]

m_χ (GeV)	μ_s^{90} ($W^+W^-/\tau^+\tau^-$ channel)	μ_s^{90} ($b\bar{b}$ channel)
20	162	-
35	70.2	128
50	19.6	55.2
100	16.8	28.9
250	29.9	19.8
500	25.2	30.6
1000	23.4	30.4
3000	22.2	26.1
5000	22.8	26.4

value of $\sigma_{\chi n}$ as labeled. In the figure are also shown other constraints on SIDM models. The black hatched region corresponds to models with $\sigma_{\chi\chi}/m_\chi > 1.25 \text{ cm}^2/\text{g}$, excluded by the Bullet Cluster analysis [24]. The region colored in yellow indicates models with $\sigma_{\chi\chi}/m_\chi > 1 \text{ cm}^2/\text{g}$, ruled out by analysis of halo density profiles [22] and halo shapes [23]. The dashed green line with arrows indicates the SIDM models with $\sigma_{\chi\chi}/m_\chi < 0.1 \text{ cm}^2/\text{g}$, which are too weak to solve the too big to fail problem of Milky Way dwarf spheroidals [26]. The dark matter models at the left side or in between the dot-dashed red lines are excluded by the direct detection experiment LUX [108], which puts upper limits on $\sigma_{\chi n}$ as a function of m_χ . As can be seen, our analysis for the $W^+W^-/\tau^+\tau^-$ channel significantly reduces the region of SIDM models that are still interesting as a solution to CDM small scale controversies.

In figure 4.7 we show our results for the $b\bar{b}$ annihilation channel. As expected, due to a smaller production of high energy neutrinos, these constraints are weaker than those for the $W^+W^-/\tau^+\tau^-$ channel. As in the case of figure 4.6, the stronger constraint in each plot corresponds to the smaller thermal annihilation cross section $\langle\sigma_a v\rangle = 10^{-27} \text{ cm}^3/\text{s}$, in agreement with equation (2.48), which favors a signal for SIDM with lower annihilation cross section. Also, from the several plots can be seen that the limits do not change significantly for different values of $\sigma_{\chi n}$. This is consistent with the fact that for strong $\sigma_{\chi\chi}$ values, the neutrino flux is independent of $\sigma_{\chi n}$, as discussed in chapter 2. Our results for the $b\bar{b}$ confirms independently most of the region excluded by the Bullet Cluster, halo density profiles and halo shapes analysis.

Additionally, we made an analysis considering dark matter capture by spin-dependent dark matter - nucleon interactions, which mainly consists of dark matter interacting with hydrogen in the Sun. Our results for the $W^+W^-/\tau^+\tau^-$ annihilation channel is presented in figure 4.8 and for the $b\bar{b}$ channel in figure 4.9. In both of these figures we choose values for $\sigma_{\chi H}$ unconstrained by the IceCube results [20]. Our constraints on SIDM models for

spin-dependent interaction are stronger than those for spin-independent. This is expected since we assume larger interaction cross sections than the ones for the spin-independent analysis. Our limits for the $W^+W^-/\tau^+\tau^-$ channel are stronger than for the $b\bar{b}$ channel as expected.

In summary, we have obtained new independent constraints on SIDM models with velocity independent self-scattering cross section using the IceCube-79 results. A significant region of the SIDM parameter space is now excluded by our analysis, excluding models with $\sigma_{\chi\chi}/m_\chi$ down to ~ 0.6 cm²/g for $\langle\sigma_a v\rangle = 3 \times 10^{-26}$ cm³/s, and down to ~ 0.1 cm²/g for $\langle\sigma_a v\rangle = 10^{-27}$ cm³/s, if dark matter annihilates into W^+W^- . The constraints are weaker for the $b\bar{b}$ annihilation channel and stronger for dark matter - nucleon spin-dependent interactions.

Combining our results with previous constraints [24, 22, 23, 26], SIDM models that could solve the CDM small scale controversies, with masses between $300 \text{ GeV} \leq m_\chi \leq 1 \text{ TeV}$, are now excluded if they annihilate into W^+W^- with a thermal annihilation cross section $\langle\sigma_a v\rangle \leq 10^{-27}$ cm³/s. In this case, solutions to the CDM potential problems will have to be encountered in different SIDM scenarios where, for example, dark matter annihilates into $b\bar{b}$. Another interesting possibility is that dark matter self-scattering cross section is velocity dependent as in [28, 109, 29, 110]. We explore this latter possibility in the next part of our work.

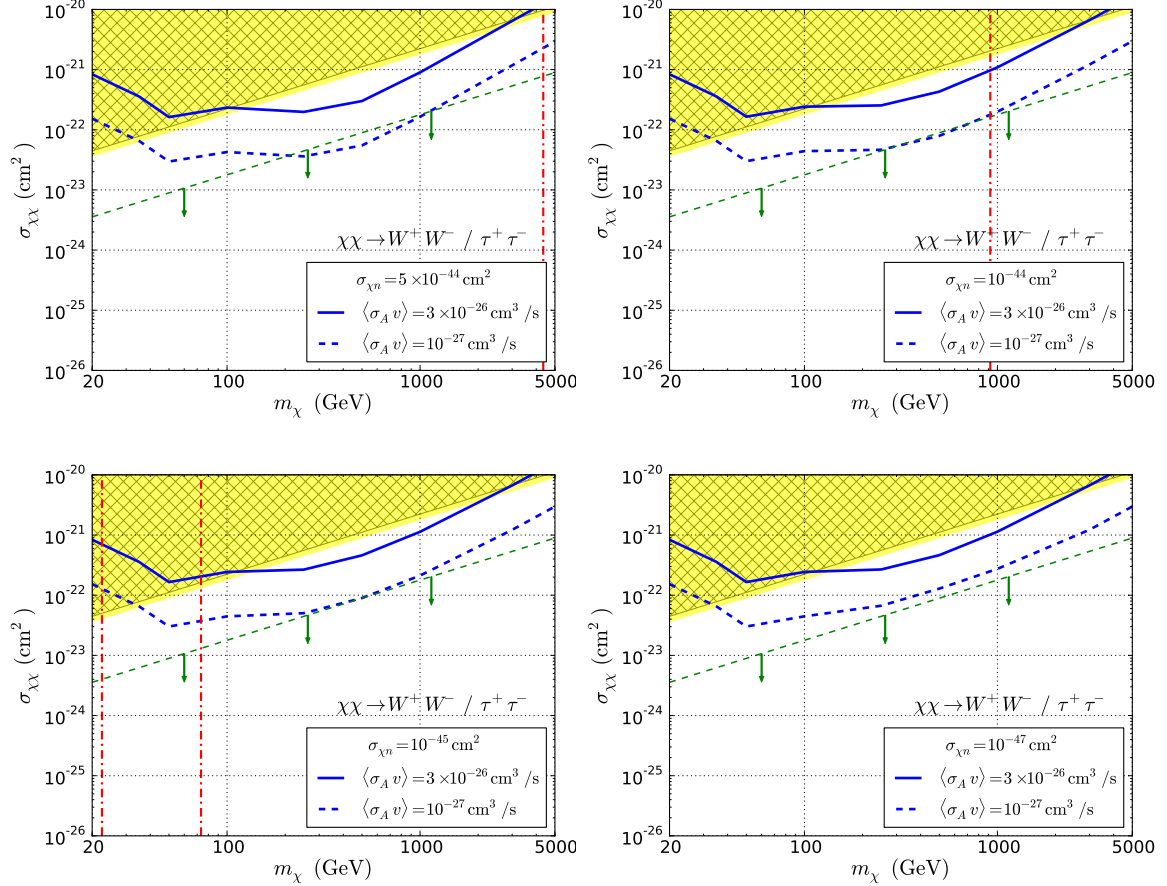


Figure 4.6: Self annihilation cross section $\sigma_{\chi\chi}$ versus dark matter mass m_χ . The regions above the blue curves exclude models with annihilation into $W^+W^-/\tau^+\tau^-$ at 90% C.L. by our analysis. The solid (dashed) line is for a thermal annihilation cross section $\langle\sigma_a v\rangle = 3(0.1) \times 10^{-26} \text{ cm}^3/\text{s}$. Each plot considers a different $\sigma_{\chi n}$ value, as labeled. Exclusion regions from a Bullet Cluster analysis [24] is shown in black hatches and by halo density profiles and halo shapes [22, 23] in yellow. The region below the dashed green line shows the region where SIDM is too weak too alleviate CDM potential problems, based on the dwarf spheroidal analysis [26]. The red lines show the direct detection limits from LUX [108], where either the region to the left or between the lines are excluded. LUX results do not probe $\sigma_{\chi n} \lesssim 10^{-47} \text{ cm}^2$, which is represented in the bottom right plot. Figure extracted from our publication [21].

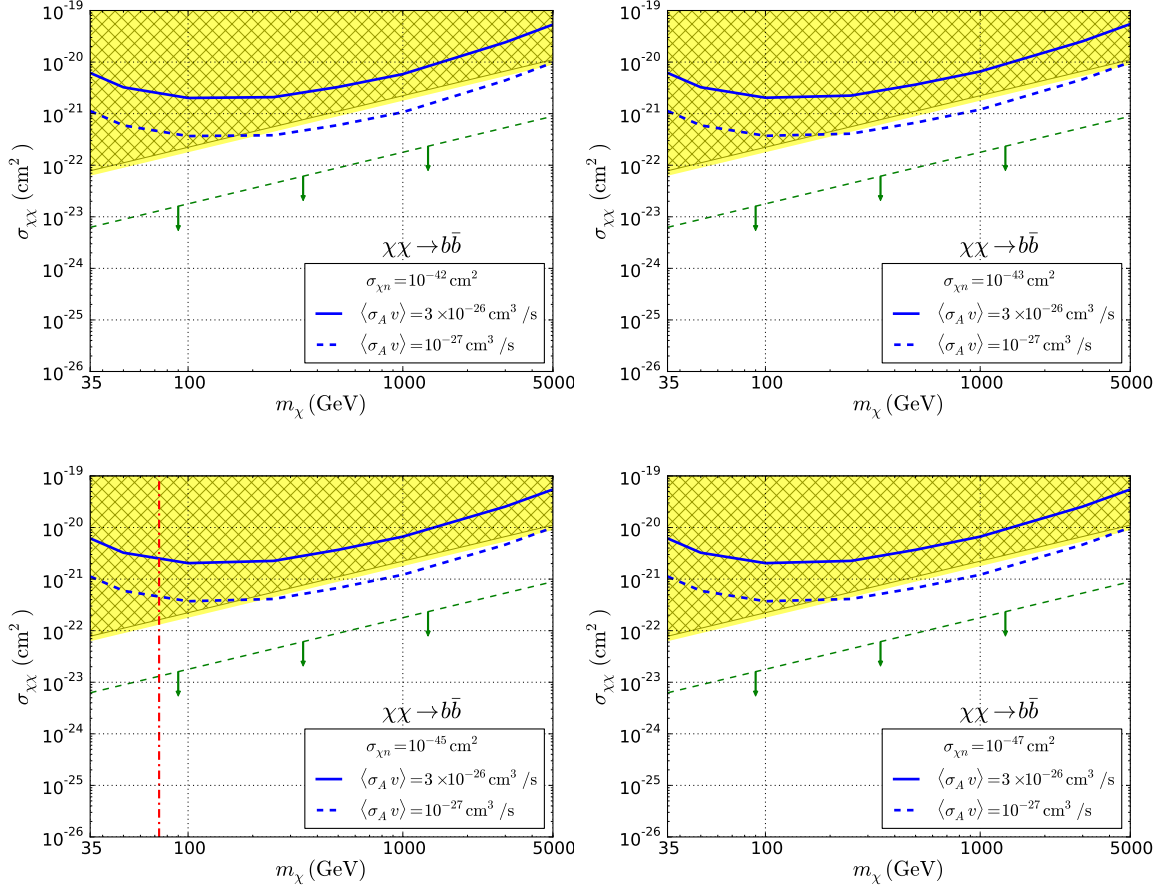


Figure 4.7: Same as previous figure but now for dark matter annihilation into $b\bar{b}$. The regions above the blue curves are excluded at 90% C.L. by our analysis. The solid (dashed) line is for a thermal annihilation cross section $\langle\sigma_A v\rangle = 3(0.1) \times 10^{-26} \text{ cm}^3/\text{s}$. Each plot considers a different $\sigma_{\chi n}$ value, as labeled. In these plots LUX [108] direct detection results exclude all the regions shown on the top figures, the region to the left of the red line in the left bottom plot, and does not probe the right bottom plot region. Figure extracted from our publication [21].

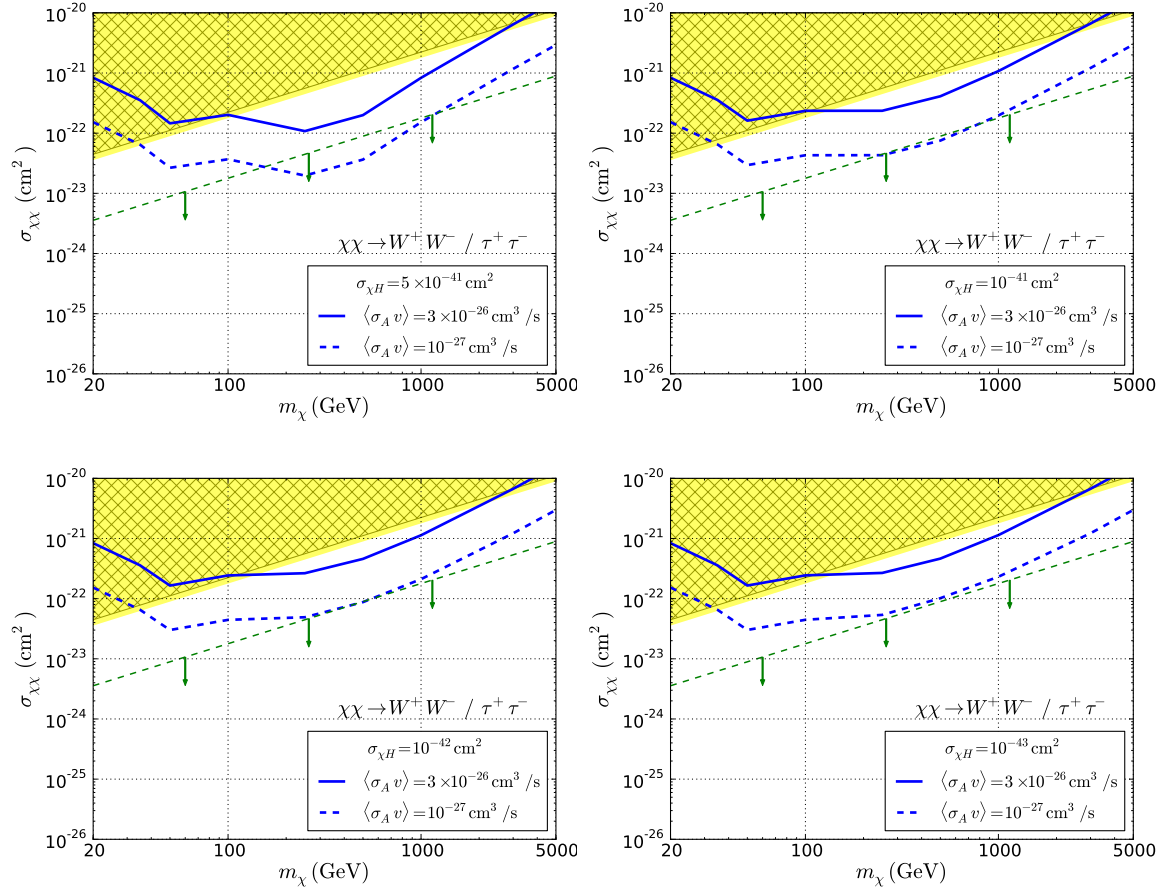


Figure 4.8: Same as Figure 4.6 but now considering $\sigma_{\chi H}$ spin-dependent interactions. There are no spin-dependent direct detection probes of the region shown in these plots.

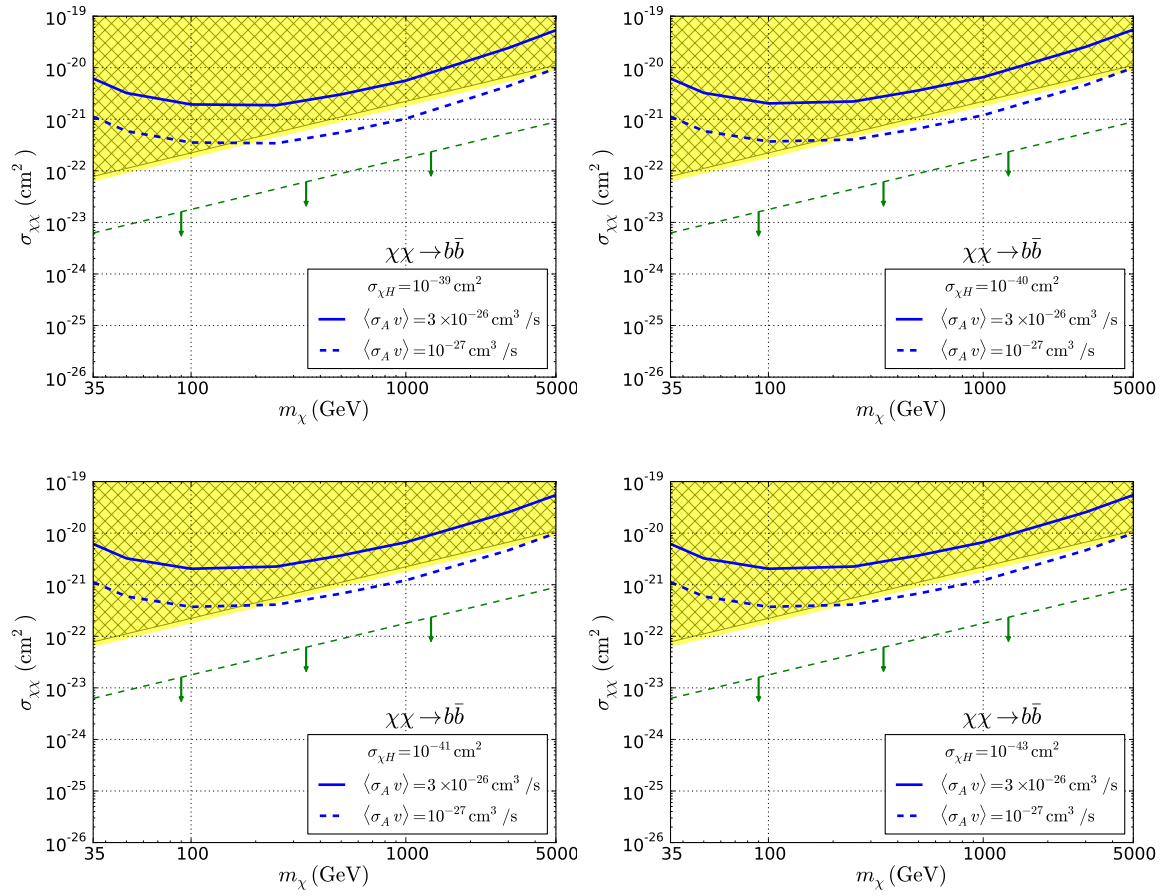


Figure 4.9: Same as Figure 4.7 but now considering $\sigma_{\chi H}$ spin-dependent interactions.

Chapter 5

Velocity Dependent SIDM

As described in chapter 1, there are several constraints on SIDM models. These were obtained from the comparison between results from SIDM simulations with observations for a wide variety of systems, such as the matter distribution of the Bullet Cluster [24, 111] and other colliding clusters [112], the density profiles of galaxies [22, 23] and the kinematics of the Milky Way's dwarf satellites [26, 84] and our own results just described in the last chapter [21]. As a result, only a small region of the parameter space of SIDM models, with a constant self-interaction cross section, are capable to solve CDM small scale controversies while being consistent with all observations.

An interesting way to evade the existent constraints is considering that the self-interacting cross section depends on the relative velocity of the dark matter particles. Such characteristic can be achieved in models where dark matter self-interacts through a Yukawa potential as in [28, 29, 109, 110]. These models can have a strong dark matter self-interaction in systems with typical low velocities, like the Milky Way's dwarf satellites, as required to solve the too big to fail problem [25, 26, 84]. At the same time, self-interactions can be highly suppressed in systems with high intrinsic velocities, evading the stringent upper limits on $\sigma_{\chi\chi}/m_\chi$ from analysis of galaxy clusters [24, 111, 112]. This proposal is supported by numerical simulations, which show that the too big to fail problem can in fact be solved within these models, while achieving agreement with the galactic density profile [25, 26].

A very interesting property of velocity dependent SIDM (vdSIDM) models is that they have Sommerfeld enhancement factors in their annihilation cross section. These can significantly increase their indirect detection signals, which can be used to probe these models.

We will focus in this chapter to obtain the corresponding muon neutrino signal from vdSIDM annihilation in the Sun to test these models by comparison with neutrino telescopes data.

5.1 A velocity dependent SIDM Model

We consider the dark matter particle χ as a Dirac fermion which couples to a vector mediator ϕ_μ of a dark $U(1)_\chi$ gauge interaction through the Lagrangian term:

$$\mathcal{L} = g_\chi \bar{\chi} \gamma^\mu \chi \phi_\mu, \quad (5.1)$$

where g_χ is the coupling constant. This interaction gives rise to dark matter self-scatterings and annihilations. We also take the dark matter as symmetric, with equal abundance of particles and anti-particles.

In the non-relativistic limit, dark matter self-interactions can be described by a Yukawa potential [27, 28, 109, 113]

$$V(r) = \pm \frac{\alpha_\chi}{r} e^{-m_\phi r}, \quad (5.2)$$

where $\alpha_\chi = g_\chi^2/(4\pi)$ is the dark fine structure constant, m_ϕ the mediator mass and r the relative distance between the dark matter particles. This potential is attractive ($-$) for $\chi\bar{\chi}$ scatterings, and repulsive ($+$), for $\chi\chi$ and $\bar{\chi}\bar{\chi}$.

The relevant quantity to investigate the dark matter self-interactions effects on structure formation is the differential self-scattering cross section $d\sigma/d\Omega$ as a function of relative velocity v . In numerical simulation analysis, the scattering angular distribution over the scattering angle θ is important, but, in order to relate the particle physics model to observations and simulation studies, it is useful to consider an integrated cross section. Therefore, we proceed as in [29] and consider the transfer cross section [114] which is widely used in SIDM literature:

$$\sigma_T = \int d\Omega (1 - \cos\theta) \frac{d\sigma}{d\Omega}. \quad (5.3)$$

This cross section can be calculated perturbatively in α_X within the Born approximation, requiring $\alpha_X m_X/m_\phi \ll 1$:

$$\sigma_T^{\text{Born}} = \frac{8\pi\alpha_X^2}{m_X^2 v^4} \left(\ln\left(1 + \frac{m_X^2 v^2}{m_\phi^2}\right) - \frac{m_X^2 v^2}{m_\phi^2 + m_X^2 v^2} \right). \quad (5.4)$$

Within the non-perturbative regime, analytical formulas can be obtained for the classical limit ($m_X v/m_\phi \gg 1$). For an attractive potential it is given by [27]:

$$\sigma_T^{\text{clas}} = \begin{cases} \frac{4\pi}{m_\phi^2} \beta^2 \ln(1 + \beta^{-1}) & \beta \lesssim 10^{-1} \\ \frac{8\pi}{m_\phi^2} \beta^2 / (1 + 1.5\beta^{1.65}) & 10^{-1} \lesssim \beta \lesssim 10^3 \\ \frac{\pi}{m_\phi^2} (\ln \beta + 1 - \frac{1}{2} \ln^{-1} \beta)^2 & \beta \gtrsim 10^3 \end{cases} \quad (5.5)$$

where $\beta \equiv 2\alpha_X m_\phi / (m_X v^2)$. However, both of these approximations cover only a limited region of the parameter space of vdSIDM models. Thus, to obtain the self-interacting cross section in the missing region we use numerical techniques.

We solve the Schrödinger equation using the partial wave method. The differential scattering cross section is given by

$$\frac{d\sigma}{d\Omega} = \frac{1}{k^2} \left| \sum_{l=0}^{\infty} (2l+1) e^{i\delta_l} P_l(\cos\theta) \sin\delta_l \right|^2, \quad (5.6)$$

where δ_l is the phase shift for the partial wave l . Using this expression in equation (5.3) and integrating over all angles, the total transfer cross sections results

$$\sigma_T = \frac{4\pi}{k^2} \sum_{l=0}^{\infty} (l+1) \sin^2(\delta_{l+1} - \delta_l). \quad (5.7)$$

Hence, to obtain the σ_T we need to calculate first the phase shift δ_l for each l in the sum.

To obtain the δ_l we solve the Schrödinger equation for the radial function $R_l(r)$ for the reduced dark matter two particle system

$$\frac{1}{r^2} \frac{d}{dr} \left(r^2 \frac{dR_l}{dr} \right) + \left(k^2 - \frac{l(l+1)}{r^2} - 2\mu V(r) \right) R_l = 0, \quad (5.8)$$

with reduced mass $\mu = m_X/2$ and $k = \mu v$. The phase shift δ_l parametrizes the asymptotic solution for $R_l(r)$, given by

$$\lim_{r \rightarrow \infty} R_l(r) \propto \cos\delta_l j_l(kr) - \sin\delta_l n_l(kr), \quad (5.9)$$

where $j_l(kr)$ and $n_l(kr)$ are the spherical Bessel and Neumann functions, respectively.

To solve equation (5.8) it is convenient to define the following variables:

$$\begin{aligned} \chi_l &\equiv r R_l, & x &\equiv \alpha_X m_X r \\ a &\equiv \frac{v}{2\alpha_X}, & b &\equiv \frac{\alpha_X m_X}{m_\phi}. \end{aligned} \quad (5.10)$$

So equation (5.8) is written as:

$$\left(\frac{d^2}{dx^2} + a^2 - \frac{l(l+1)}{x^2} - (\pm) \frac{1}{x} e^{-x/b} \right) \chi_l = 0, \quad (5.11)$$

where the $+$ ($-$) sign corresponds to a repulsive (attractive) potential.

To calculate σ_T from equation (5.7) we first obtain δ_l for fixed values of a , b and $l = 0$ then, we sum over l until reaching terms whose contribution are negligible. We proceed as in [29]:

1. We impose initial conditions for χ_l and χ'_l at a point x_i close to the origin. x_i is chosen so that $x_i \ll b, (l+1)/a$. Under this condition, equation (5.11) is dominated by the angular momentum term. Thus we expect $\chi_l(x) \propto x^{l+1}$ and therefore we can choose $\chi_l(x_i) = 1$ and $\chi'_l(x_i) = (l+1)/x_i$.
2. We solve equation (5.11) numerically within the domain $x_i \leq x \leq x_m$. x_m is determined by the condition $a^2 \gg \exp(-x_m b)/x_m$, where the potential term is suppressed compared to the kinetic term.
3. At x_m (value for x from which we expect the solution behaves like the asymptotic approximation), we match the obtained χ_l and χ'_l to the asymptotic solution, given by

$$\chi_l(x) \propto x e^{i\delta_l} (\cos \delta_l j_l(ax) - \sin \delta_l n_l(ax)). \quad (5.12)$$

Inverting this equation, it is possible to obtain the phase shift δ_l :

$$\tan \delta_l = \frac{ax_m j'_l(ax_m) - \beta_l j_l(ax_m)}{ax_m n'_l(ax_m) - \beta_l n_l(ax_m)}, \quad (5.13)$$

where

$$\beta_l = \frac{x_m \chi'_l(x_m)}{\chi_l(x_m) - 1}. \quad (5.14)$$

Our numerical algorithm makes an initial guess for the domain (x_i, x_m) according to the steps (1) and (2), and computes δ_l as described. Then it extends the domain successively, decreasing x_i and increasing x_m , to re-calculate δ_l until it converges at 1%.

4. We proceed to calculate σ_T using equation (5.7), summing over l , truncating at l_{\max} . This is determined by the condition that the last consecutive five terms contribute to less than 1% of σ_T value.

After this, we obtain σ_T as a function of the physical parameters: m_X, m_ϕ, α_X and v . In figure 5.1, we show our numerical results for σ_T/m_X as a function of m_ϕ in the case of an attractive potential. For this results we fixed $m_X = 200$ GeV, $\alpha_X = 10^{-2}$ and $v = 10$ km/s. Also, we show the Born and classical approximations for comparison. Our results reproduce those in [29].

In figure 5.2 we show our results for σ_T as a function of the relative velocity in the case of attractive (solid curves) and repulsive (dashed curves) potentials. Each curve correspond to a different set of (m_X, m_ϕ) values as labeled.

These results show that it is indeed necessary to use numerical methods to investigate dark matter self-interactions within these models, since the analytical limits for σ_T lose all the velocity spectral features which can alter significantly the actual value of σ_T .

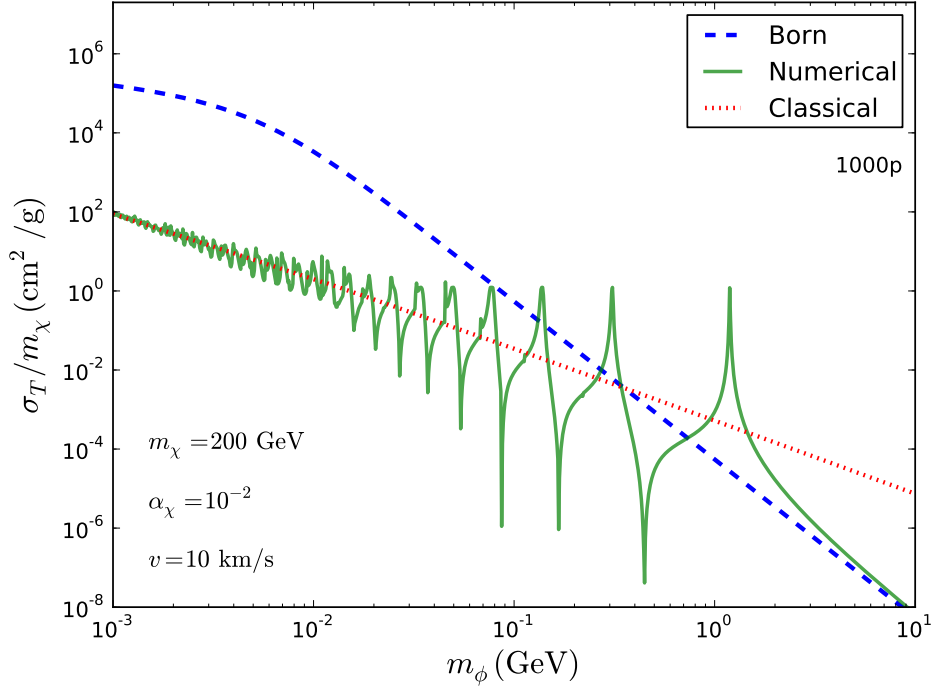


Figure 5.1: Numerical results for σ_T/m_X as a function of m_ϕ (green curve). Also are shown the results for the classical (dotted red) and Born approximations (dashed blue).

Now, we want to understand how the parameter space of vdSIDM models (m_X , m_ϕ , α_X) relate to the existent constraints on SIDM. As already mentioned, these analysis involved quite a variety of astrophysical systems such as the Bullet Cluster and Milky Way dwarf satellites, which have very different dark matter velocities distributions. For example, the Bullet Cluster have velocities close to ~ 4000 km/s, while the Milky Way dwarf spheroidal galaxies have much lower velocities around ~ 10 km/s. Therefore, the effective value of the self-interacting cross section strongly depends on the system considered. To take this into account, we computed the average of the transfer cross section $\langle\sigma_T\rangle$ over the velocities in each system:

$$\langle\sigma_T\rangle = \int \frac{d^3v_1 d^3v_2}{(\pi v_0^2)^3} e^{-\vec{v}_1^2/\vec{v}_0^2} e^{-\vec{v}_2^2/\vec{v}_0^2} \sigma_T(|\vec{v}_1 - \vec{v}_2|). \quad (5.15)$$

Changing the velocities to $\vec{v} = \vec{v}_1 - \vec{v}_2$ e $\vec{v}_t = \vec{v}_1 + \vec{v}_2$, the resulting expression is:

$$\langle\sigma_T\rangle = \int \frac{d^3v}{(2\pi v_0^2)^{3/2}} e^{-\frac{1}{2}\vec{v}^2/\vec{v}_0^2} \sigma_T(v). \quad (5.16)$$

Using this expression, it is possible to relate the limits on self-interaction cross section to the vdSIDM models. As an example we show the figure 5.3, which is extracted from [115]. In this, several curves are shown in the $m_X - m_\phi$ plane for symmetric dark matter with a

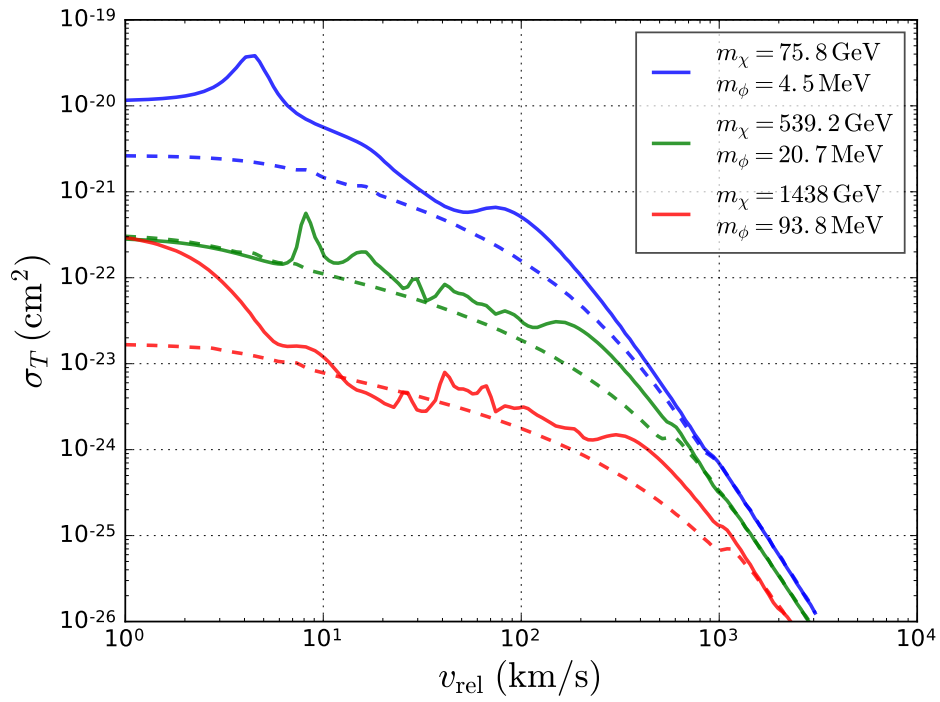


Figure 5.2: Transfer cross section as a function of relative velocity in the case of attractive (solid curves) and repulsive (dashed curves) potentials. Each curve corresponds to a different value for set of parameters, as labeled.

fixed value of $\alpha_X = 10^{-2}$. The light purple region represent the (m_X, m_ϕ) values for which $\langle\sigma_T\rangle$ falls between 0.1 and 10 cm^2/g in the case of Milky Way's dwarf galaxies (considering $v_0 = 30$ km/s in equation (5.16)). Remember that an $\langle\sigma_T\rangle$ within these values can alleviate the too big to fail problem [26]. The red curve corresponds to $\langle\sigma_T\rangle = 1$ cm^2/g at the scale of galaxy clusters (i.e. using $v_0 = 300$ km/s). This curve represent the limit obtained from halo shapes in [23], excluding models with (m_X, m_ϕ) below it. Additionally, are shown the expected sensitivity for XENON1T (purple dashed curve) and the limit from cosmic microwave background (CMB) on the parameter space if the mediator ϕ decays into pairs e^+e^- (orange line) [115, 116] (these latter results do not considered the Sommerfeld factor in dark matter annihilation).

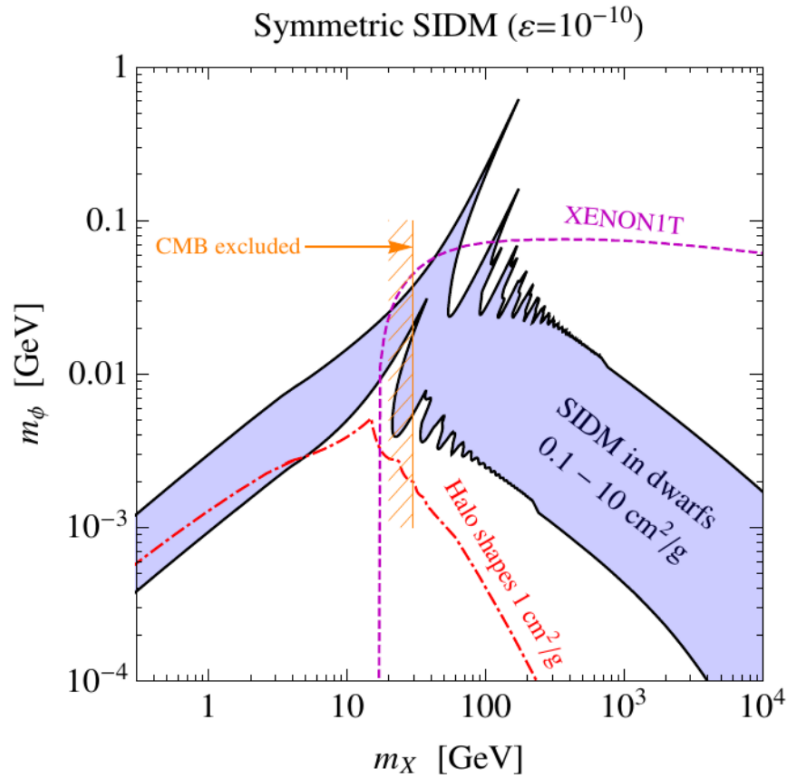


Figure 5.3: Parameter space for vdSIDM models with $\alpha_X = 10^{-2}$ for symmetric dark matter. The light purple region corresponds to (m_X, m_ϕ) values that can alleviate the too big to fail problem [26]. The curve in red represent the limit from the halo shapes analysis [23], excluding the regions below them. The purple dashed curve correspond to the XENON1T expected sensitivity and the orange vertical line to the limit from CMB assuming that the mediator ϕ decays into e^+e^- [115, 116]. The figure was extracted from [115].

Besides self-scattering, the interaction between the dark matter particles and the mediators causes also the annihilation of dark matter particles into a pair of mediators

$\chi\bar{\chi} \rightarrow \phi\phi$. The dark matter annihilation cross section at tree level is given by

$$(\sigma_a v)^{\text{tree}} = \frac{\pi\alpha_\chi^2}{m_\chi^2} \sqrt{1 - \left(\frac{m_\phi}{m_\chi}\right)^2}. \quad (5.17)$$

However, for low relative velocities, the mediator ϕ can greatly increase the annihilation cross section due to the Sommerfeld effect [117]. This is caused by the attractive self-interactions that distort the wave function of the incoming dark matter particles increasing their annihilation probability. The annihilation cross section can then be represented by

$$\sigma_a v = S(v) \times (\sigma_a v)^{\text{tree}}, \quad (5.18)$$

where the Sommerfeld factor $S(v)$ can be computed numerically in an analogous way to the one described for the self-scattering cross section [30, 118] or analytically by approximating the Yukawa potential by the Hulthen potential [31, 119, 120]. Using the latter, the Sommerfeld factor is given by

$$S = \frac{\pi}{a} \frac{\sinh(2\pi ac)}{\cosh(2\pi ac) - \cos(2\pi\sqrt{c - (ac)^2})}, \quad (5.19)$$

where $a = v/(2\alpha_\chi)$ and $c = 6\alpha_\chi m_\chi/(\pi^2 m_\phi)$.

Additionally, we considered that the dark matter annihilation process $\chi\bar{\chi} \rightarrow \phi\phi$ sets the dark matter relic density by thermal freeze-out. This requirement fixes the value of α_χ for given values of (m_χ, m_ϕ) . We include the Sommerfeld enhancement in the calculation of the DM relic density following [29, 31], which turns out important only for heavy dark matter $m_\chi \gtrsim 1$ TeV.

To compute the dark matter abundance we started with the Boltzmann equation:

$$\frac{dn_\chi}{dt} + 3Hn_\chi = -\langle\sigma_a v\rangle(n_\chi^2 - n_\chi^{\text{eq}2}), \quad (5.20)$$

where $\langle\sigma_a v\rangle$ is the thermally averaged annihilation cross section times the relative velocity, $H \equiv \dot{a}/a$ is the Hubble expansion rate, and n_χ and n_χ^{eq} are the actual and equilibrium dark matter number density. The $3Hn_\chi$ term accounts for the effect of the expansion of the universe, which dilutes the number density, and the right hand side of the equation accounts for the interactions that change the number of dark matter particles, which in this case we only considered $\chi\bar{\chi} \rightarrow \phi\phi$ and the inverse process. We assume that the mediators ϕ interact sufficiently with the SM to guarantee the thermal equilibrium with the plasma.

It is convenient to consider the time evolution in a comoving volume, scaling out the effect of the expansion of the universe. This is done by a change of variables using the entropy density, s , as a fiducial quantity: $n_\chi \rightarrow Y = n_\chi/s$ and $t \rightarrow x = m_\chi/T$. With

these variables the Boltzmann equation is rewritten as

$$\frac{dY}{dx} = -\frac{\langle\sigma_a v\rangle s}{xH}(Y^2 - Y_{\text{eq}}^2) \quad (5.21)$$

$$= -\sqrt{\frac{\pi}{45}} m_{\text{Pl}} m_\chi \frac{g_{*s}/\sqrt{g_*}}{x^2} \langle\sigma_a v\rangle (Y^2 - Y_{\text{eq}}^2), \quad (5.22)$$

where $m_{\text{Pl}} = 1.2 \times 10^{19}$ GeV is the Planck mass, and g_{*s} and g_* are the effective relativistic degrees of freedom for entropy and energy density. The solution to this equation is easy to understand qualitatively. At the early universe $x \ll 1$ the dark matter annihilation rate $\Gamma = \langle\sigma_a v\rangle n_\chi$ is greater than the expansion rate $\Gamma > H$, so the dark matter abundance Y tracks closely that of equilibrium Y_{eq} . But, as the universe cools and expands, the annihilation rate becomes equal to the expansion rate $\Gamma(x_f) \simeq H(x_f)$ for a given temperature $x \simeq x_f$ and the dark matter decouples from the plasma and its annihilations become so rare that its abundance per comoving volume remains constant, it has frozen out.

Up to the time of freeze out, due to the dark matter particles high velocity, the Sommerfeld effect is negligible so the freeze out temperature can be estimated as in the standard case for WIMPs [121, 122], resulting:

$$x_f \simeq \ln[0.038 m_{\text{Pl}} m_\chi (g/\sqrt{g_*}) \langle\sigma_a v\rangle] - \frac{1}{2} \ln(\ln[0.038 m_{\text{Pl}} m_\chi (g/\sqrt{g_*}) \langle\sigma_a v\rangle]), \quad (5.23)$$

where $g = 2$ is the number of degrees of freedom of χ and $\langle\sigma_a v\rangle$ is given by equation (5.17).

After freeze out Y_{eq} becomes insignificant quite quickly. Neglecting it, we solved the Boltzmann equation (5.22) by integration

$$Y(x_s) \approx \sqrt{\frac{45}{\pi}} \frac{1}{m_{\text{Pl}} m_\chi J}, \quad (5.24)$$

with

$$J = \int_{x_f}^{x_{\text{kd}}} \frac{g_{*s}/\sqrt{g_*}}{x^2} \langle\sigma_a v\rangle dx + \int_{x_{\text{kd}}}^{x_s} \frac{g_{*s}/\sqrt{g_*}}{x^2} \langle\sigma_a v\rangle dx, \quad (5.25)$$

where $x_{\text{kd}} = m_\chi/T_{\text{kd}}$ is the value of x at kinetic decoupling, i.e. at the temperature at which the momentum transfer via elastic scatterings between the dark matter particles and the plasma is equal to the Hubble expansion rate $\Gamma_k(T_{\text{kd}}) \simeq H(T_{\text{kd}})$ ¹, and x_s is its value when dark matter annihilations become insignificant so we can stop the integration. The integral is divided in two parts. Before kinetic decoupling the dark matter velocity distribution is thermal, sharing the same temperature as the plasma $T_\chi = T$. After kinetic decoupling, the dark matter velocity distribution initially remains thermal, but T_χ drops as a^{-2} , while T drops as a^{-1} , where a is the scale factor, and so $T_\chi = T^2/T_{\text{kd}}$.

¹It is at this temperature that the dark matter particles start to lose thermal contact with the rest of the plasma, and therefore the dark matter temperature starts to evolve separately.

The thermally averaged dark matter annihilation cross section times relative velocity in the non relativistic limit is given by

$$\langle \sigma_a v \rangle = \int \frac{d^3 v}{(2\pi v_0^2)^{3/2}} e^{-\frac{1}{2}v^2/v_0^2} \sigma_a v, \quad (5.26)$$

where $v_0 = \sqrt{2T_\chi/m_\chi} = \sqrt{2/m_\chi}$ and the annihilation cross section $(\sigma_a v)$ is given by equation (5.18), which includes the Sommerfeld factor (equation (5.19)). This can be rewritten more explicitly in terms of the variable x as:

$$\langle \sigma_a v \rangle = \frac{x_\chi^{3/2}}{2\sqrt{\pi}} \int S(\sigma_a v)^{\text{tree}} v^2 e^{-x_\chi v^2/4} dv. \quad (5.27)$$

Having obtained the present dark matter numerical density per comoving volume $Y(x_s)$, we can easily compute the dark matter mass density and its contribution to the present energy density of the universe $\Omega_\chi = \rho_\chi/\rho_{\text{cr}}$. In figure 5.4 we show our results for the calculation of the dark matter relic abundance. We consider the temperature of kinetic decoupling $T_{\text{kd}} = 1$ MeV and $m_\phi = 10$ MeV. The red solid curve corresponds to the values of α_χ as a function of the dark matter mass m_χ , such that the dark matter energy density agrees with the observed value $\Omega_\chi h^2 = 0.1184$ [35]. This curves takes into account the Sommerfeld effect. The blue dashes curves corresponds to the case disregarding the Sommeferld factor. Our results reproduce those in [29, 31].

5.2 Couplings with the Standard Model

We assume that the dark sector couples to the SM via the ϕ mediator, which allows production of known particles from dark matter annihilation in the Sun. Following a phenomenological approach, we consider that the mediator ϕ mixes with the photon γ and the Z boson through

$$\mathcal{L}_{\text{mixing}} = \frac{\varepsilon_\gamma}{2} \phi_{\mu\nu} F^{\mu\nu} + \varepsilon_Z m_Z^2 \phi_\mu Z^\mu, \quad (5.28)$$

where $\phi_{\mu\nu} \equiv \partial_\mu \phi_\nu - \partial_\nu \phi_\mu$ and $F^{\mu\nu}$ are, respectively, the mediator and the photon field strengths. The first term corresponds to the photon kinetic mixing while the second one to the mass mixing with the Z . We take the limit of very small mixing parameters $\varepsilon_\gamma, \varepsilon_Z \ll 1$. Both terms are relevant in our analysis, since the Z mixing allows the production of high energy neutrinos through ϕ decays, and the kinetic mixing the scattering off protons, which greatly contributes to the dark matter capture in the Sun. Both mixings have been widely studied within the context of vector portal dark matter, dark photon and dark Z searches [30, 123, 124, 125, 126, 127, 128, 129, 130] and also for vdSIDM direct detection in [131, 132].

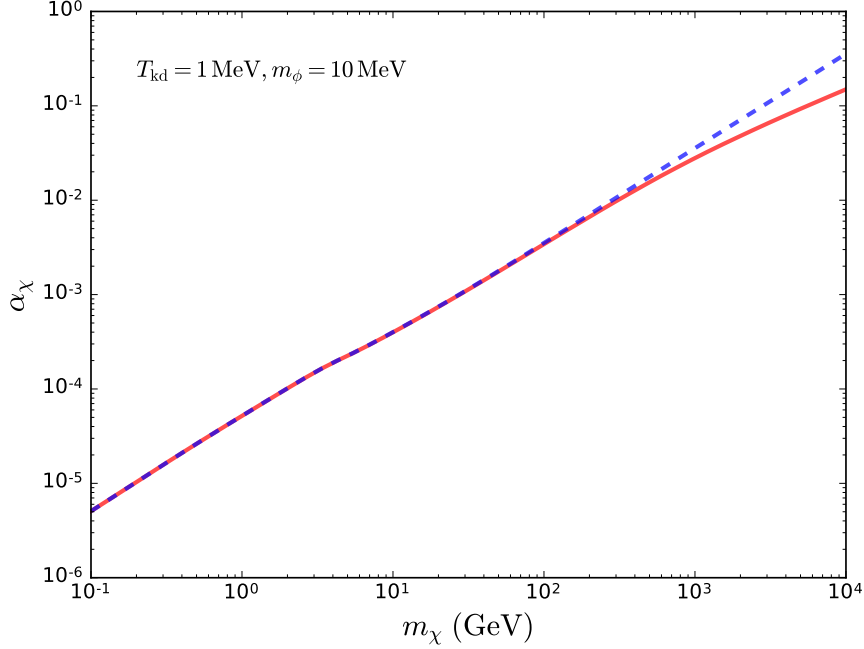


Figure 5.4: Values required for α_χ as a function of m_χ in order to obtain the observed dark matter relic abundance. The red solid curve considers the Sommerfeld enhancement factor, while the blue dashed curve does not.

If only kinetic mixing is present, for the values of m_ϕ of interest $m_\phi \sim 1 - 100$ MeV, the ϕ mediator decays predominantly into e^+e^- , with decay rate

$$\Gamma_\phi^\gamma = \frac{\alpha_{\text{em}} m_\phi \varepsilon_\gamma^2}{3}. \quad (5.29)$$

In the case of Z mixing, the total decay rate is given by

$$\Gamma_\phi^Z = \frac{\alpha_{\text{em}} m_\phi \varepsilon_Z^2 (1 - \sin^2 \theta_W + 2 \sin^4 \theta_W)}{6 \sin^2 \theta_W \cos^2 \theta_W}. \quad (5.30)$$

where the neutrino channel dominates with a branching ratio $BR_{(\phi \rightarrow \nu \bar{\nu})} \approx 6/7$, leaving a $BR_{(\phi \rightarrow e^+ e^-)} \approx 1/7$ for the e^+e^- channel. Therefore, for given values of ε_γ and ε_Z , the total decay rate is $\Gamma_\phi = \Gamma_\phi^\gamma + \Gamma_\phi^Z$ and the branching ratio to neutrinos $BR_{(\phi \rightarrow \nu \bar{\nu})} = \Gamma_{(\phi \rightarrow \nu \bar{\nu})}^Z / \Gamma_\phi$.

An additional consequence of the mediator mixing with SM particles is the DM scattering with nucleons via ϕ exchange, which are crucial for dark matter capture in the Sun. This interaction is represented by

$$\mathcal{L}_{\text{int}} = e\phi_\mu (\varepsilon_p \bar{p} \gamma^\mu p + \varepsilon_n \bar{n} \gamma^\mu n), \quad (5.31)$$

where $\varepsilon_p, \varepsilon_n$ are the effective coupling to protons and neutrons, and parametrized [131]

respectively by:

$$\varepsilon_p = \varepsilon_\gamma + \frac{\varepsilon_Z}{4 \sin \theta_W \cos \theta_W} (1 - 4 \sin^2 \theta_W) \approx \varepsilon_\gamma + 0.05 \varepsilon_Z \quad (5.32)$$

$$\varepsilon_n = -\frac{\varepsilon_Z}{4 \sin \theta_W \cos \theta_W} \approx -0.6 \varepsilon_Z. \quad (5.33)$$

Thus, in the case of kinetic mixing, the mediator couples only to protons, since only these carry electric charge. For Z mixing, the mediator couples mainly to neutrons. So, for these models isospin violation, i.e. different interactions strengths to protons and neutrons, arises naturally.

The spin-independent dark matter scattering with a nucleus N , carrying atomic number Z and mass number A , and in the zero momentum transfer limit ($q^2 = 0$) is given by

$$\sigma_{\chi N}^{\text{SI}} = \frac{16\pi\alpha_{\text{em}}\alpha_\chi\mu_{\chi N}^2}{m_\phi^4} (\varepsilon_p Z + \varepsilon_n(A - Z))^2, \quad (5.34)$$

where $\mu_{\chi N}$ is the dark matter - nucleus reduced mass. However, the mediator masses m_ϕ we are exploring are comparable to the transferred momentum in the DM scatterings with the Sun's nuclei, which are typically of the order of $q \sim 10$ MeV. Therefore, the cross section is momentum dependent and cannot be approximated by a contact interaction [131, 133]. We take this into account by considering a suppression factor

$$\sigma_{\chi N}^{\text{SI}}(q^2) = \sigma_{\chi N}^{\text{SI}}(q^2) \times \frac{m_\phi^4}{(m_\phi^2 + q^2)^2}, \quad (5.35)$$

where the momentum transfer is given by $q = \sqrt{2m_N E_R}$ and $E_R \simeq \mu_{\chi N}^2 v^2 / m_N$ is the typical nuclear recoil energy.

Before describing the dark matter accumulation in the Sun and its associated signal we briefly summarize some relevant constraints on the parameters we just described.

A lower bound on the mixing parameters $\varepsilon_\gamma, \varepsilon_Z \gtrsim 10^{-10} \times \sqrt{10 \text{ MeV}/m_\phi}$ comes from the requirement that the mediators ϕ decay fast enough, with lifetime $\tau_\phi \lesssim 1$ s, so that standard Big Bang nucleosynthesis is preserved [134]. Also, analysis of supernovae cooling through mediators emission establish strong constraints on the kinetic mixing parameter, excluding $\varepsilon_\gamma \sim 10^{-10} - 10^{-7}$ for $m_\phi \sim 1 - 100$ MeV [135, 136, 137, 138]. Recent works have revised these analysis including the plasma effects of finite temperature and density [139, 140] and specifically [140] excludes $\varepsilon_\gamma \gtrsim 10^{-8}$ for $m_\phi \sim 10 - 40$ MeV and $\varepsilon_\gamma \gtrsim 10^{-9}$ for $m_\phi \sim 10$ MeV independently of the details in their modeling.

Other constraints come from beam dump and fixed target experiments such as SLAC E137 [141, 125], the LSND neutrino experiment [142, 143] and CHARM [144, 145]. Among these, the strongest results correspond to E137, excluding $\varepsilon_\gamma \gtrsim 10^{-7}$ for mediator masses $m_\phi \lesssim 400$ MeV.

Additional constraints come from dark matter direct detection searches. Recent analysis have used the results from XENON100, LUX and SuperCDMS experiments to constraint specifically vdSIDM models [131, 132]. Their results indicate that most of the relevant parameter space with $m_\chi \gtrsim 10$ GeV if $\varepsilon_\gamma, \varepsilon_Z = 10^{-8}$ is excluded, and $m_\chi \gtrsim 30$ GeV if $\varepsilon_\gamma, \varepsilon_Z = 10^{-9}$.

Finally, there are also strong constraints from indirect detection searches. Recent analysis that included the enhancement in dark matter annihilations due to the Sommerfeld effect [146, 130] have found that the observations of gamma rays by Fermi-LAT [147], the positron and anti-proton flux by AMS-02 [148, 149, 150] and particularly the CMB by Planck [35] exclude all the parameter space of vdSIDM that can alleviate the CDM small scale problems.

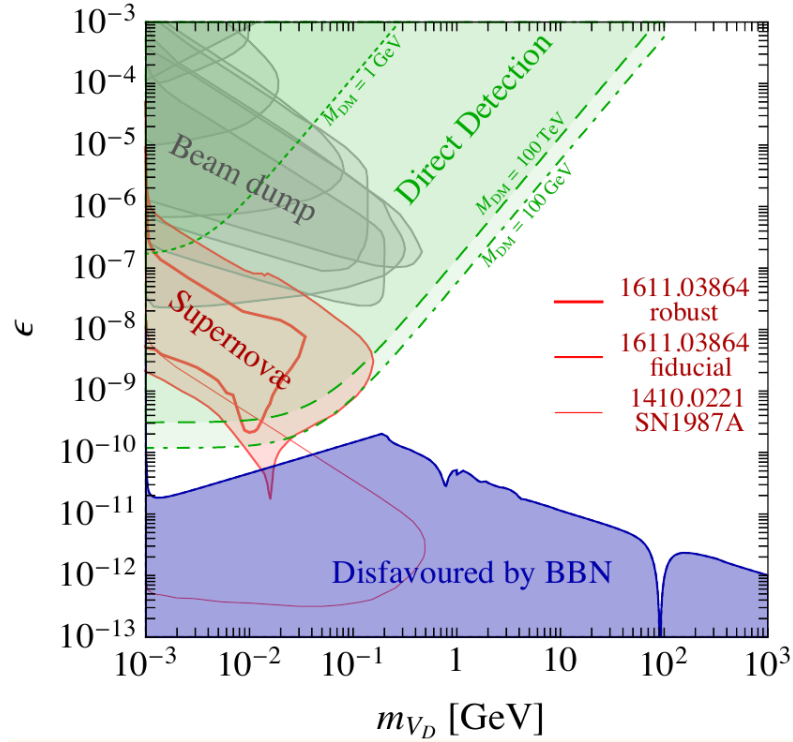


Figure 5.5: Constraints on the kinetic mixing ε_γ parameter. Excluded regions on the plane $(m_\phi, \varepsilon_\gamma)$ are shown taking into account the results from several beam dump experiments (gray areas), supernova (red), direct detection for some indicative values of m_χ (green) and from Big Bang nucleosynthesis (blue). Only the innermost supernova result (thickest red curve) is model independent [140]. Figure extracted from [130].

In our analysis we focus on vdSIDM models with mixing parameters between $\varepsilon_\gamma, \varepsilon_Z \sim 10^{-10} - 10^{-8}$ and with $m_\chi \sim 1$ GeV - TeV and $m_\phi \sim 1 - 100$ MeV.

Chapter 6

Capture and Annihilation for velocity dependent SIDM

In this chapter we analyze how dark matter with velocity dependent self-interactions affect the capture and annihilation processes in the Sun. The time evolution for the total number of dark matter particles and anti-particles in the Sun N_χ ¹ is given by

$$\dot{N}_\chi = \Gamma_c + \Gamma_s - 2\Gamma_a. \quad (6.1)$$

where Γ_a is the dark matter annihilation rate, Γ_c its capture rate due to scatterings with the Sun's nuclei, and Γ_s its self-capture rate. We neglected the evaporation of captured particles since this effect is negligible for the DM masses we are studying $m_\chi \geq 4$ GeV [91, 151].

The DM capture rate due to scatterings with the Sun's nuclei is given by equation (2.23):

$$\Gamma_c = 4.8 \times 10^{24} \text{ s}^{-1} \frac{\rho_\chi}{0.3 \text{ GeV/cm}^3} \left(\frac{270 \text{ km/s}}{\bar{v}_\chi} \right) \left(\frac{\text{GeV}}{m_\chi} \right) \sum_i \left[F_i(m_\chi) \left(\frac{\sigma_{\chi N_i}}{10^{-40} \text{ cm}^2} \right) f_i \phi_i S(m_\chi/m_{N_i}) \left(\frac{\text{GeV}}{m_{N_i}} \right) \right], \quad (6.2)$$

where the only difference relative to the SIDM with constant self-interaction lies in $\sigma_{\chi N_i}$, which now is given by equations (5.34) and (5.35). For the element distribution ϕ_i and mass fraction f_i we used updated values from [87] and [104]. We show our results for Γ_c as a function of m_χ in figure 6.1, where we considered ϕ mixing with the photon with $\varepsilon_\gamma = 10^{-10}$. Each curve corresponds to a different value of the mediator mass m_ϕ as labeled.

For the calculation of the dark matter self-capture rate Γ_s we followed [85, 152, 153]

¹From here on when we mention dark matter particles, we consider them in conjunction with their anti-particles, unless specified.

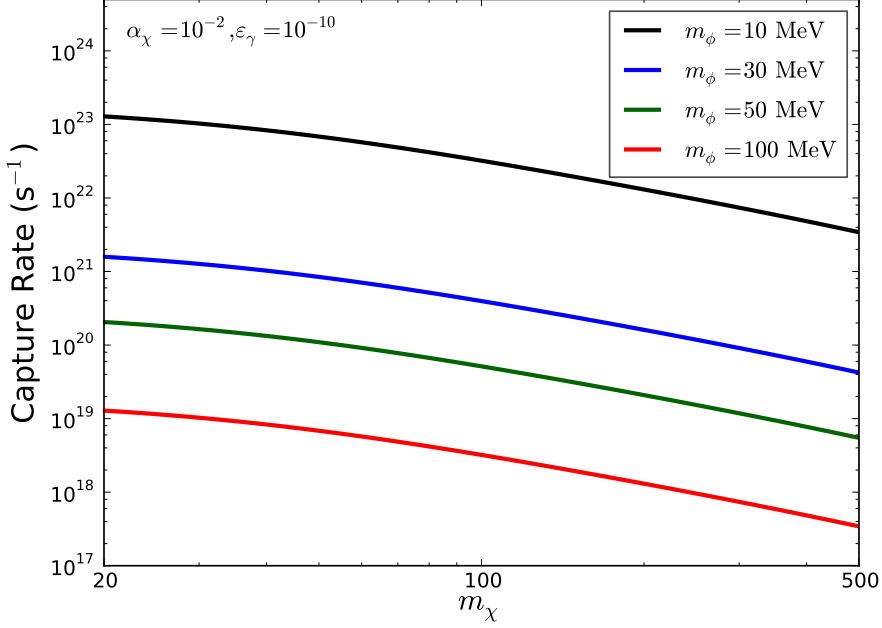


Figure 6.1: Dark matter capture rate for vdSIDM models as a function of the dark matter mass m_χ . Each curve corresponds to a different value of the mediator mass m_ϕ as labeled. It was assumed $\alpha_\chi = 10^{-2}$ and only photon mixing with $\varepsilon_\gamma = 10^{-10}$.

and [19] as detailed in chapter 2. Here we extend these procedures to account for the velocity dependence of the self-scattering cross section $\sigma_{\chi\chi}(v_{\text{rel}})$ and also the spatial and velocity distributions of the dark matter particles in the Sun. The self-capture rate can be written as $\Gamma_s = C_s N_\chi$, where N_χ is the number of captured dark matter particles and

$$C_s = \int \frac{f(u)}{u} \sigma^{\text{eff}}(v_{\text{rel}}) f(r, u') (v^2 - u'^2 - u^2) \Theta(v^2 - u'^2 - u^2) 4\pi r^2 dr d\theta du' du, \quad (6.3)$$

where

$$f(u) = \sqrt{\frac{6}{\pi}} \left(\frac{\rho_\chi}{m_\chi} \right) \frac{1}{\bar{v}} e^{-\frac{3}{2}(u/\bar{v})^2} e^{-\frac{3}{2}(\bar{v}/\tilde{v})^2} u^2 \sinh\left(\frac{3u\tilde{v}}{\bar{v}^2}\right) \frac{1}{u\tilde{v}} \quad (6.4)$$

is the dark matter velocity distribution in the halo, with the halo's velocity dispersion $\bar{v} = 270$ km/s and the Sun's velocity $\tilde{v} = 220$ km/s. We assume that the dark matter particles in the Sun have a thermal distribution [151]:

$$f(r, u') = \frac{1}{V_1} \left(\frac{m_\chi}{2\pi k T_\chi} \right)^{3/2} e^{-m_\chi u'^2 / (2k T_\chi)} e^{-m_\chi \phi(r) / (k T_\chi)} 2\pi u'^2 \sin \theta, \quad (6.5)$$

where $V_1 = \int_0^{R_\odot} e^{-m_\chi \phi / (k T_\chi)} 4\pi r^2 dr$, $\phi(r)$ is the solar gravitational potential, and T_χ is the dark matter temperature in the Sun. The effective dark matter self-scattering cross section is $\sigma^{\text{eff}}(v_{\text{rel}}) = (\sigma_{\chi\chi}^{\text{att}} + \sigma_{\chi\chi}^{\text{rep}})/2$, accounting for both attractive and repulsive interactions.

The relative speed is $v_{\text{rel}} = (v^2 + u^2 + u'^2 - 2u'\sqrt{v^2 + u^2} \cos \theta)^{1/2}$, where v is the escape velocity at a distance r from the Sun's center, and θ the angle between the velocity of the incoming particle and the one already captured in the Sun. Finally, Θ is the Heaviside step function. We integrate equation (6.3) over the particle's velocities and the Sun's volume.

Figure 6.2 shows the total dark matter capture rate $\Gamma_c + \Gamma_s(t_\odot)$ at the present epoch $t = t_\odot$ for all the studied region in (m_χ, m_ϕ) , for the mixing parameters $\varepsilon_Z = 10^{-9}$ and $\varepsilon_\gamma = 0$. The red dashed contours indicate dark matter self-capture contribution relative to the total capture rate, while the region between the orange dashed curves indicates the parameter space of vdSIDM region that alleviates the too big to fail problem with $0.1 < \langle \sigma_T \rangle / m_\chi < 10 \text{ cm}^2/\text{g}$. It is clear that for vdSIDM models the contribution of dark matter self-interactions to the total capture rate is negligible for most of the parameter space.

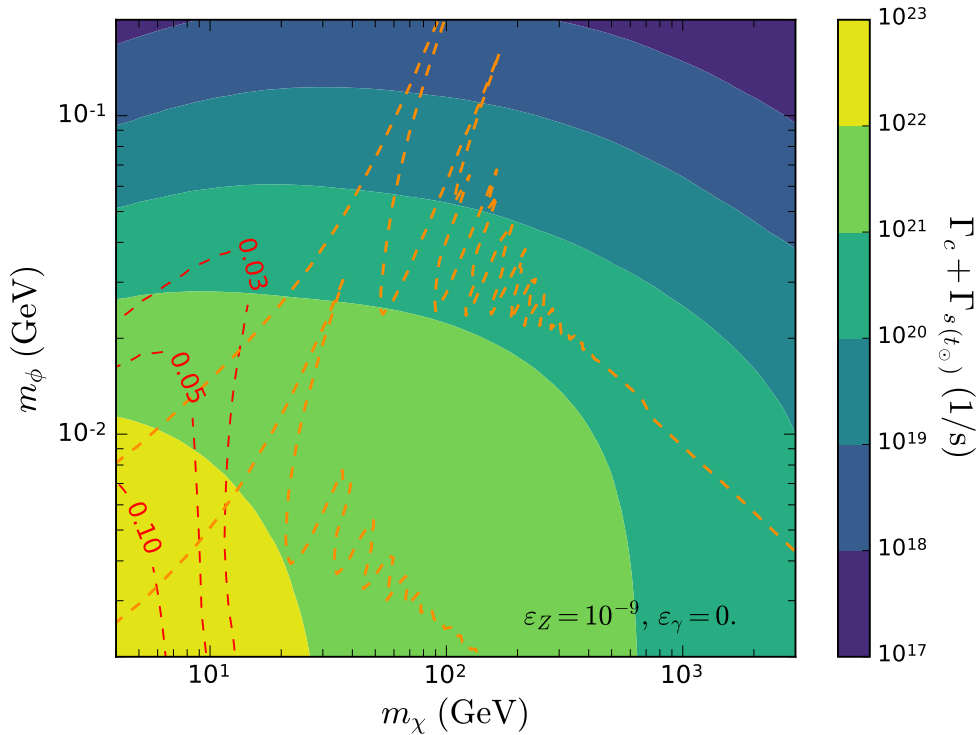


Figure 6.2: Total dark matter capture rate for $\varepsilon_Z = 10^{-9}$ and $\varepsilon_\gamma = 0$. The dashed red contours indicate the dark matter self-capture contribution relative to the total capture rate.

The annihilation rate Γ_a is given by

$$\Gamma_a = \int d^3r n_\chi(r) n_{\bar{\chi}}(r) \langle \sigma_a v \rangle, \quad (6.6)$$

where $\langle\sigma_a v\rangle$ is the thermally averaged dark matter annihilation cross section and $n_\chi(r)$ and $n_{\bar{\chi}}(r)$ are the radial distribution of dark matter particles and antiparticles in the Sun. This equation can be written as $\Gamma_a = C_a N_\chi^2/4$, where N_χ is the total number of dark matter particles and antiparticles and $C_a = \langle\sigma_a v\rangle V_2/V_1^2$, with the effective volumes $V_j = 6.9 \times 10^{27} (\frac{T_\chi}{1.57 \times 10^7 \text{K}})^{3/2} (\frac{100}{j m_\chi})^{3/2}$ [91]. The thermally averaged cross section is

$$\langle\sigma_a v\rangle = \left(\frac{m_\chi}{4\pi k T_\chi}\right)^{3/2} \int d^3v e^{-\frac{m_\chi v^2}{4k T_\chi}} (\sigma_a v), \quad (6.7)$$

where $(\sigma_a v)$ includes the Sommerfeld enhancement factor (equations (5.18) and (5.19)). The effect of this factor over C_a is clearly seen in figure 6.3, where the ratio $C_a/C_a^{w/o \text{ Sommm.}}$ of C_a including over excluding the Sommerfeld factor is shown, for all the studied (m_χ, m_ϕ) space. It can be seen that C_a is greatly enhanced, specially at large masses $m_\chi > 100$ GeV. This is expected, since the the average dark matter velocity in the Sun decreases for large m_χ .

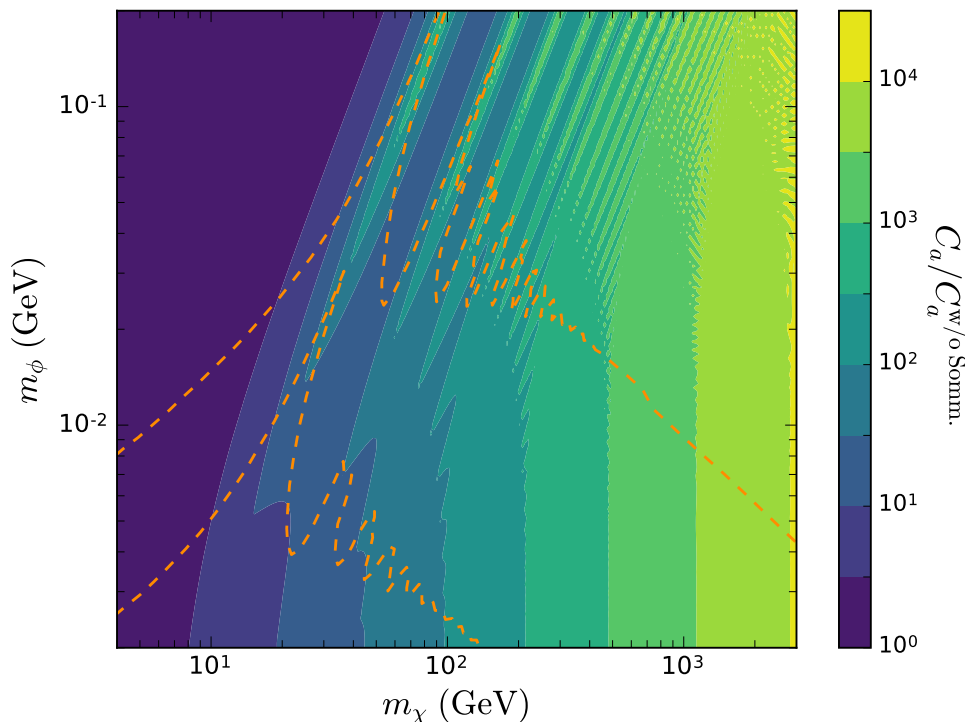


Figure 6.3: Sommerfeld enhancement effect on C_a .

In computing both Γ_s and Γ_a , we considered that the dark matter is thermally distributed in the Sun's core. For most values of m_χ the dark matter temperature is equal to the Sun's core temperature $T_\chi = 1.57 \times 10^7$ K. However for low dark matter masses ($m_\chi \lesssim 10$ GeV) a correction is needed, since in this case the particles are more dispersedly

distributed around the solar core, reaching distances where the solar temperature is lower. Hence, for these lower masses, we considered T_χ equal to the solar temperature at the dark matter mean distance from the Sun's core, e.g. $T_\chi = 1.43 \times 10^7$ K and 1.52×10^7 K for $m_\chi = 4$ and 10 GeV respectively.

Once the total capture and annihilation rates are obtained, the total number of DM particles in the Sun at a time t is given by equation (6.1), which yields to

$$N_\chi(t) = \frac{\Gamma_c \tanh(t/\zeta)}{\zeta^{-1} - C_s \tanh(t/\zeta)/2}, \quad (6.8)$$

where $\zeta = (\Gamma_c C_a/2 + C_s^2/4)^{-1/2}$ [19]. So, at present time $t_\odot = 4.57 \times 10^9$ years, and the annihilation rate is $\Gamma_a = C_a N_\chi^2(t_\odot)/4$.

In figure 6.4 we show the time evolution for the number of captured dark matter particles N_χ for three representative cases (left) and their corresponding annihilation rate Γ_a (right). The solid curves represent our results for the full calculation for vdSIDM as described above, while the dotted curves neglect the dark matter self-capture term, and the dashes curves neglect the Sommerfeld enhancement in the dark matter annihilations. The effect of self-interactions is only noticeable when the dark matter - nucleon cross section is very low, which happens for $\varepsilon_Z = 10^{-10}$ (blue curves). In this case, both the number of captured particles and the annihilation rate increase. On the other hand, the Sommerfeld enhancement in the annihilation rate hastens the equilibrium. This effect is more evident for $\varepsilon_Z = 10^{-8}$ and 10^{-9} (red and green curves). Although this lowers the total number of captured particles, the annihilation rate is much larger and reaches its maximum much earlier. However, notice that the Sommerfeld enhancement does not necessarily cause a larger annihilation rate at the present time (highlighted by the dotted vertical line), as is the case for $\varepsilon_Z = 10^{-8}$.

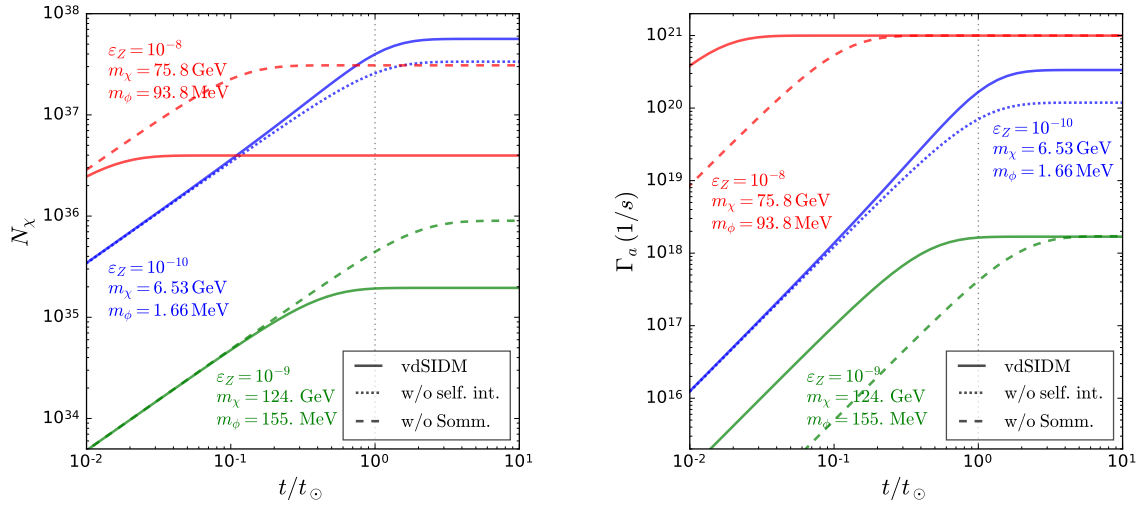


Figure 6.4: Time evolution of captured dark matter particles in the Sun for three representative cases (left) and their corresponding annihilation rates (right). Solid curves represent results for the full calculation as described in the text, dotted curves neglect the DM self-capture term, dashed curves ignore the Sommerfeld enhancement in DM annihilations.

Chapter 7

Neutrino Flux from vdSIDM Annihilation in the Sun

The annihilation of dark matter particles in the Sun creates pairs of ϕ particles which, through their subsequent decay, produce high energy electrons and neutrinos. In this work we focus on the neutrino signal, estimating its flux at the Earth and both IceCube-DeepCore [107] and PINGU's [154] sensitivity to vdSIDM models. In this way, we determine the vdSIDM parameter space to be probed by these neutrino telescopes.

The neutrinos and anti-neutrinos¹ production is flavor blind, and their energy spectrum per annihilation is given by:

$$\frac{dN_\nu}{dE_\nu} = \frac{4}{\Delta E} \Theta(E_\nu - E_-) \Theta(E_+ - E_\nu), \quad (7.1)$$

where Θ is the Heaviside function, $\Delta E = \sqrt{m_\chi^2 - m_\phi^2}$ and the maximum and minimum energies at $E_\pm = (m_\chi \pm \sqrt{m_\chi^2 - m_\phi^2})/2$, which, for the values of the masses explored $E_- \approx 0$ to $E_+ \approx m_\chi$. The specific fraction of neutrinos produced depends on the mediator's ϕ branching ratio, which depends on the mixing parameters ε_Z and ε_γ , as seen in eqs.(5.29) and (5.30). Neutrinos production is maximum when only Z mass mixing is considered, or in other words, when $\varepsilon_\gamma = 0$. Here we consider this scenario, for which $BR(\phi \rightarrow \nu\bar{\nu}) \approx 86\%$. We also consider additional cases, where $\varepsilon_\gamma = -0.64 \times \varepsilon_Z$, such that the mediator ϕ couplings to protons and neutrons are equal ($\eta \equiv \varepsilon_n/\varepsilon_p = 1$), with $BR(\phi \rightarrow \nu\bar{\nu}) \approx 74\%$, and $\eta = -0.7$ with a 68% branching ratio.

It is important to note that the neutrinos are not necessarily produced at the Sun's core, since the ϕ mediators propagate freely until their decay². Thus, the neutrinos'

¹From here on when we mention neutrinos, we consider them in conjunction with anti-neutrinos, unless specified.

²Due to the very small mixing parameters $\varepsilon_\gamma, \varepsilon_Z \sim 10^{-9}$, the ϕ mediator-nucleon cross section is also very small, being $\sigma_{\phi p} \sim 10^{-46}$ cm², which implies that their interaction length is much greater than the Sun radius.

production point depends strongly on the mixing parameters as well as on the ϕ 's Lorentz factor, given by the ratio $\gamma_\phi = m_\chi/m_\phi$. For example, for pure Z mixing, the mean decay length in the Sun's reference is given by

$$\lambda_\phi \approx 4 \times 10^{-2} R_\odot \times \left(\frac{10^{-8}}{\varepsilon_Z} \right)^2 \left(\frac{10 \text{ MeV}}{m_\phi} \right) \left(\frac{m_\chi/m_\phi}{1000} \right). \quad (7.2)$$

So, depending on the values of the model parameters, we will have scenarios where most of the neutrinos are produced inside the Sun and, conversely, where most are produced outside of it. We exemplify this in figure 7.1, where we show ϕ 's decay probability distribution for two cases: $\varepsilon_Z = 10^{-8}$, $m_\phi = 10 \text{ MeV}$, $m_\chi = 10 \text{ GeV}$ (blue) and $m_\chi = 1 \text{ TeV}$ (red). In the blue distribution most ($\sim 67\%$) of the ϕ mediators decay within the inner part of the Sun ($r \leq R_\odot/2$), while for the red distribution, due to the larger Lorentz boost, most decays ($\sim 81\%$) occur outside the Sun. We took into account this effect when computing the neutrinos' propagation.

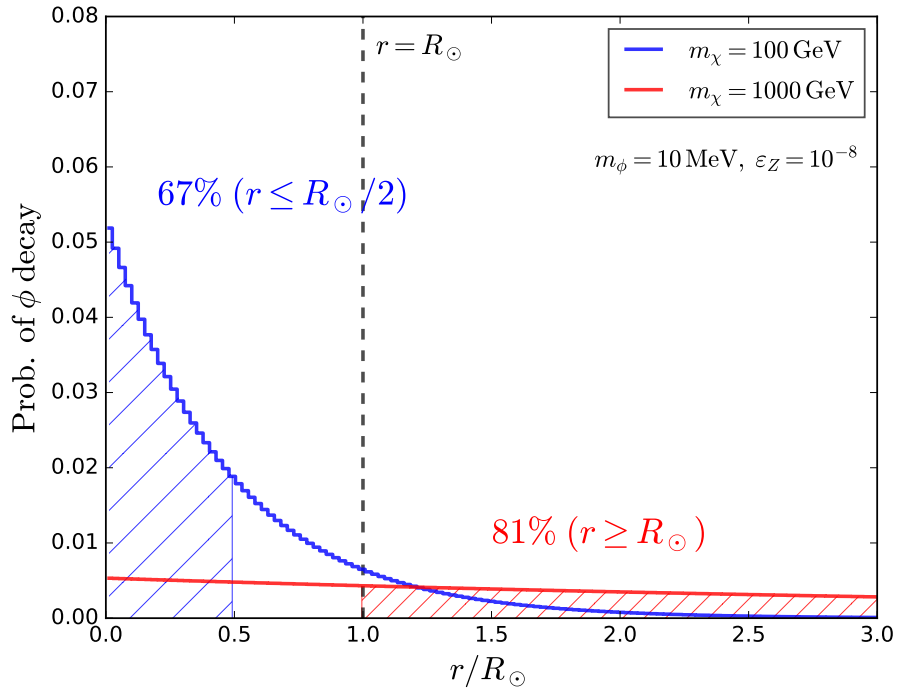


Figure 7.1: ϕ mediator decay probability as a function of the distance from the Sun's core. In the blue distribution for $m_\chi = 100 \text{ GeV}$, most decays (67%) occur inside the Sun with $r \leq R_\odot/2$, while for the red distribution corresponding to $m_\chi = 1 \text{ TeV}$, most decays (81%) occur outside the Sun.

To determine the neutrino flux at the detector, we developed a propagation code where the neutrino point of production is selected accordingly to the ϕ decay distribution. For each combination of parameters ($\varepsilon_\gamma, \varepsilon_Z, m_\chi, m_\phi$) we considered 5×10^5 annihilation events.

Neutrinos were propagated to the detector [155, 156, 96, 157] taking into account their neutral and charged interactions, oscillations and the production of secondary neutrinos. For the propagation inside the Sun, we used the density profile of the Sun as given by the standard solar model BS05OP [104]. Propagation from the Sun’s surface to a distance of 1 AU included the neutrinos produced in this region, as well as oscillations in the vacuum. Finally, they were propagated from 1 AU to the detector’s location at the Earth considering their observational time. For this latter step we used the WimpEvent program, contained in the WimpSim simulation package [96].³

Figure 7.2 shows the muon neutrino spectrum per annihilation at different stages of propagation. We represented two cases of pure Z mixing with $\varepsilon_Z = 10^{-8}$, $m_\chi = 539.2$ GeV, $m_\phi = 12.5$ MeV (red) and $m_\phi = 93.8$ MeV (green). The dotted line corresponds to the spectrum at ϕ ’s decay (given by equation (7.1) scaled by $BR(\phi \rightarrow \nu\bar{\nu})$), the dashed curves to the spectrum at the Sun’s surface and finally the solid curves at 1 AU from the Sun. Note that for the case in red, the ϕ mediator’s decay length is larger than the Sun’s radius $\lambda_\phi = 1.6 \times R_\odot$ so there is a significant contribution to the spectrum during the neutrinos propagation from $r = R_\odot$ to 1 AU. This is not the case for the spectrum in green, where λ_ϕ is very small and the vast majority of the neutrinos are produced in the Sun’s core. In this case the spectra at R_\odot and 1AU differentiate only by the effect of neutrino oscillations. Additionally, notice that the mediator late decays for the red spectrum, enable high energy neutrinos to evade absorption and energy loss in the Sun, producing a harder spectrum relative to the green curves with faster decays.

We proceeded to validate our code by comparing the obtained neutrino spectrum with that from WimpSim. The latter considers only the case of neutrinos being produced at the center of the Sun. Therefore, we took the limit in which the mediator ϕ ’s lifetime approximates to zero $\tau_\phi \rightarrow 0$ so all neutrinos in our simulation will also be produced at the center of the Sun. For the tests we considered the annihilation channel $\chi\bar{\chi} \rightarrow ZZ$ and several values for m_χ within the range of interest. In figure 7.3 we show the neutrino spectrum propagated up to the Sun’s surface obtained with both methods for dark matter with $m_\chi = 500$ GeV. Our results for ν_μ spectrum are shown in red, including the spectrum of secondary neutrinos, while the results for WimpSim correspond to the green curves. We also show the total neutrino spectrum, which includes all neutrino flavors, our results correspond to the black solid curve while the gray curve to those for the WimpSim package. Our results follows very closely those from WimpSim, sub-estimating the number of neutrinos in less than $\sim 5\%$.

The number of neutrino signal events N_ν^s in the detector is given by

$$N_\nu^s = \Gamma_a t_{\text{exp}} \times \int_{\Delta\Omega} \int_{E_{\text{th}}}^{m_\chi} \frac{d^2\phi_\nu}{dE_\nu d\Omega} A_{\text{eff}}(E_\nu) dE_\nu d\Omega \quad (7.3)$$

³For consistency we used WimpSim 3.05 default values for the neutrino oscillation parameters, as well as the neutrino - nucleon cross sections (calculated with CTEQ6-DIS PDFs [100]).

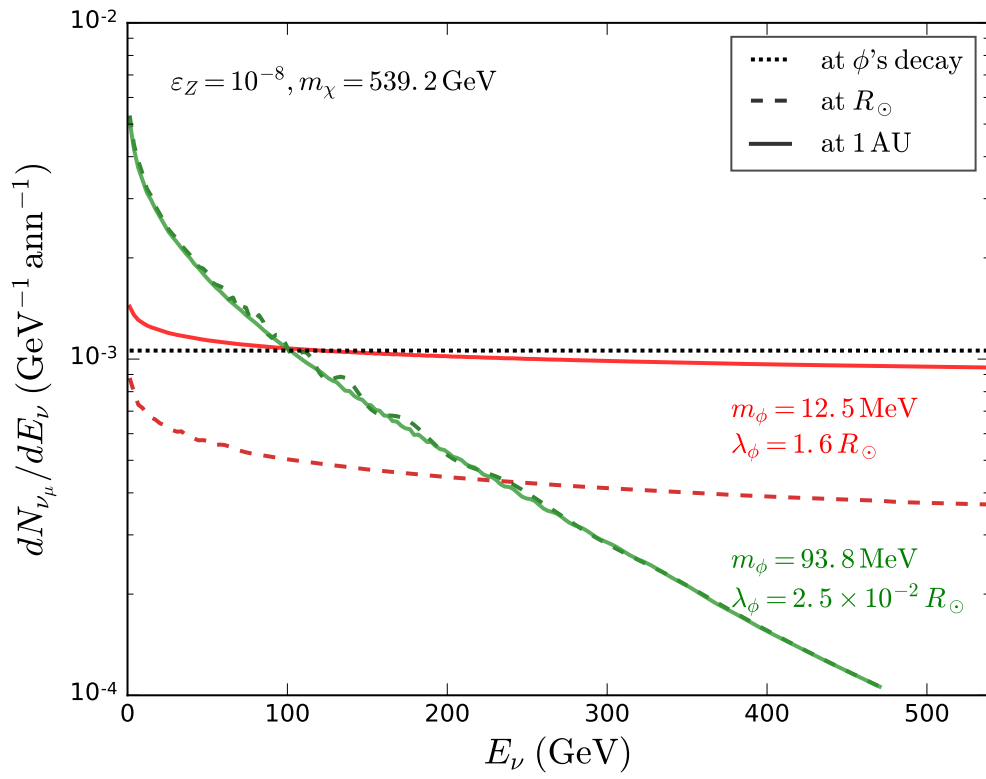


Figure 7.2: Muon neutrino spectrum at their production, $r = R_\odot$ and $r = 1 \text{ AU}$ for $m_\chi = 539.2 \text{ GeV}$ with $\varepsilon_Z = 10^{-8}$. See text for details.

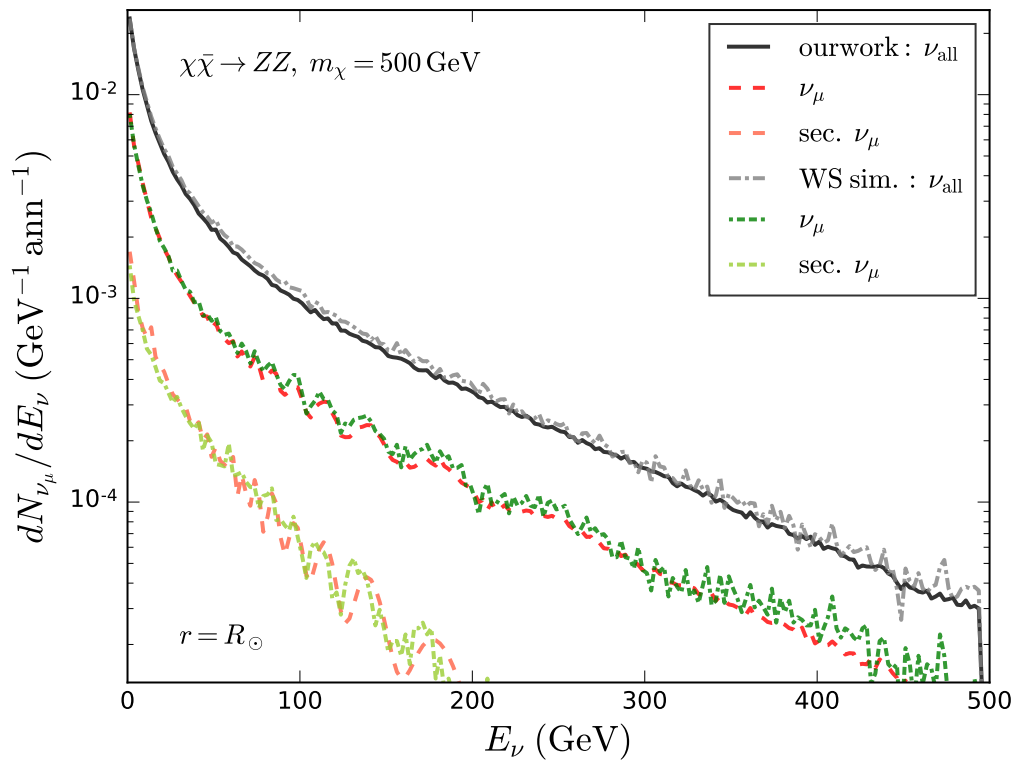


Figure 7.3: Neutrino spectrum at the Sun's radius $r = R_\odot$, for $\chi\bar{\chi} \rightarrow ZZ$ with $m_\chi = 500$ GeV. The black curve corresponds to our results for the total neutrino spectrum and the gray curve to the results using the WimpSim simulation package. Also, we show our results for the ν_μ spectrum in red, including the secondary neutrino component, and in green the corresponding ν_μ spectrum obtained with WimpSim.

where Γ_a is the dark matter annihilation rate, t_{exp} is the detector's exposure time and ϕ_ν is the neutrino flux at the detector per annihilation. We integrate over energies from the detector's energy threshold E_{th} to the maximum neutrino energy for a given dark matter mass $E_+ \approx m_\chi$. $A_{\text{eff}}(E_\nu)$ is the detector's effective area as a function of the neutrino energy E_ν [158, 159]. The latter accounts for the neutrino-nucleon interaction probability and the produced muon energy loss before detection, as well as the detector's triggers and selection analysis efficiencies.

To estimate the number of signal events we took into account the detector's angular resolution, in a similar way we described in chapter 4. The neutrino arrival direction was smeared following a gaussian distribution with its standard deviation given by the detector's angular resolution [154, 158] at the corresponding neutrino's energy. Only events arriving within a solid angle $\Delta\Omega = 2\pi(1 - \cos\Psi)$ surrounding the direction between the detector and the Sun were accepted. The acceptance angle Ψ depends on energy and specific analysis, and will be defined in the next chapter.

Muons and neutrinos produced by cosmic rays' interactions in the Earth's atmosphere constitutes the main background in our analysis. As the IceCube collaboration achieves an excellent atmospheric muon rejection [158], we consider that the background is comprised exclusively by the irreducible flux of atmospheric neutrinos.

The number of background events is given by

$$N_\nu^{\text{b}} = t_{\text{exp}} \times \int_{E_{\text{th}}}^{E_{\text{max}}} \frac{d\phi_{\nu_{\text{atm}}}}{dE_\nu} A_\nu(E_\nu) dE_\nu \times \Delta\Omega \quad (7.4)$$

where $\phi_{\nu_{\text{atm}}}$ is the atmospheric neutrino flux at the detector's location [160]. In order to compare with the dark matter signal we set $E_{\text{max}} = m_\chi$ and considered the same solid angle $\Delta\Omega = 2\pi(1 - \cos\Psi)$.

Chapter 8

IceCube-DeepCore and PINGU Sensitivities to vdSIDM

The IceCube neutrino telescope has a good sensitivity for neutrinos arriving from the Sun's direction, and thanks to its more recent inner array DeepCore, can lower its energy threshold to about ~ 10 GeV [107]. It also has a good angular resolution for muon neutrinos, ranging from $\sim 5^\circ$ at 100 GeV to $\sim 1^\circ$ at 1 TeV [158]. These features make of IceCube an ideal tool to explore vdSIDM models by looking for the muon neutrino signal from dark matter annihilations in the Sun.

In order to determine the IceCube-DeepCore sensitivity to vdSIDM, we considered the same time period as the latest IceCube collaboration's search for dark matter annihilating in the Sun [158]. It spanned a three year period including the austral winters between May 2011 and May 2014, with a total lifetime exposure of $t_{\text{exp}} = 532$ days. To be compatible with their procedure, we only considered up-going muon neutrinos. We split the results of our simulations into three samples: events with $m_\chi \leq 50$ GeV, for which dark matter annihilations result mainly in low energies neutrinos, and therefore can only be detected by DeepCore; events with $m_\chi \geq 500$ GeV, for which we considered the full IceCube's effective area, and finally events with intermediate masses where we performed a combined analysis. Accordingly, we take the acceptance angles $\Psi_1 = 10^\circ$ and $\Psi_2 = 2.8^\circ$ as reference values, where the first corresponds to DeepCore's angular cut, as defined in their analysis, and the second to the their first angular bin [158]. This latter value allows us to take advantage of the better angular resolution at higher energies.

The number of background events was determined by the average atmospheric muon neutrino flux from the Sun's direction in the winter [160]. Since during this season the Sun's zenith angle varies between 90° and 113.5° we took only the average within these directions.

Additionally, we determined the planned IceCube's extension PINGU [154] sensitivity to vdSIDM. PINGU consists of 40 new strings with 60 optical modules each in the DeepCore region of the IceCube detector, lowering the energy threshold to just a few GeV.

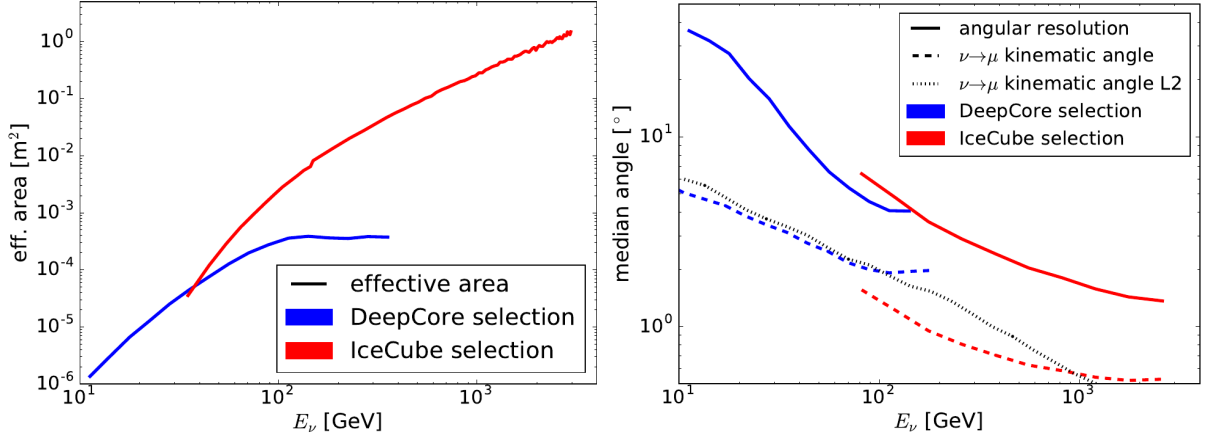


Figure 8.1: Effective area (left) and angular resolution (right) of the IceCube and DeepCore neutrino telescopes [158].

As a consequence, vdSIDM can be probed to lower masses, more specifically between 4 and 30 GeV. The same procedure as for the IceCube-DeepCore analysis was followed for the the PINGU detector, for which we used the angular resolution given in [154] and the effective area in [159].

Our results are shown in figures 8.2 and 8.3, each for different values of the mixing parameter ε_Z . The regions below or enclosed by the colored curves correspond to (m_χ, m_ϕ) values for which IceCube-DeepCore and PINGU detectors have at least a 2-sigma detection sensitivity relative to the expected background of atmospheric muon neutrinos. The solid curves are for an acceptance angle $\Psi_1 = 10^\circ$ while dashed curves are for $\Psi_2 = 2.8^\circ$. Each color correspond to different ε_γ or $\eta \equiv \varepsilon_n/\varepsilon_p$ value, as labeled. Notice that for high energy neutrinos the results for $\Psi_2 = 2.8^\circ$ cover a larger area of the parameter space as expected. The discontinuity of the curves around $m_\chi = 30$ GeV reflects the two individual analysis, one for the IceCube-DeepCore and the other for the PINGU detector. The region between the orange dashed curves correspond to the vdSIDM parameter space that alleviates the too big to fail problem, having $0.1 < \langle \sigma_T \rangle / m_\chi < 10 \text{ cm}^2/\text{g}$. For $\varepsilon_Z = 10^{-8}$, this parameter space can be almost completely probed by these experiments, while for $\varepsilon_Z = 10^{-9}$ a large part of this region can be probed for $m_\chi \gtrsim 70$ GeV. Notice that in this case, the PINGU detector's sensitivity decreases very significantly and the IceCube's sensitivity for low m_ϕ and high m_χ has a lower limit, as evidenced by the blue line at the lower right corner of figure 8.3. Finally, we also performed an analysis for $\varepsilon_Z = 10^{-10}$, but our results indicate that the neutrino telescopes lose all sensitivity.

For comparison we derive direct detection limits from the LUX experiment recent results [161]. We followed the procedure described in [131], considering the q^2 -dependent suppression factor given by equation (5.34) and taking $q \approx 50$ MeV for dark matter - xenon scattering. Additionally, we determined the limits in the case of isospin violation with $\eta = -0.7$ [162]. These limits are represented by the red dotted curves in the figures

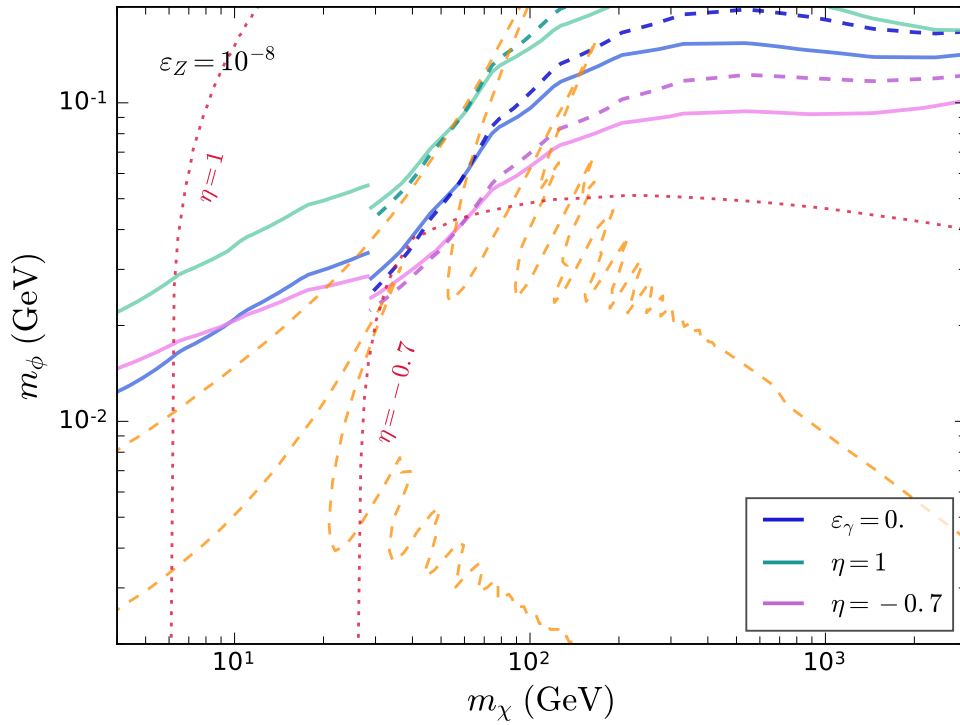


Figure 8.2: Sensitivity of IceCube-DeepCore and PINGU for vdSIDM for $\varepsilon_Z = 10^{-8}$, where the region below the curves (as labeled) can be probed by these experiments. The region between the orange dashed curves correspond to the vdSIDM parameter space that alleviates the too big to fail problem, having $0.1 < \langle \sigma_T \rangle / m_\chi < 10 \text{ cm}^2/\text{g}$. The red dotted curves correspond to limits derived from direct detection (LUX) results, see text for more details.

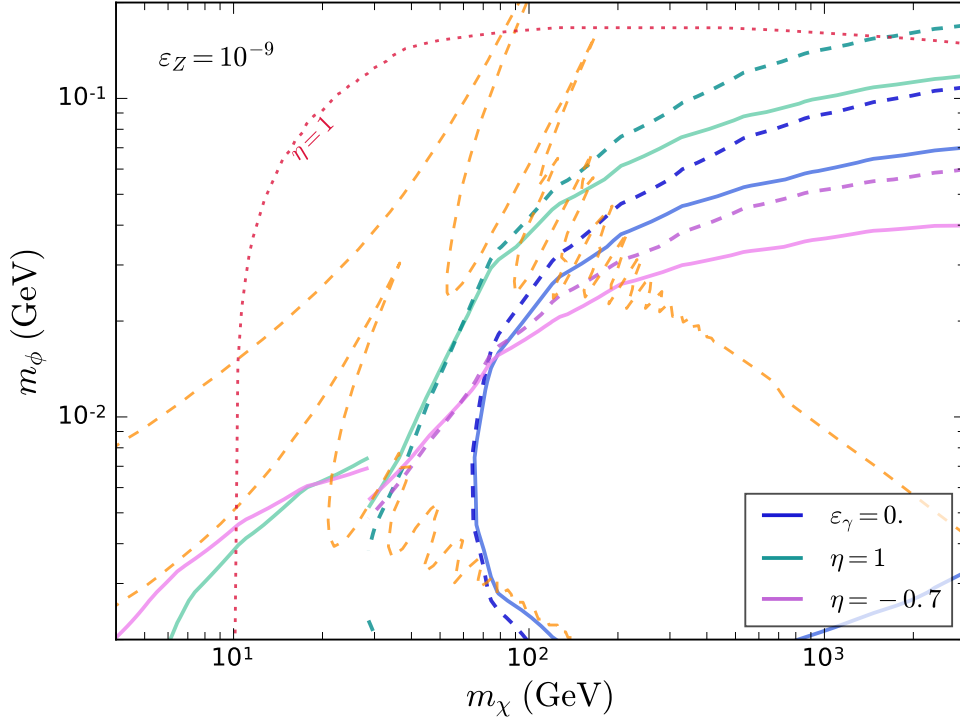


Figure 8.3: Same as figure 8.2, but for $\varepsilon_Z = 10^{-9}$.

described above, where the region below them are excluded at 90% C.L. Notice that the figure 8.3 does not include the direct detection limit for $\eta = -0.7$ since it falls out of the explored parameter space, which indicates the high dependence of direct detection results on the isospin violation parameter in contrast to that of the neutrino telescopes.

In summary, our results show that neutrino telescopes can compete with the strong results from dark matter direct detection searches. The sensitivity for $\varepsilon_Z = 10^{-8}$ is sufficient to explore the parameter space of interest almost completely. And, while the sensitivity decreases for $\varepsilon_Z = 10^{-9}$ specially at low m_χ , the neutrino telescope sensitivities do not depend on the isospin parameter η as much as the direct detection results, showing a good complementarity between both dark matter search methods.

Conclusions

In this thesis we have explored SIDM models that alleviate the small scale structure problems of collisionless CDM. We estimate how SIDM modifies the neutrino flux from dark matter annihilations in the Sun, and determine its flux at neutrino telescopes. Based on these results we show that neutrino telescopes can probe these models. We investigated two different scenarios: SIDM models with a constant self-scattering cross section and models where the self-scattering cross section depends on the relative velocity of the dark matter particles (vdSIDM).

For the first scenario, we demonstrated that most SIDM models with strong self-interacting cross sections, at $\sigma_{\chi\chi} \gtrsim \mathcal{O}(10^{-22(-23)} \text{ cm}^2)$ for an annihilation cross section $\langle\sigma_a v\rangle = 3 \times 10^{-26}(10^{-27}) \text{ cm}^3/\text{s}$ are ruled out if they annihilate into W^+W^- [21]. This exclusion comes from the comparison of our predicted neutrino signal in the IceCube detector to their observations [20]. This result is valid for both spin-dependent and spin-independent dark matter-nucleon interactions, with the first one being more stringent.

Previous studies had restricted the self-scattering per unit mass to a small range $0.1 \lesssim \sigma_{\chi\chi}/m_\chi \lesssim 1 \text{ cm}^2/\text{g}$ if these models are to alleviate the small scale problems [22, 23, 24, 25, 26]. Our results contribute further to constrain this possibility. In the case of dark matter annihilating into $W^+W^-/\tau^+\tau^-$, we exclude models with $\sigma_{\chi\chi}/m_\chi$ down to $\sim 0.6 \text{ cm}^2/\text{g}$ for $\langle\sigma_a v\rangle = 3 \times 10^{-26} \text{ cm}^3/\text{s}$, and down to $\sim 0.1 \text{ cm}^2/\text{g}$ for $\langle\sigma_a v\rangle = 10^{-27} \text{ cm}^3/\text{s}$. Thus, in order to evade these constraints, SIDM would have to annihilate to other channels that produce a softer neutrino spectrum, such as $b\bar{b}$. Another interesting possibility is to consider that the self-interacting cross section is velocity dependent.

We analyzed this latter scenario considering a simple vdSIDM model in which the dark force is mediated by a dark vector boson ϕ that couples to the photon and Z boson with mixing parameters ε_γ and ε_Z . We determined the neutrino telescopes sensitivity to these models assuming plausible values for its parameters [33].

In this scenario, in order to determine the neutrino indirect signal, several effects need to be accounted including Sommerfeld enhanced dark matter annihilation as well as the enhancement on the produced neutrino flux due to mediator ϕ late decays. We showed that, in contrast with SIDM models with constant self-scattering cross section, where the self-capture cause a significant enhancement on the neutrino signal, the self-interactions for vdSIDM models have a very modest effect. This is due to the high velocity at which

the dark matter particles from the halo reach when traversing the Sun.

We conclude that, for $\varepsilon_Z = 10^{-8}$ the detector's sensitivity is enough to probe the vast majority of the relevant vdSIDM parameter space for all ε_γ analyzed values, including the low dark matter mass region, thanks to the PINGU detector. These results show that neutrino telescopes can compete and complement the strong results from dark matter direct detection searches.

Although the sensitivity decreases for $\varepsilon_Z = 10^{-9}$ it is still enough to probe most of the parameter space for $m_\chi \gtrsim 70$ GeV. In this case the PINGU detector has almost no sensitivity for vdSIDM models. Additionally, the neutrino telescopes lose all sensitivity for $\varepsilon_Z \leq 10^{-10}$.

We have shown that the IceCube-DeepCore neutrino telescope with its current accumulated data is sensitive to most of the parameter space of vdSIDM models that alleviate the small scale structure problems observed in dwarf galaxies. Experimental analysis could probe these models, and independently confirm direct detection limits. It can also expand these limits, specially in the case of isospin violation, where we have shown that IceCube-DeepCore sensitivity is drastically better than direct detection.

Bibliography

- [1] D. H. Weinberg, J. S. Bullock, F. Governato, R. K. de Naray and A. H. G. Peter, *Cold dark matter: controversies on small scales*, 1306.0913.
- [2] A. Del Popolo and M. Le Delliou, *Small scale problems of the Λ CDM model: a short review*, *Galaxies* **5** (2017) 17, [1606.07790].
- [3] W. de Blok, *The Core-Cusp Problem*, *Adv.Astron.* **2010** (2010) 789293, [0910.3538].
- [4] S.-H. Oh, W. J. G. de Blok, E. Brinks, F. Walter and R. C. Kennicutt, Jr, *Dark and luminous matter in THINGS dwarf galaxies*, *Astron. J.* **141** (2011) 193, [1011.0899].
- [5] R. Kuzio de Naray, S. S. McGaugh and W. de Blok, *Mass Models for Low Surface Brightness Galaxies with High Resolution Optical Velocity Fields*, *Astrophys.J.* **676** (2008) 920–943, [0712.0860].
- [6] J. F. Navarro, C. S. Frenk and S. D. M. White, *A Universal density profile from hierarchical clustering*, *Astrophys. J.* **490** (1997) 493–508, [astro-ph/9611107].
- [7] J. F. Navarro, A. Ludlow, V. Springel, J. Wang, M. Vogelsberger, S. D. White et al., *The Diversity and Similarity of Simulated Cold Dark Matter Halos*, astro-ph/08101522.
- [8] J. Stadel, D. Potter, B. Moore, J. Diemand, P. Madau et al., *Quantifying the heart of darkness with GHALO - a multi-billion particle simulation of our galactic halo*, *Mon.Not.Roy.Astron.Soc.* **398** (2009) L21–L25, [0808.2981].
- [9] M. Boylan-Kolchin, J. S. Bullock and M. Kaplinghat, *Too big to fail? The puzzling darkness of massive Milky Way subhaloes*, *Mon.Not.Roy.Astron.Soc.* **415** (2011) L40, [1103.0007].
- [10] M. Boylan-Kolchin, J. S. Bullock and M. Kaplinghat, *The Milky Way’s bright satellites as an apparent failure of LCDM*, *Mon.Not.Roy.Astron.Soc.* **422** (2012) 1203–1218, [1111.2048].
- [11] F. Governato, A. Zolotov, A. Pontzen, C. Christensen, S. Oh et al., *Cuspy No More: How Outflows Affect the Central Dark Matter and Baryon Distribution in Lambda CDM Galaxies*, *Mon.Not.Roy.Astron.Soc.* **422** (2012) 1231–1240, [1202.0554].
- [12] A. M. Brooks and A. Zolotov, *Why Baryons Matter: The Kinematics of Dwarf Spheroidal Satellites*, *Astrophys.J.* **786** (2014) 87, [1207.2468].

- [13] V. Avila-Reese, P. Colin, O. Valenzuela, E. D’Onghia and C. Firmani, *Formation and structure of halos in a warm dark matter cosmology*, *Astrophys.J.* **559** (2001) 516–530, [astro-ph/0010525].
- [14] M. R. Lovell, V. Eke, C. S. Frenk, L. Gao, A. Jenkins et al., *The Haloes of Bright Satellite Galaxies in a Warm Dark Matter Universe*, *Mon.Not.Roy.Astron.Soc.* **420** (2012) 2318–2324, [1104.2929].
- [15] D. N. Spergel and P. J. Steinhardt, *Observational evidence for selfinteracting cold dark matter*, *Phys.Rev.Lett.* **84** (2000) 3760–3763, [astro-ph/9909386].
- [16] A. Burkert, *The Structure and evolution of weakly selfinteracting cold dark matter halos*, *Astrophys.J.* **534** (2000) L143–L146, [astro-ph/0002409].
- [17] B. Moore, S. Gelato, A. Jenkins, F. Pearce and V. Quilis, *Collisional versus collisionless dark matter*, *Astrophys.J.* **535** (2000) L21–L24, [astro-ph/0002308].
- [18] R. Dave, D. N. Spergel, P. J. Steinhardt and B. D. Wandelt, *Halo properties in cosmological simulations of selfinteracting cold dark matter*, *Astrophys.J.* **547** (2001) 574–589, [astro-ph/0006218].
- [19] A. R. Zentner, *High-Energy Neutrinos From Dark Matter Particle Self-Capture Within the Sun*, *Phys.Rev.* **D80** (2009) 063501, [0907.3448].
- [20] ICECUBE COLLABORATION collaboration, M. Aartsen et al., *Search for dark matter annihilations in the Sun with the 79-string IceCube detector*, *Phys.Rev.Lett.* **110** (2013) 131302, [1212.4097].
- [21] I. F. M. Albuquerque, C. Pérez de Los Heros and D. S. Robertson, *Constraints on self interacting dark matter from IceCube results*, *JCAP* **1402** (2014) 047, [1312.0797].
- [22] M. Rocha, A. H. Peter, J. S. Bullock, M. Kaplinghat, S. Garrison-Kimmel et al., *Cosmological Simulations with Self-Interacting Dark Matter I: Constant Density Cores and Substructure*, *Mon.Not.Roy.Astron.Soc.* **430** (2013) 81–104, [1208.3025].
- [23] A. H. Peter, M. Rocha, J. S. Bullock and M. Kaplinghat, *Cosmological Simulations with Self-Interacting Dark Matter II: Halo Shapes vs. Observations*, 1208.3026.
- [24] S. W. Randall, M. Markevitch, D. Clowe, A. H. Gonzalez and M. Bradac, *Constraints on the Self-Interaction Cross-Section of Dark Matter from Numerical Simulations of the Merging Galaxy Cluster 1E 0657-56*, *Astrophys.J.* **679** (2008) 1173–1180, [0704.0261].
- [25] M. Vogelsberger, J. Zavala and A. Loeb, *Subhaloes in Self-Interacting Galactic Dark Matter Haloes*, *Mon.Not.Roy.Astron.Soc.* **423** (2012) 3740, [1201.5892].
- [26] J. Zavala, M. Vogelsberger and M. G. Walker, *Constraining Self-Interacting Dark Matter with the Milky Way’s dwarf spheroidals*, *Monthly Notices of the Royal Astronomical Society: Letters* **431** (2013) L20–L24, [1211.6426].

- [27] J. L. Feng, M. Kaplinghat and H.-B. Yu, *Halo Shape and Relic Density Exclusions of Sommerfeld-Enhanced Dark Matter Explanations of Cosmic Ray Excesses*, *Phys.Rev.Lett.* **104** (2010) 151301, [0911.0422].
- [28] A. Loeb and N. Weiner, *Cores in Dwarf Galaxies from Dark Matter with a Yukawa Potential*, *Phys.Rev.Lett.* **106** (2011) 171302, [1011.6374].
- [29] S. Tulin, H.-B. Yu and K. M. Zurek, *Beyond Collisionless Dark Matter: Particle Physics Dynamics for Dark Matter Halo Structure*, *Phys.Rev.* **D87** (2013) 115007, [1302.3898].
- [30] N. Arkani-Hamed, D. P. Finkbeiner, T. R. Slatyer and N. Weiner, *A Theory of Dark Matter*, *Phys. Rev.* **D79** (2009) 015014, [0810.0713].
- [31] J. L. Feng, M. Kaplinghat and H.-B. Yu, *Sommerfeld Enhancements for Thermal Relic Dark Matter*, *Phys. Rev.* **D82** (2010) 083525, [1005.4678].
- [32] R. K. Leane, K. C. Y. Ng and J. F. Beacom, *Powerful Solar Signatures of Long-Lived Dark Mediators*, *Phys. Rev.* **D95** (2017) 123016, [1703.04629].
- [33] D. S. Robertson and I. F. M. Albuquerque, *Probing Velocity Dependent Self-Interacting Dark Matter with Neutrino Telescopes*, 1711.02052.
- [34] A. Berlin, D. S. Robertson, M. P. Solon and K. M. Zurek, *Bino variations: Effective field theory methods for dark matter direct detection*, *Phys. Rev.* **D93** (2016) 095008, [1511.05964].
- [35] PLANCK collaboration, P. A. R. Ade et al., *Planck 2015 results. XIII. Cosmological parameters*, *Astron. Astrophys.* **594** (2016) A13, [1502.01589].
- [36] 2dFGRS collaboration, S. Cole et al., *The 2dF Galaxy Redshift Survey: Power-spectrum analysis of the final dataset and cosmological implications*, *Mon. Not. Roy. Astron. Soc.* **362** (2005) 505–534, [astro-ph/0501174].
- [37] BOSS collaboration, R. A. C. Croft et al., *Large-scale clustering of Lyman α emission intensity from SDSS/BOSS*, *Mon. Not. Roy. Astron. Soc.* **457** (2016) 3541–3572, [1504.04088].
- [38] BOSS collaboration, F. Beutler et al., *The clustering of galaxies in the completed SDSS-III Baryon Oscillation Spectroscopic Survey: baryon acoustic oscillations in the Fourier space*, *Mon. Not. Roy. Astron. Soc.* **464** (2017) 3409–3430, [1607.03149].
- [39] J. Dubinski and R. Carlberg, *The Structure of cold dark matter halos*, *Astrophys.J.* **378** (1991) 496.
- [40] B. Moore, T. R. Quinn, F. Governato, J. Stadel and G. Lake, *Cold collapse and the core catastrophe*, *Mon.Not.Roy.Astron.Soc.* **310** (1999) 1147–1152, [astro-ph/9903164].
- [41] B. Moore, *Evidence against dissipationless dark matter from observations of galaxy haloes*, *Nature* **370** (1994) 629.

- [42] W. de Blok and A. Bosma, *High-resolution rotation curves of low surface brightness galaxies*, *Astron. Astrophys.* **385** (2002) 816, [astro-ph/0201276].
- [43] M. Spano, M. Marcelin, P. Amram, C. Carignan, B. Epinat et al., *GHASP: An H-alpha kinematic survey of spiral and irregular galaxies. 5. Dark matter distribution in 36 nearby spiral galaxies*, *Mon. Not. Roy. Astron. Soc.* **383** (2008) 297–316, [0710.1345].
- [44] S.-H. Oh et al., *High-resolution mass models of dwarf galaxies from LITTLE THINGS*, *Astron. J.* **149** (2015) 180, [1502.01281].
- [45] J. F. Navarro, V. R. Eke and C. S. Frenk, *The cores of dwarf galaxy halos*, *Mon. Not. Roy. Astron. Soc.* **283** (1996) L72–L78, [astro-ph/9610187].
- [46] O. Y. Gnedin and H. Zhao, *Maximum feedback and dark matter profiles of dwarf galaxies*, *Mon. Not. Roy. Astron. Soc.* **333** (2002) 299, [astro-ph/0108108].
- [47] J. I. Read and G. Gilmore, *Mass loss from dwarf spheroidal galaxies: The Origins of shallow dark matter cores and exponential surface brightness profiles*, *Mon. Not. Roy. Astron. Soc.* **356** (2005) 107–124, [astro-ph/0409565].
- [48] R. Kuzio de Naray and K. Spekkens, *Do Baryons Alter the Halos of Low Surface Brightness Galaxies?*, *Astrophys. J.* **741** (2011) L29, [1109.1288].
- [49] J. S. Bullock, *Notes on the Missing Satellites Problem*, 1009.4505.
- [50] B. Moore, S. Ghigna, F. Governato, G. Lake, T. R. Quinn et al., *Dark matter substructure within galactic halos*, *Astrophys. J.* **524** (1999) L19–L22, [astro-ph/9907411].
- [51] A. A. Klypin, A. V. Kravtsov, O. Valenzuela and F. Prada, *Where are the missing Galactic satellites?*, *Astrophys. J.* **522** (1999) 82–92, [astro-ph/9901240].
- [52] A. A. Thoul and D. H. Weinberg, *Hydrodynamic simulations of galaxy formation. 2. Photoionization and the formation of low mass galaxies*, *Astrophys. J.* **465** (1996) 608, [astro-ph/9510154].
- [53] J. S. Bullock, A. V. Kravtsov and D. H. Weinberg, *Reionization and the abundance of galactic satellites*, *Astrophys. J.* **539** (2000) 517, [astro-ph/0002214].
- [54] B. Willman, *Two new Milky Way companions*, *ASP Conf. Ser.* (2005) , [astro-ph/0506460].
- [55] SDSS COLLABORATION collaboration, V. Belokurov et al., *Cats and Dogs, Hair and A Hero: A Quintet of New Milky Way Companions*, *Astrophys. J.* **654** (2007) 897–906, [astro-ph/0608448].
- [56] V. Belokurov, M. Walker, N. Evans, D. Faria, G. Gilmore et al., *Leo V: A Companion of a Companion of the Milky Way Galaxy*, *Astrophys. J.* **686** (2008) L83–L86, [0807.2831].
- [57] E. J. Tollerud, J. S. Bullock, L. E. Strigari and B. Willman, *Hundreds of Milky Way Satellites? Luminosity Bias in the Satellite Luminosity Function*, *Astrophys. J.* **688** (2008) 277–289, [0806.4381].

- [58] DES collaboration, K. Bechtol et al., *Eight New Milky Way Companions Discovered in First-Year Dark Energy Survey Data*, *Astrophys. J.* **807** (2015) 50, [1503.02584].
- [59] DES collaboration, A. Drlica-Wagner et al., *Eight Ultra-faint Galaxy Candidates Discovered in Year Two of the Dark Energy Survey*, *Astrophys. J.* **813** (2015) 109, [1508.03622].
- [60] O. Newton, M. Cautun, A. Jenkins, C. S. Frenk and J. Helly, *The total satellite population of the Milky Way*, 1708.04247.
- [61] LSST collaboration, Z. Ivezić, J. A. Tyson, R. Allsman, J. Andrew and R. Angel, *LSST: from Science Drivers to Reference Design and Anticipated Data Products*, 0805.2366.
- [62] V. Springel, J. Wang, M. Vogelsberger, A. Ludlow, A. Jenkins et al., *The Aquarius Project: the subhalos of galactic halos*, *Mon. Not. Roy. Astron. Soc.* **391** (2008) 1685–1711, [0809.0898].
- [63] J. Wang, C. S. Frenk, J. F. Navarro and L. Gao, *The Missing Massive Satellites of the Milky Way*, *Mon. Not. Roy. Astron. Soc.* **424** (2012) 2715–2721, [1203.4097].
- [64] C. W. Purcell and A. R. Zentner, *Bailing Out the Milky Way: Variation in the Properties of Massive Dwarfs Among Galaxy-Sized Systems*, *JCAP* **1212** (2012) 007, [1208.4602].
- [65] E. J. Tollerud, M. Boylan-Kolchin and J. S. Bullock, *M31 Satellite Masses Compared to Λ CDM Subhaloes*, *Mon. Not. Roy. Astron. Soc.* **440** (2014) 3511–3519, [1403.6469].
- [66] S. Garrison-Kimmel, M. Boylan-Kolchin, J. S. Bullock and E. N. Kirby, *Too Big to Fail in the Local Group*, *Mon. Not. Roy. Astron. Soc.* **444** (2014) 222–236, [1404.5313].
- [67] S.-H. Oh, C. Brook, F. Governato, E. Brinks, L. Mayer, W. J. G. de Blok et al., *The central slope of dark matter cores in dwarf galaxies: Simulations vs. THINGS*, *Astron. J.* **142** (2011) 24, [1011.2777].
- [68] R. Teyssier, A. Pontzen, Y. Dubois and J. Read, *Cusp-core transformations in dwarf galaxies: observational predictions*, 1206.4895.
- [69] A. Zolotov, A. M. Brooks, B. Willman, F. Governato, A. Pontzen et al., *Baryons Matter: Why Luminous Satellite Galaxies Have Reduced Central Masses*, *Astrophys. J.* **761** (2012) 71, [1207.0007].
- [70] A. Di Cintio, C. B. Brook, A. V. Macciò, G. S. Stinson, A. Knebe, A. A. Dutton et al., *The dependence of dark matter profiles on the stellar-to-halo mass ratio: a prediction for cusps versus cores*, *Mon. Not. Roy. Astron. Soc.* **437** (2014) 415–423, [1306.0898].
- [71] A. Di Cintio, C. B. Brook, A. A. Dutton, A. V. Macciò, G. S. Stinson and A. Knebe, *A mass-dependent density profile for dark matter haloes including the influence of galaxy formation*, *Mon. Not. Roy. Astron. Soc.* **441** (2014) 2986–2995, [1404.5959].

- [72] R. Kannan, G. S. Stinson, A. V. Macciò, C. Brook, S. M. Weinmann, J. Wadsley et al., *The MaGICC volume: reproducing statistical properties of high redshift galaxies*, *Mon. Not. Roy. Astron. Soc.* **437** (2014) 3529–3539, [1302.2618].
- [73] T. K. Chan, D. Kereš, J. Oñorbe, P. F. Hopkins, A. L. Muratov, C. A. Faucher-Giguère et al., *The impact of baryonic physics on the structure of dark matter haloes: the view from the FIRE cosmological simulations*, *Mon. Not. Roy. Astron. Soc.* **454** (2015) 2981–3001, [1507.02282].
- [74] P. F. Hopkins, D. Keres, J. Onorbe, C.-A. Faucher-Giguere, E. Quataert, N. Murray et al., *Galaxies on FIRE (Feedback In Realistic Environments): Stellar Feedback Explains Cosmologically Inefficient Star Formation*, *Mon. Not. Roy. Astron. Soc.* **445** (2014) 581–603, [1311.2073].
- [75] S. Garrison-Kimmel, M. Rocha, M. Boylan-Kolchin, J. Bullock and J. Lally, *Can Feedback Solve the Too Big to Fail Problem?*, *Mon. Not. Roy. Astron. Soc.* **433** (2013) 3539, [1301.3137].
- [76] A. R. Wetzel, P. F. Hopkins, J.-h. Kim, C.-A. Faucher-Giguere, D. Keres and E. Quataert, *Reconciling dwarf galaxies with Λ CDM cosmology: Simulating a realistic population of satellites around a Milky Way-mass galaxy*, *Astrophys. J.* **827** (2016) L23, [1602.05957].
- [77] P. Colin, V. Avila-Reese and O. Valenzuela, *Substructure and halo density profiles in a warm dark matter cosmology*, *Astrophys. J.* **542** (2000) 622–630, [astro-ph/0004115].
- [78] A. Schneider, R. E. Smith, A. V. Maccio and B. Moore, *Nonlinear Evolution of Cosmological Structures in Warm Dark Matter Models*, 1112.0330.
- [79] M. Viel, G. D. Becker, J. S. Bolton and M. G. Haehnelt, *Warm dark matter as a solution to the small scale crisis: New constraints from high redshift Lyman-alpha forest data*, *Phys.Rev.* **D88** (2013) 043502, [1306.2314].
- [80] E. Polisensky and M. Ricotti, *Constraints on the Dark Matter Particle Mass from the Number of Milky Way Satellites*, *Phys.Rev.* **D83** (2011) 043506, [1004.1459].
- [81] A. Schneider, D. Anderhalden, A. Maccio and J. Diemand, *Warm dark matter does not do better than cold dark matter in solving small-scale inconsistencies*, 1309.5960.
- [82] V. Iršič et al., *New Constraints on the free-streaming of warm dark matter from intermediate and small scale Lyman- α forest data*, *Phys. Rev.* **D96** (2017) 023522, [1702.01764].
- [83] B. D. Wandelt, R. Dave, G. R. Farrar, P. C. McGuire, D. N. Spergel et al., *Selfinteracting dark matter*, astro-ph/0006344.
- [84] O. D. Elbert, J. S. Bullock, S. Garrison-Kimmel, M. Rocha, J. Oñorbe and A. H. G. Peter, *Core formation in dwarf haloes with self-interacting dark matter: no fine-tuning necessary*, *Mon. Not. Roy. Astron. Soc.* **453** (2015) 29–37, [1412.1477].

- [85] A. Gould, *Resonant Enhancements in WIMP Capture by the Earth*, *Astrophys.J.* **321** (1987) 571.
- [86] G. Jungman, M. Kamionkowski and K. Griest, *Supersymmetric dark matter*, *Phys.Rept.* **267** (1996) 195–373, [[hep-ph/9506380](#)].
- [87] M. Asplund, N. Grevesse, A. J. Sauval and P. Scott, *The chemical composition of the Sun*, *Ann.Rev.Astron.Astrophys.* **47** (2009) 481–522, [[0909.0948](#)].
- [88] P. Salucci, F. Nesti, G. Gentile and C. Martins, *The dark matter density at the Sun’s location*, *Astron.Astrophys.* **523** (2010) A83, [[1003.3101](#)].
- [89] R. Catena and P. Ullio, *A novel determination of the local dark matter density*, *JCAP* **1008** (2010) 004, [[0907.0018](#)].
- [90] A. Gould, *Weakly interacting massive particle distribution in and evaporation from the sun*, *Astrophys.J.* **321** (1987) 560–570.
- [91] K. Griest and D. Seckel, *Cosmic Asymmetry, Neutrinos and the Sun*, *Nucl.Phys.* **B283** (1987) 681.
- [92] Nasa, “Sun Fact Sheet, Nasa.”
<http://nssdc.gsfc.nasa.gov/planetary/factsheet/sunfact.html>, 2013.
- [93] S. Ritz and D. Seckel, *Detailed Neutrino Spectra From Cold Dark Matter Annihilations in the Sun*, *Nucl.Phys.* **B304** (1988) 877.
- [94] M. Srednicki, K. A. Olive and J. Silk, *High-Energy Neutrinos from the Sun and Cold Dark Matter*, *Nucl.Phys.* **B279** (1987) 804.
- [95] T. Gaisser, G. Steigman and S. Tilav, *Limits on Cold Dark Matter Candidates from Deep Underground Detectors*, *Phys.Rev.* **D34** (1986) 2206.
- [96] M. Blennow, J. Edsjo and T. Ohlsson, *Neutrinos from WIMP annihilations using a full three-flavor Monte Carlo*, *JCAP* **0801** (2008) 021, [[0709.3898](#)].
- [97] J. Edsjö, “WimpSim Neutrino Mont Carlo.”
<http://www.fysik.su.se/~edsjo/wimpsim/>, 2008.
- [98] T. Sjöstrand, S. Mrenna and P. Skands, *Pythia 6.4 physics and manual*, *Journal of High Energy Physics* **2006** (2006) 026.
- [99] J. Edsjö, *Aspects of Neutrino Detection of Neutralino Dark Matter*, 9704384.
- [100] J. Pumplin, D. Stump, J. Huston, H. Lai, P. M. Nadolsky et al., *New generation of parton distributions with uncertainties from global QCD analysis*, *JHEP* **0207** (2002) 012, [[hep-ph/0201195](#)].
- [101] P. M. Nadolsky, H.-L. Lai, Q.-H. Cao, J. Huston, J. Pumplin et al., *Implications of CTEQ global analysis for collider observables*, *Phys.Rev.* **D78** (2008) 013004, [[0802.0007](#)].
- [102] J. Edsjö, “Nusigma 1.17.” <http://copsosx03.physto.se/wimpsim/code.html>, 2013.

- [103] PARTICLE DATA GROUP collaboration, J. Beringer, J. F. Arguin, R. M. Barnett, K. Copic, O. Dahl et al., *Review of particle physics*, *Phys. Rev. D* **86** (Jul, 2012) 010001.
- [104] J. N. Bahcall, A. M. Serenelli and S. Basu, *New solar opacities, abundances, helioseismology, and neutrino fluxes*, *Astrophys.J.* **621** (2005) L85–L88, [[astro-ph/0412440](#)].
- [105] W. F. McDonough, *Compositional Model for the Earth’s Core*, vol. 2, ch. Matle and Core. Elsevier-Pergamon, Oxford, 2003.
- [106] M. Danniger, *Searches for Dark Matter with IceCube and DeepCore*, Ph.D. thesis, Department of Physics, Stockholm University, 2013.
- [107] ICECUBE collaboration, R. Abbasi et al., *The Design and Performance of IceCube DeepCore*, *Astropart. Phys.* **35** (2012) 615–624, [[1109.6096](#)].
- [108] LUX COLLABORATION collaboration, D. Akerib et al., *First results from the LUX dark matter experiment at the Sanford Underground Research Facility*, *Phys.Rev.Lett.* **112** (2014) 091303, [[1310.8214](#)].
- [109] L. G. van den Aarssen, T. Bringmann and C. Pfrommer, *Is dark matter with long-range interactions a solution to all small-scale problems of Lambda CDM cosmology?*, *Phys.Rev.Lett.* **109** (2012) 231301, [[1205.5809](#)].
- [110] S. Tulin, H.-B. Yu and K. M. Zurek, *Resonant Dark Forces and Small Scale Structure*, *Phys.Rev.Lett.* **110** (2013) 111301, [[1210.0900](#)].
- [111] A. Robertson, R. Massey and V. Eke, *What does the Bullet Cluster tell us about self-interacting dark matter?*, *Mon. Not. Roy. Astron. Soc.* **465** (2017) 569–587, [[1605.04307](#)].
- [112] D. Harvey, R. Massey, T. Kitching, A. Taylor and E. Tittley, *The non-gravitational interactions of dark matter in colliding galaxy clusters*, *Science* **347** (2015) 1462–1465, [[1503.07675](#)].
- [113] M. R. Buckley and P. J. Fox, *Dark Matter Self-Interactions and Light Force Carriers*, *Phys. Rev.* **D81** (2010) 083522, [[0911.3898](#)].
- [114] P. S. Krstić and D. R. Schultz, *Consistent definitions for, and relationships among, cross sections for elastic scattering of hydrogen ions, atoms, and molecules*, *Phys. Rev. A* **60** (Sep, 1999) 2118–2130.
- [115] M. Kaplinghat, S. Tulin and H.-B. Yu, *Self-interacting Dark Matter Benchmarks*, 1308.0618.
- [116] S. Galli, F. Iocco, G. Bertone and A. Melchiorri, *CMB constraints on Dark Matter models with large annihilation cross-section*, *Phys.Rev.* **D80** (2009) 023505, [[0905.0003](#)].
- [117] A. Sommerfeld, *Über die Beugung und Bremsung der Elektronen*, *Ann. der Physik* **403** (1931) 257.

- [118] J. Hisano, S. Matsumoto, M. M. Nojiri and O. Saito, *Non-perturbative effect on dark matter annihilation and gamma ray signature from galactic center*, *Phys. Rev. D* **71** (2005) 063528, [[hep-ph/0412403](#)].
- [119] S. Cassel, *Sommerfeld factor for arbitrary partial wave processes*, *J. Phys.* **G37** (2010) 105009, [[0903.5307](#)].
- [120] T. R. Slatyer, *The Sommerfeld enhancement for dark matter with an excited state*, *JCAP* **1002** (2010) 028, [[0910.5713](#)].
- [121] E. W. Kolb and M. S. Turner, *The Early Universe*, *Front. Phys.* **69** (1990) 1–547.
- [122] R. J. Scherrer and M. S. Turner, *On the Relic, Cosmic Abundance of Stable Weakly Interacting Massive Particles*, *Phys. Rev. D* **33** (1986) 1585.
- [123] B. Holdom, *Two $U(1)$'s and Epsilon Charge Shifts*, *Phys. Lett.* **166B** (1986) 196–198.
- [124] M. Pospelov and A. Ritz, *Astrophysical Signatures of Secluded Dark Matter*, *Phys. Lett.* **B671** (2009) 391–397, [[0810.1502](#)].
- [125] J. D. Bjorken, R. Essig, P. Schuster and N. Toro, *New Fixed-Target Experiments to Search for Dark Gauge Forces*, *Phys. Rev. D* **80** (2009) 075018, [[0906.0580](#)].
- [126] K. S. Babu, C. F. Kolda and J. March-Russell, *Implications of generalized $Z - Z'$ mixing*, *Phys. Rev. D* **57** (1998) 6788–6792, [[hep-ph/9710441](#)].
- [127] H. Davoudiasl, H.-S. Lee and W. J. Marciano, *'Dark' Z implications for Parity Violation, Rare Meson Decays, and Higgs Physics*, *Phys. Rev. D* **85** (2012) 115019, [[1203.2947](#)].
- [128] Y. Cui and F. D'Eramo, *On the Completeness of Vector Portal Theories: New Insights into the Dark Sector and its Interplay with Higgs Physics*, [1705.03897](#).
- [129] P. Langacker, *The Physics of Heavy Z' Gauge Bosons*, *Rev. Mod. Phys.* **81** (2009) 1199–1228, [[0801.1345](#)].
- [130] M. Cirelli, P. Panci, K. Petraki, F. Sala and M. Taoso, *Dark Matter's secret liaisons: phenomenology of a dark $U(1)$ sector with bound states*, *JCAP* **1705** (2017) 036, [[1612.07295](#)].
- [131] M. Kaplinghat, S. Tulin and H.-B. Yu, *Direct Detection Portals for Self-interacting Dark Matter*, *Phys. Rev. D* **89** (2014) 035009, [[1310.7945](#)].
- [132] E. Del Nobile, M. Kaplinghat and H.-B. Yu, *Direct Detection Signatures of Self-Interacting Dark Matter with a Light Mediator*, *JCAP* **1510** (2015) 055, [[1507.04007](#)].
- [133] N. Fornengo, P. Panci and M. Regis, *Long-Range Forces in Direct Dark Matter Searches*, *Phys. Rev. D* **84** (2011) 115002, [[1108.4661](#)].
- [134] T. Lin, H.-B. Yu and K. M. Zurek, *On Symmetric and Asymmetric Light Dark Matter*, *Phys. Rev. D* **85** (2012) 063503, [[1111.0293](#)].

- [135] J. B. Dent, F. Ferrer and L. M. Krauss, *Constraints on Light Hidden Sector Gauge Bosons from Supernova Cooling*, 1201.2683.
- [136] H. K. Dreiner, J.-F. Fortin, C. Hanhart and L. Ubaldi, *Supernova constraints on MeV dark sectors from e^+e^- annihilations*, *Phys. Rev.* **D89** (2014) 105015, [1310.3826].
- [137] D. Kazanas, R. N. Mohapatra, S. Nussinov, V. L. Teplitz and Y. Zhang, *Supernova Bounds on the Dark Photon Using its Electromagnetic Decay*, *Nucl. Phys.* **B890** (2014) 17–29, [1410.0221].
- [138] E. Rrapaj and S. Reddy, *Nucleon-nucleon bremsstrahlung of dark gauge bosons and revised supernova constraints*, *Phys. Rev.* **C94** (2016) 045805, [1511.09136].
- [139] E. Hardy and R. Lasenby, *Stellar cooling bounds on new light particles: plasma mixing effects*, *JHEP* **02** (2017) 033, [1611.05852].
- [140] J. H. Chang, R. Essig and S. D. McDermott, *Revisiting Supernova 1987A Constraints on Dark Photons*, *JHEP* **01** (2017) 107, [1611.03864].
- [141] J. D. Bjorken, S. Ecklund, W. R. Nelson, A. Abashian, C. Church, B. Lu et al., *Search for Neutral Metastable Penetrating Particles Produced in the SLAC Beam Dump*, *Phys. Rev.* **D38** (1988) 3375.
- [142] B. Batell, M. Pospelov and A. Ritz, *Exploring Portals to a Hidden Sector Through Fixed Targets*, *Phys. Rev.* **D80** (2009) 095024, [0906.5614].
- [143] R. Essig, R. Harnik, J. Kaplan and N. Toro, *Discovering New Light States at Neutrino Experiments*, *Phys. Rev.* **D82** (2010) 113008, [1008.0636].
- [144] CHARM collaboration, F. Bergsma et al., *A Search for Decays of Heavy Neutrinos in the Mass Range 0.5-GeV to 2.8-GeV*, *Phys. Lett.* **166B** (1986) 473–478.
- [145] S. N. Gninenko, *Constraints on sub-GeV hidden sector gauge bosons from a search for heavy neutrino decays*, *Phys. Lett.* **B713** (2012) 244–248, [1204.3583].
- [146] T. Bringmann, F. Kahlhoefer, K. Schmidt-Hoberg and P. Walia, *Strong constraints on self-interacting dark matter with light mediators*, *Phys. Rev. Lett.* **118** (2017) 141802, [1612.00845].
- [147] FERMI-LAT collaboration, M. Ackermann et al., *Searching for Dark Matter Annihilation from Milky Way Dwarf Spheroidal Galaxies with Six Years of Fermi Large Area Telescope Data*, *Phys. Rev. Lett.* **115** (2015) 231301, [1503.02641].
- [148] AMS collaboration, L. Accardo et al., *High Statistics Measurement of the Positron Fraction in Primary Cosmic Rays of 0.5–500 GeV with the Alpha Magnetic Spectrometer on the International Space Station*, *Phys. Rev. Lett.* **113** (2014) 121101.
- [149] AMS collaboration, M. Aguilar et al., *Electron and Positron Fluxes in Primary Cosmic Rays Measured with the Alpha Magnetic Spectrometer on the International Space Station*, *Phys. Rev. Lett.* **113** (2014) 121102.

- [150] AMS collaboration, M. Aguilar et al., *Antiproton Flux, Antiproton-to-Proton Flux Ratio, and Properties of Elementary Particle Fluxes in Primary Cosmic Rays Measured with the Alpha Magnetic Spectrometer on the International Space Station*, *Phys. Rev. Lett.* **117** (2016) 091103.
- [151] A. Gould, *WIMP Distribution in and Evaporation From the Sun*, *Astrophys.J.* **321** (1987) 560.
- [152] W. H. Press and D. N. Spergel, *Capture by the sun of a galactic population of weakly interacting massive particles*, *Astrophys. J.* **296** (1985) 679–684.
- [153] A. Gould, *Cosmological density of WIMPs from solar and terrestrial annihilations*, *Astrophys. J.* **388** (1992) 338–344.
- [154] ICECUBE PINGU collaboration, M. G. Aartsen et al., *Letter of Intent: The Precision IceCube Next Generation Upgrade (PINGU)*, 1401.2046.
- [155] V. Barger, W.-Y. Keung, G. Shaughnessy and A. Tregre, *High energy neutrinos from neutralino annihilations in the Sun*, *Phys. Rev.* **D76** (2007) 095008, [0708.1325].
- [156] M. Cirelli, N. Fornengo, T. Montaruli, I. A. Sokalski, A. Strumia et al., *Spectra of neutrinos from dark matter annihilations*, *Nucl.Phys.* **B727** (2005) 99–138, [hep-ph/0506298].
- [157] T. Ohlsson and H. Snellman, *Neutrino oscillations with three flavors in matter of varying density*, *Eur. Phys. J.* **C20** (2001) 507–515, [hep-ph/0103252].
- [158] ICECUBE collaboration, M. G. Aartsen et al., *Search for annihilating dark matter in the Sun with 3 years of IceCube data*, *Eur. Phys. J.* **C77** (2017) 146, [1612.05949].
- [159] ICECUBE-GEN2 collaboration, K. Clark, *Status of the PINGU detector*, *PoS ICRC2015* (2016) 1174.
- [160] M. Honda, M. Sajjad Athar, T. Kajita, K. Kasahara and S. Midorikawa, *Atmospheric neutrino flux calculation using the NRLMSISE-00 atmospheric model*, *Phys. Rev.* **D92** (2015) 023004, [1502.03916].
- [161] LUX collaboration, D. S. Akerib et al., *Results from a search for dark matter in the complete LUX exposure*, *Phys. Rev. Lett.* **118** (2017) 021303, [1608.07648].
- [162] J. L. Feng, J. Kumar, D. Marfatia and D. Sanford, *Isospin-Violating Dark Matter*, *Phys. Lett.* **B703** (2011) 124–127, [1102.4331].